Construction et utilisation de modèles anatomiques

par

Alexandre GUIMOND

Thèse de doctorat effectuée en cotutelle

Département d'informatique et de recherche opérationnelle

Faculté des arts et des sciences

Université de Montréal

et

École doctorale des sciences pour l'ingénieur

Université de Nice - Sophia Antipolis

Thèse présentée à

la Faculté des études supérieures de l'Université de Montréal

en vue de l'obtention du grade de Philosophiæ doctor (Ph.D.) en informatique

et à

l'École doctorale des sciences pour l'ingénieur de l'Université de Nice - Sophia Antipolis

en vue de l'obtention du grade de Docteur en sciences pour l'ingénieur.

22 décembre 1999

Page d'identification du jury

Université de Montréal
Faculté des études supérieures

et

Université de Nice - Sophia Antipolis
École doctorale des sciences pour l'ingénieur

Cette thèse intitulée

Construction et utilisation de modèles anatomiques

présenté et soutenue à l'Université de Montréal par:

Alexandre GUIMOND

a été évaluée par un jury composé des personnes suivantes:

Président	Pierre POULIN, Université de Montréal
Directeur de recherche	Jean MEUNIER, Université de Montréal
Directeur de recherche	Jean-Philippe THIRION, INRIA Sophia Antipolis
Membre du jury	Olivier FAUGERAS, INRIA Sophia Antipolis
Examinateur externe et rapporteur	Louis COLLINS, Université McGill
Rapporteur	Laurent YOUNES, École Normale Supérieure de Cachan
Représentant du doyen de la FES	A.-Robert LEBLANC, Université de Montréal

Résumé

Dans cette thèse, nous présentons différents problèmes reliés à la construction et l'utilisation de modèles anatomiques conçus à partir d'images volumétriques tridimensionnelles, ainsi que les solutions que nous proposons.

Notre apport se reflète sur trois domaines du traitement d'images médicales : le recalage d'images, la recherche de régions anatomiques correspondantes dans une base de données d'images et la construction de modèles moyens.

Au niveau du recalage, nous présentons une méthode de correction d'intensité s'intégrant au sein d'une méthode d'évaluation de différences de forme. La technique présentée permet d'évaluer les différences d'intensités dues à des paramètres d'acquisition différents ainsi qu'à des modalités d'acquisition différentes.

Ensuite, une méthode est présentée permettant de parcourir rapidement un ensemble d'images non recalées et provenant de sujets différents afin d'y extraire la même région anatomique. Cette méthode, locale et rapide, permet l'analyse de la même structure cérébrale d'un ensemble de sujets dans des délais applicables en milieu clinique.

Finalement, nous présentons une méthode complètement automatique de construction de modèle moyen anatomique « stable » du cerveau humain à partir d'un ensemble d'images de résonance magnétique. Les modèles calculés présentent deux caractéristiques importantes : une intensité moyenne ainsi qu'une forme moyenne, les deux dans une même image. Des statistiques sur la variabilité de la forme et de l'intensité des structures du cerveau peuvent aussi être calculées.

Abstract

In this thesis, we present various problems connected to the construction and the use of anatomical models built using three-dimensional volumetric images, as well as the solutions we propose.

Our contribution is reflected on three fields of medical image processing: image registration, the search for corresponding anatomical regions in an image database and the construction of average models.

Regarding registration, we present a method of intensity correction integrated within a method evaluating shape differences. The technique presented makes it possible to evaluate the differences in intensities due to different acquisition parameters as well as different acquisition methods.

Then, a method is presented making it possible to quickly traverse a set of non-registered images coming from different subjects in order to extract the same anatomical region. This method, local and fast, allows the analysis of the same cerebral structure of a set of subjects in a clinical context.

Finally, we present a completely automatic method for the construction of "stable" average anatomical models of the human brain from a set of magnetic resonance (MR) images. The calculated models show two significant characteristics: an average intensity as well as an average shape, both in the same image. Statistics regarding shape and intensity variability of brain structures may also be computed.

Remerciements

À toutes les personnes que j'ai côtoyées au cours des cinq dernières années des deux côtés de l'Atlantique, je voudrais exprimer toute ma reconnaissance. Cette thèse n'aurait pu plus être réalisée sans leur soutien moral.

Je tiens à remercier mes directeurs de thèse Jean Meunier et Jean-Philippe Thirion pour leurs précieux conseils, leur support et leur encouragements qui m'ont permis de réaliser cette thèse.

Je veux aussi remercier mes confrères des laboratoires de Vision et de Modélisation Géométrique et d'Informatique Graphique de l'Université de Montréal ainsi que du projet Epidaure de l'INRIA Sophia Antipolis qui forment des environnements de recherche des plus stimulants et au sein desquelles les idées présentées dans cette thèse ont émergées.

Enfin, je souhaite exprimer ma plus profonde gratitude à ma famille qui a toujours su m'encourager et me soutenir dans mes démarches.

Cette thèse a été réalisée en partie grâce au soutien financier du Conseil de Recherches en Sciences Naturelles et en Génie du Canada et du Fonds pour la Formation de Chercheurs et l'Aide à la Recherche.

Table des matières

Table des figures

Liste des tableaux

Chapitre 1

Introduction

Sommaire

1.1 Problématique

Les troubles neurologiques telles la schizophrénie ou la maladie d'ALZHEIMER sont depuis longtemps le sujet d'études sérieuses. Ces recherches ont permis de remarquer que leur présence s'accompagne parfois d'une déformation de certaines structures cérébrales. Cependant, l'étude quantitative de ces déformations reste à faire ; c'est-à-dire qu'aujourd'hui, nous entendons beaucoup plus parler de « gros » putamen ou de « gros » ventricules que d'une différence de volume quantifiée par rapport à une normale.

L'idée de caractériser les différentes structures cérébrales ne date pas d'hier. Le grand nombre d'atlas anatomiques du cerveau [67, 75, 88] le prouvent bien. Par contre, comme le

présentent MAZZIOTTA *et al.* [68] ainsi que SUBSOL [83], ces atlas sur papier ne répondent plus aux besoins actuels et ceci pour plusieurs raisons. Premièrement, le support papier, quoique encore très utilisé cliniquement par les médecins, s'avère insuffisant pour emmagasiner les quantités appréciables d'informations contenues dans ces atlas. On a alors recours à des atlas surchargés de caractéristiques ou peu synthétiques. Deuxièmement, ils sont généralement basés sur l'étude d'un seul, ou au mieux, de quelques individus plutôt que sur des mesures obtenues d'une population. La variabilité anatomique interindividuelle est si grande que l'application directe de ces observations est généralement impossible ou hasardeuse. Finalement, ces atlas sont publiés et non maintenus ; c'est-à-dire qu'ils ont une forme statique et l'information qu'ils contiennent ne peut-être mise à jour facilement. Il devient donc nécessaire de transférer l'information de ces atlas vers des médias plus appropriés à leur utilisation et leur maintien. Il existe d'ailleurs présentement quelques atlas numériques commercialisés sur le marché [50, 1], mais ce sont des adaptations informatiques d'atlas papier. Ils offrent donc l'avantage de synthétiser plus d'informations sur une même page et peuvent la disposer plus adéquatement, mais ces atlas comportent encore l'inconvénient d'être statiques et basés sur des mesures tirées d'un minimum de sujets.

Au cours des dernières années, l'utilisation de l'imagerie par résonance magnétique (IRM) a engendré de vastes bases de données (BD) d'images médicales. L'étude de cette information pourrait fournir les éléments nécessaires à la construction d'atlas numériques comprenant des données quantitatives à propos des caractéristiques des différentes structures cérébrales.

1.2 Le recalage

1.2.1 Les correspondances

Toute méthode de comparaison quantitative d'images médicales nécessite une manière de trouver une correspondance point à point entre deux images. Le recalage est une méthode tentant de solutionner ce problème en calculant la transformation nécessaire à appliquer à une image afin de la rendre le plus similaire possible à une autre. Plus formellement, recaler une image source S sur une image cible (*target*) T, en se contraignant à une classe

de transformations H et à une mesure de similitude C dépendante des deux images et de la transformation, correspond à trouver la fonction $h \in H$ qui optimise $C(T,S,h)$.

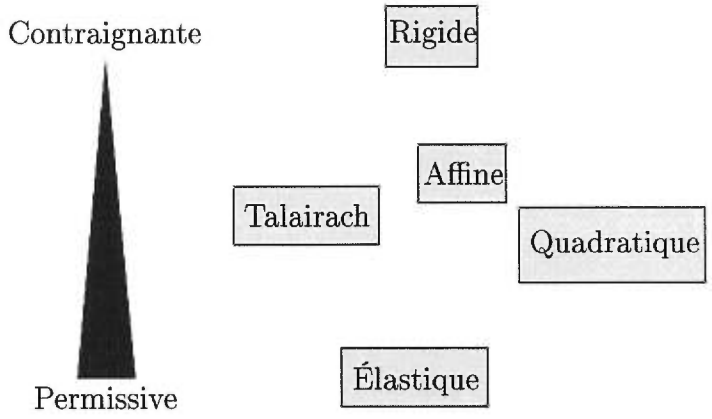

FIG. 1.1 – *Classification de différentes classes de transformations.*

La classe de transformations H permises suscite toujours de grands débats. Plusieurs approches existent. Pour en nommer quelques-unes, des méthodes de recalage ont été développées permettant des transformations linéaires [21, 2, 66], linéaires par morceaux [61], quadratiques [39], splines [6] et élastiques ou fluides [89, 18, 22, 3] (Voir la figure 1.1 pour une classification approximative.).

Le choix de l'une ou l'autre de ces classes de transformations dépendra du type de recalage souhaité, qui fera généralement partie d'un des quatre cas de figure suivants :

Recalage monomodal intrapatient Mettre en correspondance des images d'un même sujet acquises selon la même modalité mais à des instants différents. Par exemple, pour voir l'évolution d'une maladie. On utilisera ici soit un recalage rigide pour ensuite étudier l'image de soustraction, soit un recalage non rigide pour étudier le champ de déplacements résultant.

Recalage multimodal intrapatient Mettre en correspondance des images d'un même sujet acquises selon différentes modalités (IRM-TEP[1], CT[2]-TEP, etc.). Cela nécessite habituellement l'estimation d'une transformation rigide et est généralement utilisé afin de regrouper des informations complémentaires provenant d'acquisitions de modalités

1. Tomographie par Émission de Positon
2. *Computed Tomography*

différentes d'un même patient.

Recalage monomodal interpatient Mettre en correspondance des images de patients différents acquises selon la même modalité. On utilisera dans ce cas des classes de transformations plutôt permissives. Ce type de recalage sert entre autre à quantifier les différences de forme de structures anatomiques provenant de sujets différents.

Recalage multimodal interpatient Mettre en correspondance des images de patients différents acquises selon différentes modalités, par exemple pour recaler une image CT avec une image de résonance magnétique (RM). Peu de travaux ont été réalisés dans ce domaine, mais au cours des dernières années, certains groupes s'y sont attaqués.

Pour chacune de ces catégories, différentes méthodes de recalage ont été proposées (Voir TOGA [98] pour une description détaillée des méthodes les plus populaires et MAINTZ & VIERGEVER [65] pour une classification exhaustive.). Elles peuvent être divisées en deux grandes catégories :

1. Les méthodes basées sur les repères, et
2. les méthodes basées sur les intensités.

Dans cette thèse, nous nous intéressons à la quantification automatique de variations de forme des structures cérébrales. Ainsi, les méthodes manuelles ou semi-automatiques ne seront pas abordées car elles requièrent l'intervention d'un usager expérimenté pour de longues périodes de temps et ne sont pas adaptées à un usage clinique quotidien. De plus, les différences dues à des transformations linéaires (translation, rotation, facteur d'échelle et cisaillement) ne sont pas étudiées car elles sont considérées comme des variations normales. Ceci s'explique par exemple par le fait que tous les cerveaux n'ont pas la même taille. Cependant, ce n'est pas le reflet d'une pathologie, mais seulement de variations normales.

Le lecteur intéressé par les méthodes de recalage linéaire dans un cadre monomodal est invité à consulter les travaux de COLLINS *et al.* [21], ANDREASEN *et al.* [2] et MARTIN *et al.* [66]. Pour le recalage rigide multimodal, les travaux de WEST *et al.* [104] présentent une étude comparative de différentes méthodes de recalage rigide développées jusqu'en 1996. Cependant, les techniques les plus populaires aujourd'hui ont été développées au cours des dernières années et sont celles de VIOLA & WELLS [102], MAES *et al.* [62] et ROCHE *et al.* [78].

Les méthodes abordées ci-après sont des techniques de recalage non rigide, également appelées techniques de *warping*.

1.2.2 Les méthodes basées sur les repères

Ces méthodes sont basées sur des repères anatomiques extraits soit manuellement, soit automatiquement, de chaque image, et la correspondance entre points contraint la transformation (Voir la figure 1.2.). Ces repères peuvent être divisés en quatre catégories :

1. Les repères anatomiques tels l'interface entre structures,
2. les repères géométriques tels les courbures maximales,
3. les repères extrinsèques tels les marqueurs externes ajustés sur un crâne, et
4. les motifs d'intensités tels les points de fort gradient.

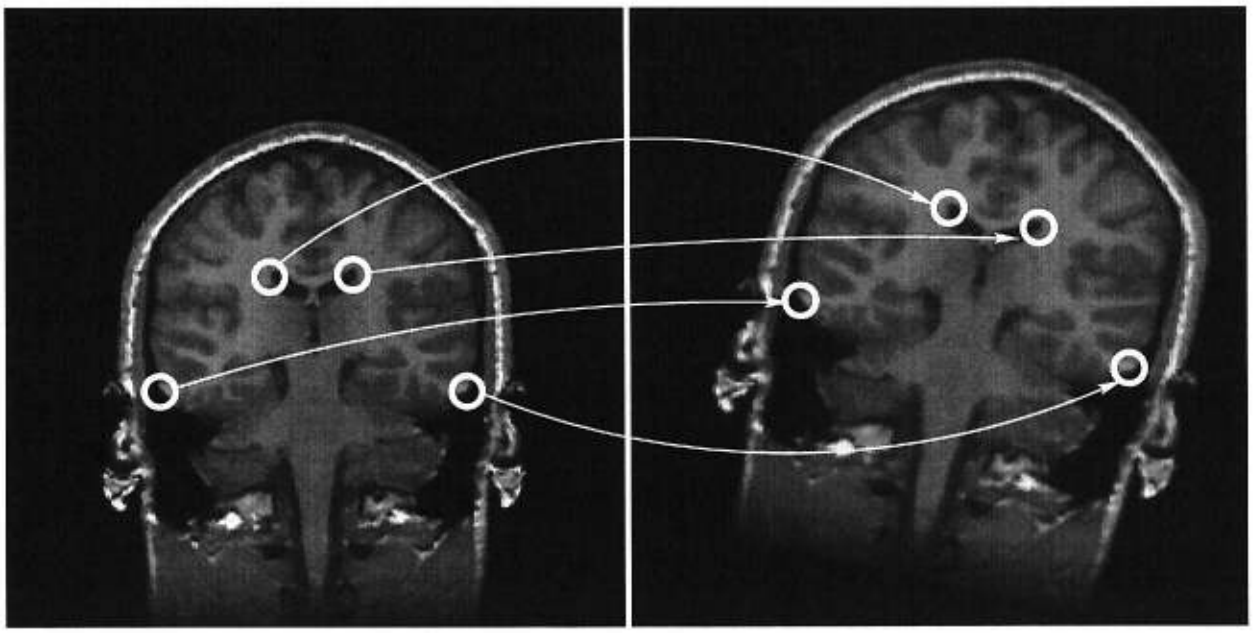

FIG. 1.2 – *La correspondance entre points de repères anatomiques définit la transformation.*

Le système de coordonnées de TALAIRACH & TOURNOUX [88] (Voir les figures 1.3 et 1.4.), aussi connu sous le nom du système de grille proportionnelle tridimensionnelle, est fréquemment utilisé en milieu clinique. Ce système est défini par la ligne bicommissurale[3], le point

3. Cette ligne est définie à partir de deux points de repère anatomiques : les commissures antérieure (CA) et postérieure (CP). C'est pourquoi on la nomme communément la ligne CA-CP, ou AC-PC en anglais.

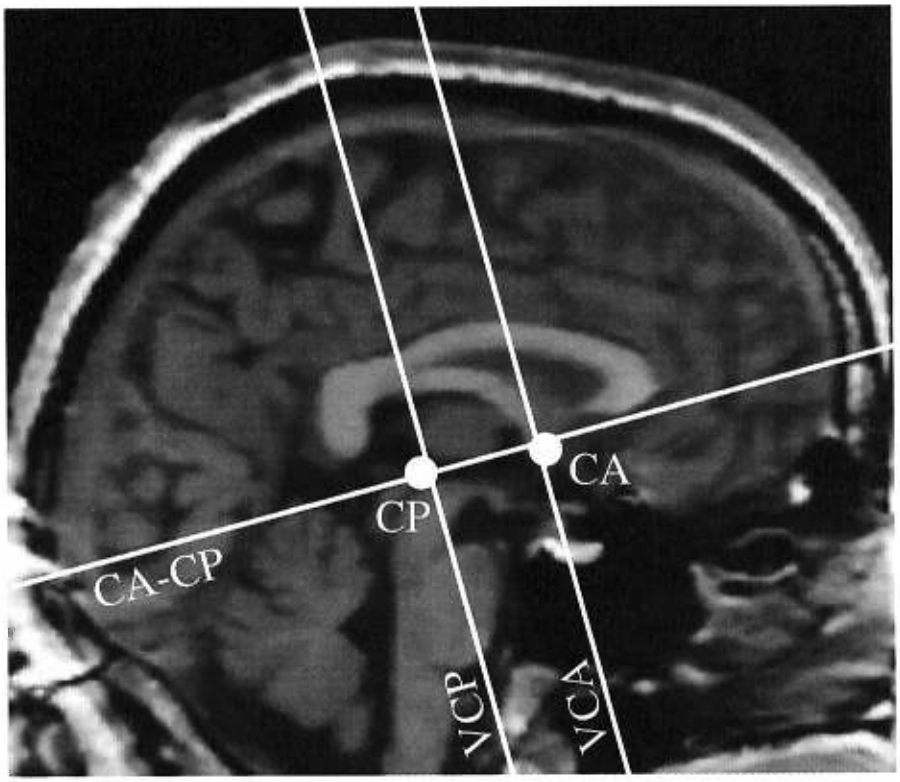

FIG. 1.3 – *Système de référence de base de* TALAIRACH. *Le cerveau est divisé en 12 régions définies par 1) le plan inter-hémisphérique (c'est le plan de coupe pour cette figure), 2) un plan perpendiculaire au plan inter-hémisphérique et contenant la ligne* CA-CP, *3) un plan perpendiculaire aux deux premiers et touchant la partie postérieure du point* CA *(VCA), et 4) un plan perpendiculaire aux deux premiers et contenant le point* CP *(VCP). La ligne CA-CP repose sur la face supérieure du point CA et la face inférieure du point CP.*

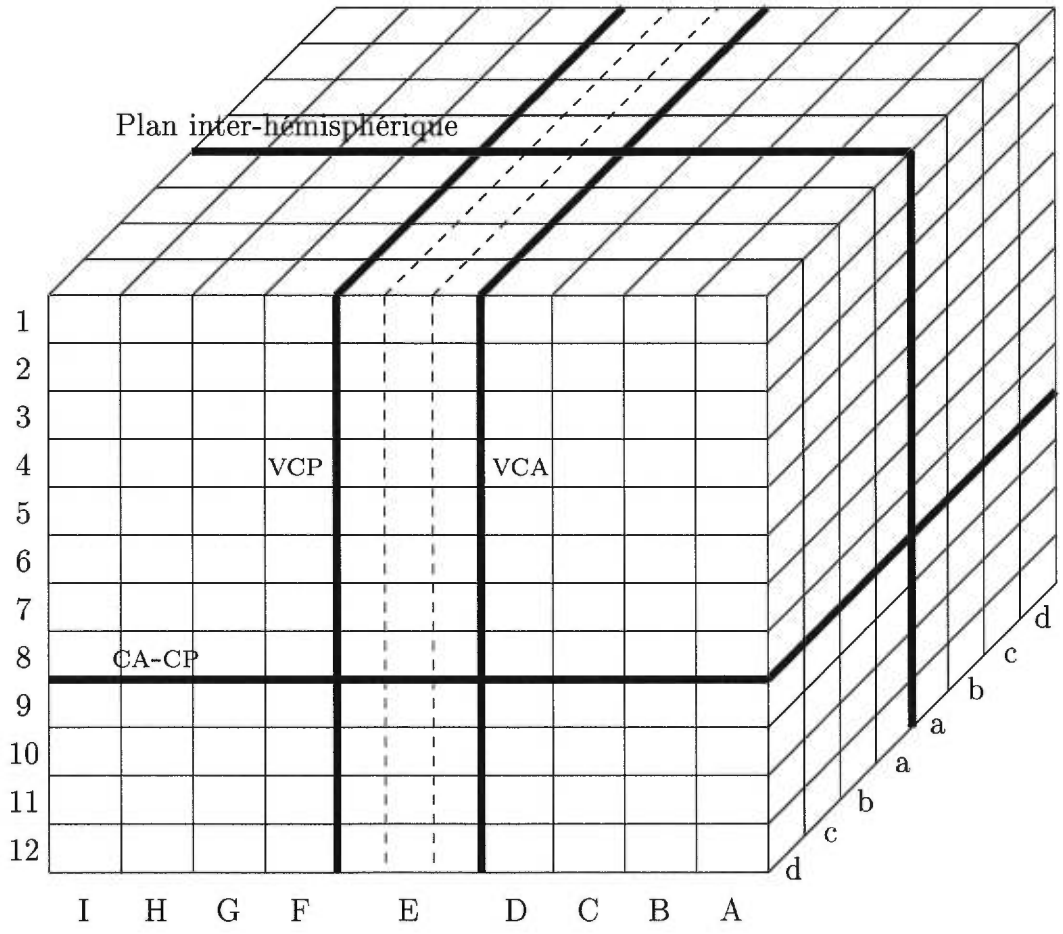

FIG. 1.4 – *Le système de grille proportionnelle tridimensionnelle de* TALAIRACH. *Chaque structure cérébrale a des coordonnées dans l'espace (par exemple* $(a,D,9)$ *ou* $(c,G,6)$*) ce qui permet de la comparer directement aux structures correspondantes identifiées à la même position chez d'autres sujets.*

supérieur du cortex pariétal et le point inférieur du cortex temporal comme frontières supérieure et inférieure, le point le plus postérieur du cortex occipital et le point le plus antérieur du cortex frontal comme frontières postérieure et antérieure ainsi que le point le plus latéral du cortex pariétotemporal comme frontière latérale, afin de diviser le cerveau en douze sous-espaces. Ce système est une tentative de modélisation des différences non-linéaires entre jeux de données.

Malgré sa popularité, le système de TALAIRACH est vivement critiqué car il entraîne une grande variabilité sur la position de structures éloignées des repères anatomiques. Ainsi, des approches prometteuses ont dernièrement été proposées permettant une localisation de structures anatomiques plus abondantes tout en réduisant substantiellement les erreurs de position [98].

Malgré les résultats intéressants fournis par ce type de méthode de recalage, il serait difficile de les adapter à nos besoins. En effet, ces méthodes ont été conçues afin de mettre en correspondance des volumes complets alors que nous comptons concentrer nos travaux sur des sous-régions des images initiales. Les repères obtenus à l'aide de ces techniques seraient alors trop instables et en trop petit nombre pour espérer un recalage adéquat. De plus, même si la correspondance entre les repères peut être très précise, nous croyons que les méthodes basées sur les intensités fournissent des résultats globalement plus précis dû au fait que chaque voxel des images peut-être considéré comme un point de repère. Nous nous attarderons donc aux méthodes de recalage basées sur les intensités et référons le lecteur aux documents cités ainsi qu'à TOGA [98] pour plus d'informations sur les techniques basées sur les repères.

1.2.3 Les méthodes basées sur les intensités

Il existe plusieurs méthode de recalage non rigide basés sur les intensités. Nous n'en mentionnons ici que quelques-unes qui nous paraissent fondamentales et référons le lecteur à TOGA [98] ou encore MAINTZ *et al.* [64] pour une analyse plus complète.

De manière générale, ces algorithmes retournent un champ de déplacements v permettant de déformer une image source S en une image cible T. Nos images ayant trois dimensions,

les vecteurs de v sont tridimensionnels. Le déplacement à un point $x = (x_1,x_2,x_3)$ est alors dénoté par $v(x) = [v_1(x),v_2(x),v_3(x)]$ et la transformation h est définie par $h(x) = v(x) + x$. Ainsi, l'application de h sur S transforme cette image de sorte qu'elle présente la même forme que T.

Lors de la mise en œuvre de ces méthodes, deux éléments essentiels sont mis de l'avant. Premièrement, un critère de similarité doit être proposé. Il permettra de trouver des correspondances point à point entre les images à recaler. Deuxièmement, on tentera généralement d'imposer certaines contraintes sur l'aspect de la déformation afin de modéliser une transformation plausible. Ceci se reflétera par une forme de régularisation du champ de déplacements v.

Nous allons premièrement présenter certains critères de similarité couramment utilisés puis nous aborderons les méthodes de régularisation les plus populaires.

Les critères de similarité

La somme du carré des différences Le critère de similarité sans doute le plus intuitif est la minimisation de la somme du carré des différences entre T et S,

$$C(T,S,h) = \sum_x ||T(x) - S \circ h(x)||^2, \tag{1.1}$$

où $\circ$ dénote la composition. Ce critère est utilisé entre autres par CHRISTENSEN [18], MILLER [70] et JOSHI [54]. Cependant, cette formulation impose que les intensités des structures correspondantes de T et S soient les mêmes. Ceci constitue une contrainte importante et difficilement réalisable lorsque l'on se place dans un contexte où l'on veut recaler plusieurs images entre elles comme c'est le cas dans cette thèse. En pratique, ceci nous contraint à utiliser des images obtenues sur le même scanner avec les mêmes paramètres d'acquisition. De plus, cette méthode ne permet pas de recaler des images de patients dont les anomalies entraînent des variations influant sur la réponse des différents tissus lors de l'acquisition.

Le flux optique Un autre critère ayant la même contrainte est le flux optique. Il est basée sur l'idée qu'il existe une relation entre la variation temporelle de l'image en un point et le mouvement du capteur, des objets et de leurs déformations. On a donc ici affaire plutôt

à une modélisation du problème qu'à un critère de similarité. Cependant, c'est de cette modélisation que découlent les appariements entre points et nous l'introduisons donc ici.

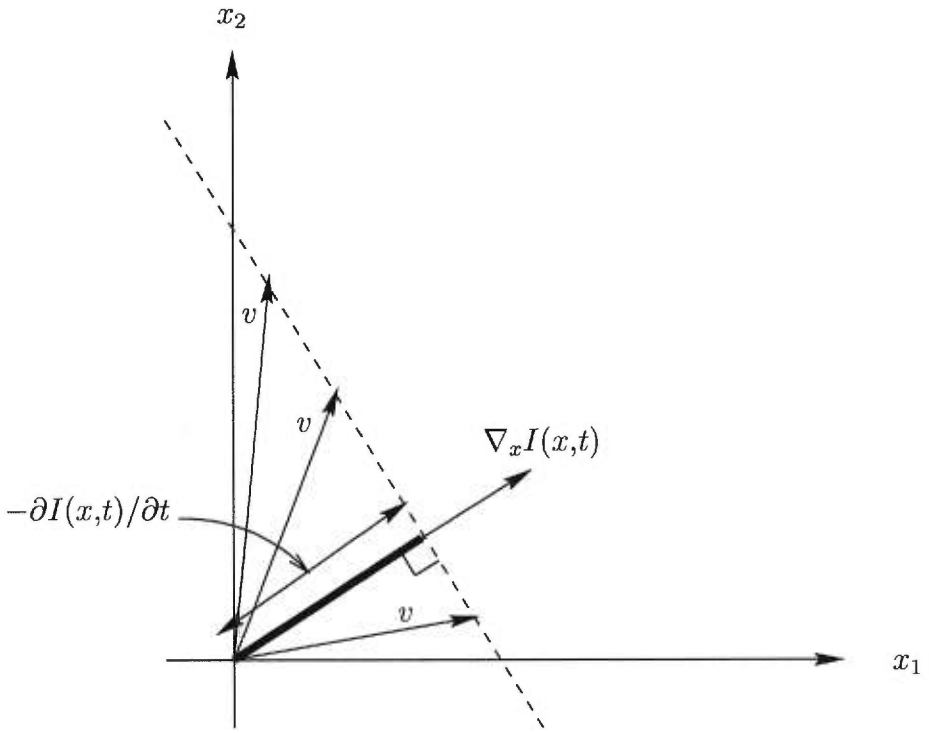

FIG. 1.5 – *Contrainte de gradient pour le flux optique en deux dimensions. Tout v solution de l'équation 1.3 doit avoir son extrémité reposant sur le pointillé.*

Différents modèles de flux optique existent [5], mais nous ne nous attarderons qu'à la forme la plus populaire : les techniques différentielles [52]. Dans ce contexte, les images T et S sont considérées comme des échantillons d'une séquence d'images $I(x,t)$ où t représente le moment d'acquisition. Supposons maintenant que

$$I(x,t) = I(x + v(x)\delta t, t + \delta t). \tag{1.2}$$

L'équation 1.2 nous dit que l'intensité des objets est conservée et donc que $\partial I(x,t)/\partial t = 0$. Concrètement, ceci signifie que l'intensité des structures cérébrales correspondantes dans T et S est la même. Nous pouvons réécrire cette dernière égalité de la manière suivante,

$$\nabla_x I(x,t) \cdot v(x) + \partial I(x,t)/\partial t = 0 \tag{1.3}$$

où $\nabla_x I(x,t) = \left(\frac{\partial I(x,t)}{\partial x_1}, \frac{\partial I(x,t)}{\partial x_2}, \frac{\partial I(x,t)}{\partial x_3}\right)$ est le gradient spatial de $I(x,t)$ par rapport à la position x. L'équation 1.3 est une équation avec un nombre d'inconnues égal à la dimension des images. En fait, elle ne donne que la composante des déplacements dans la direction du gradient (Voir la figure 1.5 pour une interprétation géométrique en deux dimensions.). Comme nous le verrons plus tard, des méthodes de régularisations peuvent être jumelées à cette approche afin d'obtenir la composante des déplacements dans les autres directions.

Une autre approche pour obtenir les appariements est de choisir une direction privilégiée. C'est ce qui est proposé par THIRION [89, 93, 92] qui choisit la direction du gradient $\nabla_x I(x,t)$. Les déplacements correspondent alors à

$$v(x) = -\frac{\partial I(x,t)/\partial t}{||\nabla_x I(x,t)||^2} \nabla_x I(x,t). \tag{1.4}$$

Pour des raison de stabilité algorithmique lorsque le gradient est de faible norme, le terme $(\partial I(x,t)/\partial t)^2$ est ajouté au dénominateur de l'équation 1.4. De plus, en assumant que les déplacements entre T et S sont petits, on peut estimer $\partial I(x,t)/\partial t$ par $S(x)-T(x)$ et $\nabla_x I(x,t)$ par $\nabla T(x)$. L'équation 1.4 devient alors

$$v(x) = -\frac{S(x) - T(x)}{||\nabla T(x)||^2 + [S(x) - T(x)]^2} \nabla T(x). \tag{1.5}$$

La corrélation normalisée Pour se défaire de cette contrainte d'intensité, BAJCSY & KOVAČIČ [3] ainsi que GEE *et al.* [35] ont proposé d'utiliser le maximum de corrélation normalisée comme mesure de similitude. La corrélation normalisée entre T et S est définie comme suit,

$$\frac{\sum_x [T(x) \times S \circ h(x)]}{\sqrt{\sum_x T(x)^2} \times \sqrt{\sum_x [S \circ h(x)]^2}}, \tag{1.6}$$

et sa valeur se situe dans l'intervalle [0,1] puisque les valeurs de T et S sont toutes positives. Cette valeur mesure le degré de dépendance linéaire entre les intensités des deux images, 1 correspondant à une parfaite dépendance linéaire et une valeur de 0 correspondant à aucune dépendance linéaire. Cette méthode cherche donc à maximiser la corrélation normalisée.

Ce critère a l'avantage d'être invariant par rapport aux différences linéaires d'intensités entre T et S. C'est-à-dire qu'il produit le même résultat si les valeurs de S sont multipliées

par une valeur et/ou si on leur additionne une valeur. Il est ainsi plus robuste à bon nombre de transformations d'intensité que l'on retrouve couramment dans les images intramodales à recaler. Cependant, ces différences d'intensité doivent être linéaires et uniformes sur l'ensemble de l'image.

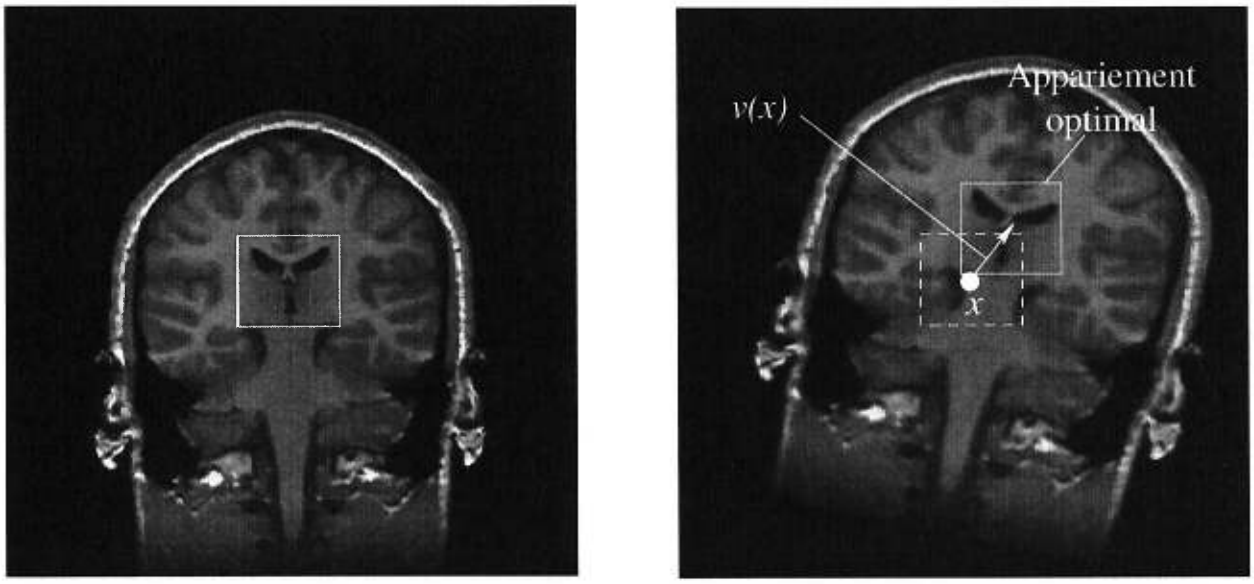

FIG. 1.6 – *Représentation de la technique de* block matching. *Un bloc défini dans l'image de gauche est déplacé dans un certain voisinage de celle de droite. La région de la deuxième image qui fournit le meilleur appariement avec la première région, selon un critère donné tel que la corrélation normalisée, permet de définir le vecteur de déplacement pour ce bloc. Ce procédé est répété pour l'ensemble des blocs définis dans l'image de gauche et pour plusieurs tailles de blocs différentes.*

Pour s'affranchir de cette dernière contrainte, COLLINS *et al.* [22] proposent d'utiliser la corrélation normalisée au sein d'une technique de *block matching* (Voir la figure 1.6.) pour obtenir les correspondances. Cette technique consiste à diviser une image en un groupe de blocs, chacun étant déplacé localement dans l'autre image afin d'obtenir un appariement optimal au sens de la corrélation normalisée. Ceci permet d'obtenir des transformations d'intensité linéaires différentes pour différentes régions de l'image. Notons que pour cette méthode, la mesure de similitude est une pondération de la corrélation normalisée entre les intensités des images ainsi que de la corrélation normalisée entre la norme du gradient des

images.

Autres critères de similarité En plus des méthodes précédentes, il existe une grande variété de critères de similarité utilisés pour fin de recalage [64, 63]. Nous en présentons ici quelques unes que nous trouvons intéressantes mais qui ne se sont pas encore démarquées dans le domaine du recalage non rigide.

Le rapport de corrélation Le rapport de corrélation [78] est un critère de similarité développé dans un but de recalage rigide multimodal. Il assume, qu'une fois T et S recalées, il existe une dépendance fonctionnelle entre les intensité de T par rapport à celles de S, $T = f(S)$. Il est défini comme :

$$\eta^2(T|S) = 1 - \frac{\text{var}(T - \hat{f}(S))}{\text{var}(T)}, \tag{1.7}$$

où $\hat{f}(S)$ est une approximation au moindre carrés de T en fonction de S. Il est montré par Roche *et al.* [77] que sous l'hypothèse d'un bruit Gaussien sur T, le rapport de corrélation est une mesure de similarité optimale dans le cadre d'estimation par maximum de vraisemblance.

Quoique développé pour le recalage multimodal rigide, le rapport de corrélation fut récemment utilisé dans un contexte de recalage multimodal non rigide [59].

L'information mutuelle L'information mutuelle [72, 34] est une mesure de similarité bien connue. Elle est définie comme :

$$\text{I}(T,S) = \text{H}(T) + \text{H}(S) - \text{H}(T,S) \tag{1.8}$$

où $\text{H}(\cdot)$ est l'entropie d'une variable aléatoire[4].

L'entropie est une mesure de désordre ou encore d'information, c'est-à-dire la partie non prévisible d'une observation. La quantité d'informations apportée par un symbole de probabilité p_k est représentée par $-\log p_k$, parce que si le symbole est rare, il porte une grande information alors que s'il est fréquent, cette information est faible. De plus, si deux

4. Les images S et T sont considérées comme des densités de probabilités décrivant chacune une variable aléatoire.

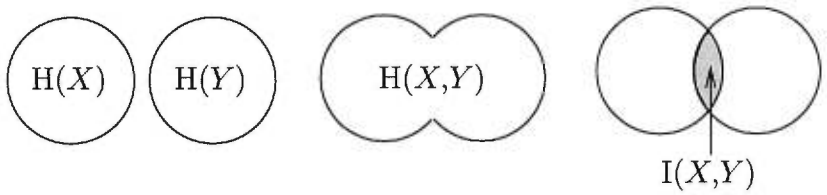

FIG. 1.7 – *Relation entre l'entropie de deux variables aléatoires et l'information mutuelle.*

événements indépendants sont de probabilités p_1 et p_2, l'information totale de probabilité $p_1 \times p_2$ est la somme des informations partielles. L'entropie elle est alors définie comme l'espérance mathématique de l'information que peut contenir une variable aléatoire

$$\begin{aligned} H(T) &= \mathrm{E}\{-\log p(T)\} = -\int p(t)\log p(t)dt \\ H(S) &= \mathrm{E}\{-\log p(S)\} = -\int p(s)\log p(s)ds \\ H(T,S) &= \mathrm{E}\{-\log p(T,S)\} = -\int p(t,s)\log p(t,s)ds\,dt. \end{aligned} \tag{1.9}$$

En examinant la figure 1.7, nous comprenons que plus l'information mutuelle entre deux images est grande, plus ces images sont similaires. Ce type de similarité a principalement été utilisé dans un contexte de recalage rigide d'images provenant de modalités différentes [102, 62] mais également pour le recalage rigide intramodalité [69] ainsi que tout dernièrement dans un contexte de recalage multimodal non rigide [64, 33].

SSC et DSC Venot *et al.* [100, 101] introduisent deux critères de similarité pour fins de recalage : les changements de signe stochastique (« stochastic sign change » ou SSC) et déterministe (« deterministic sign change » ou DSC). Considérons deux images, $I_1(x)$ et $I_2(x)$ différentes seulement à cause d'un bruit additif de moyenne zéro et ayant une fonction de densité symétrique. Soit $D(x) = I_1(x) - I_2(x)$ l'image de soustraction. Si le bruit est nul, les valeurs de $D(x)$ sont nulles également. En présence de bruit, ces valeurs oscillent autour de zéro. Supposons maintenant que les deux images diffèrent pour une région donnée. Dans cette zone, les valeurs de $D(x)$ sont toutes négatives ou positives. Elle ne contient pas de changement de signe. Donc, dans le cas d'images bruitées, plus les images sont similaires, plus le nombre de changements de signe est grand. Le critère SSC est donc défini comme le nombre de changements de signe des pixels de $D(x)$ parcourue dans chaque dimension. Quand les

images ne sont pas bruitées, on peut bruiter artificiellement l'image de soustraction de la manière suivante

$$D'(x) = \begin{cases} I_1(x) - I_2(x) - q & \text{si } \sum_{x \in x} x \text{ est paire,} \\ I_1(x) - I_2(x) + q & \text{sinon,} \end{cases} \tag{1.10}$$

où q est un réel de petite valeur.

Le DSC et le SSC ont surtout été utilisés pour la comparaison d'images synthigraphiques ou angiographiques quoique leur utilisation ait également connu un certain succès avec d'autres types d'images [41, 71].

Les méthodes de régularisation

La contrainte explicite Cette méthode consiste à introduire lors de la minimisation du critère C une contrainte sur le champ de déplacements. Par exemple, HORN & SCHUNK [52] proposent de combiner la contrainte de gradient de l'équation 1.3 avec une contrainte de lissage global sur v. Cette contrainte a pour but de modéliser la notion intuitive que la transformation ne doit pas séparer ou briser les objets présents dans les images. Concrètement, une structure anatomique ne devrait pas se scinder en deux. Ils minimisent ainsi

$$\int \left(\nabla_x I(x,t) \cdot v(x) + \frac{\partial I(x,t)}{\partial t} \right)^2 + \alpha^2 \left(||\nabla v_1(x)||^2 + ||\nabla v_2(x)||^2 + ||\nabla v_3(x)||^2 \right) dx \tag{1.11}$$

où α^2 est un multiplicateur de LAGRANGE et l'intégrale est évaluée sur l'ensemble du domaine de x. Une solution itérative est alors utilisée pour obtenir v,

$$v_{n+1}(x) = \overline{v}_n(x) - \frac{\nabla_x I(x,t) \cdot \overline{v}_n(x) + \partial I(x,t)/\partial t}{||\nabla_x I(x,t)||^2 + \alpha^2} \nabla_x I(x,t) \tag{1.12}$$

où $\overline{v}_n$ dénote des moyennes dans le voisinage de v à la n^{e} itération et le champ initial v_0 est nul.

Similairement, BAJCSY & KOVAČIČ [3], GEE *et al.* [35], CHRISTENSEN *et al.* [18], MILLER *et al.* [70] ainsi que JOSHI [54] ajoutent des contraintes permettant de générer des transformations respectant certains modèles physiques (élasticité, fluidité, etc.). Ces contraintes sont issues soit de la mécanique des fluides, soit de la mécanique des milieux continus et ont l'avantage de produire des transformations correspondant à des phénomènes bien connus.

Cependant, ces méthodes de régularisation requièrent beaucoup de temps de calcul (jusqu'à plusieurs jours pour le modèle fluide) ce qui les rend peu attrayantes par approche à la prochaine méthode.

Le lissage Une autre approche de régularisation est d'obtenir les appariements sans contrainte puis d'en calculer des moyennes locales à l'aide d'un filtrage Gaussien afin d'obtenir une transformation lisse. Le principal avantage de cette méthode est son faible temps de calcul.

THIRION [89, 93, 92] utilise ce type de régularisation en la jumelant à l'équation 1.5 au sein d'une méthode itérative. Les déplacements à l'itération $n+1$ sont obtenus à l'aide de la formule

$$v_{n+1}(x) = G_\sigma \otimes \left(v_n(x) - \frac{S \circ h_n(x) - T(x)}{||\nabla T(x)||^2 + [S \circ h_n(x) - T(x)]^2} \nabla T(x) \right), \qquad (1.13)$$

où G_σ représente un filtre Gaussien et $\otimes$ la convolution.

COLLINS *et al.* [22] fait également usage de cette méthode afin de régulariser les appariements obtenus par *block matching*.

Résumé

Voici donc en résumé ce que proposent les méthodes de recalage monomodal non rigide les plus connues.

HORN & SCHUNK [52] utilisent la contrainte de conservation d'intensité (Équation 1.3) du flux optique ainsi qu'une contrainte de régularisation imposant un champ de déplacements lisse.

THIRION [89, 93, 92] utilise également la contrainte d'intensité du flux optique pour obtenir les déplacements dans la direction du gradient, mais régularise le champ de déplacements à l'aide d'un lissage Gaussien.

COLLINS *et al.* [22] utilisent également un filtrage Gaussien mais minimisent le critère de corrélation normalisée dans un cadre de *block matching*.

BAJCSY & KOVAČIČ [3] ainsi que GEE *et al.* [35], contrairement à l'approche précédente, minimisent la corrélation normalisée sur l'*ensemble* des images T et S. La régularisation

est explicitée au sein de la minimisation pour modéliser un matériaux élastique.

CHRISTENSEN *et al.* [18], MILLER *et al.* [70] et JOSHI [54] utilisent également un modèle de régularisation physique, mais le critère à minimiser est la somme du carré des différences entre T et S.

De plus, pour toutes ces approches, il est important que les images à recaler ne soient pas trop différentes l'une de l'autre. Dans le cadre des approches minimisant un critère de similarité, ceci s'explique par la forme fortement non quadratique du critère. Il est alors important de commencer la minimisation proche de la solution optimale afin de ne pas tomber dans un minimum local. Dans le cadre des approches à base de flux optique, l'estimation de la dérivée temporelle $\partial I(x,t)/\partial t$ par $S - T$ n'est justifiable que si les déplacements entre ces deux images sont petits.

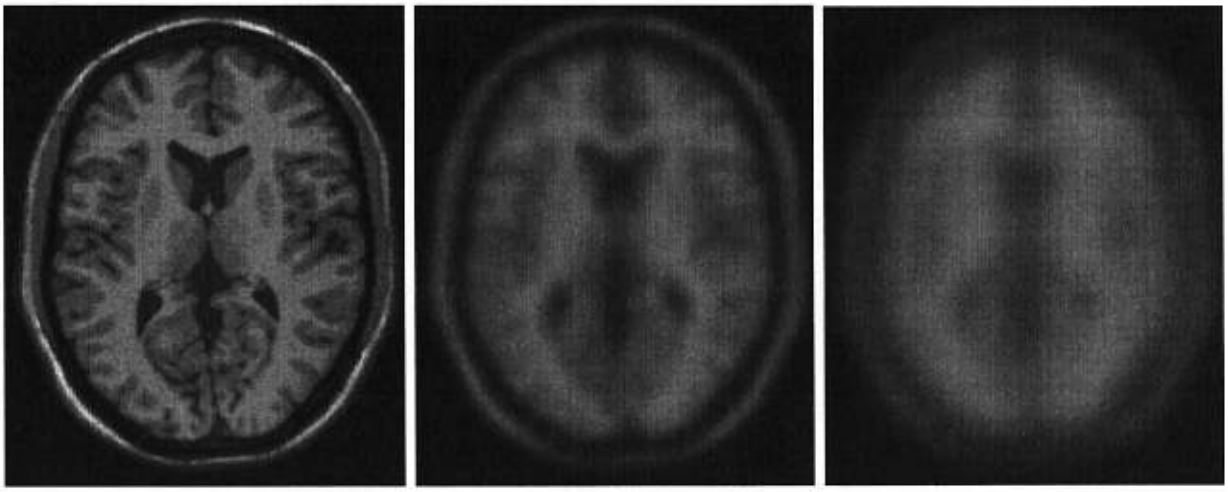

(a) Petite échelle (image originale).

(b) Moyenne échelle ($\sigma = 3$).

(c) Grande échelle ($\sigma = 6$).

FIG. 1.8 – *Trois images d'une représentation multiéchelle construite à l'aide d'un filtre Gaussien.*

Ainsi, toutes approches mentionnées plus haut utilisent différentes combinaisons des techniques suivantes :

- Les images à recaler sont préalablement recalées à l'aide de méthodes rigides ou affines.
- Une approche multiéchelle est employée (Voir la figure 1.8.). Cette technique consiste à représenter une image à partir d'une famille d'images. Chaque image est générée de

façon à ce que les détails des petites échelles soient graduellement enlevés, souvent à l'aide de filtres Gaussiens. Les premières itérations de l'algorithme de recalage sont effectuées avec les images à grande échelles où seulement les structures principales sont recalées, et le facteur d'échelle est graduellement réduit au cours des itérations.

- Une approche multirésolution est employée (Voir la figure 1.9.). Les images sont ici représentées à l'aide d'une structure pyramidale. L'image originale, au bas de la pyramide, est filtrée à l'aide d'un filtre moyen puis sous-échantillonnée afin de créer une image de moindre résolution. Ce processus est répété afin de créer plusieurs images représentant les différents niveaux de la pyramide. Les premières itérations de l'algorithme de recalage sont effectuées avec les images du haut, puis l'algorithme évoluera graduellement vers le bas.

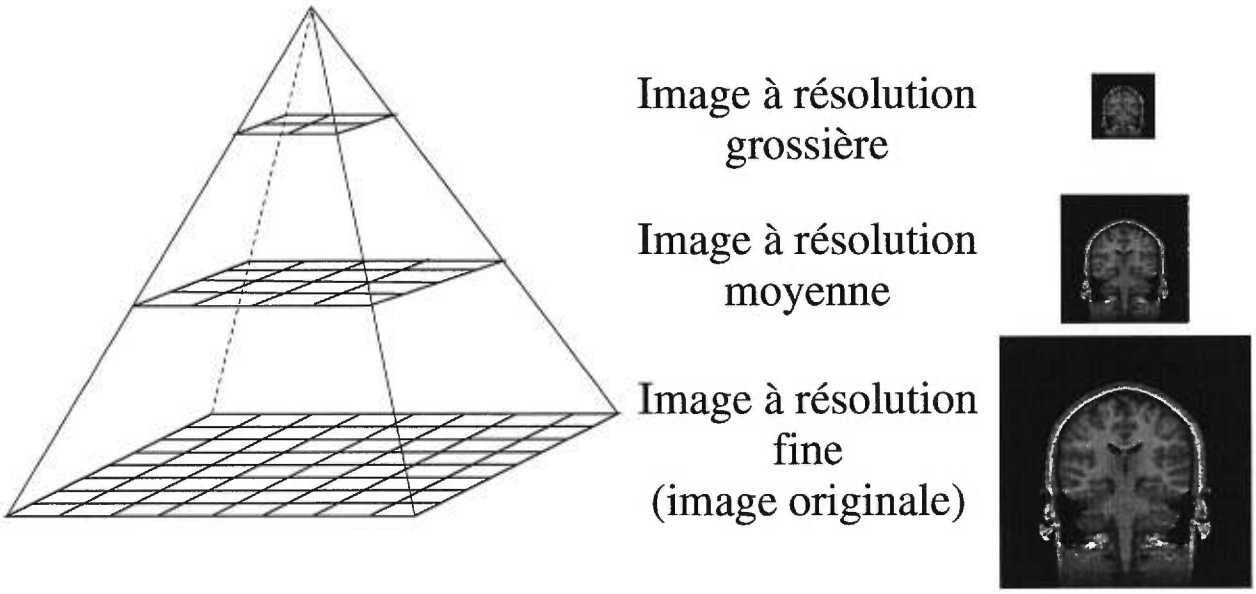

FIG. 1.9 – *Une représentation multirésolution à trois niveaux.*

Le lecteur intéressé par les techniques multiéchelles et multirésolutions pourra consulter BAJCSY & KOVAČIČ [57] pour introduction détaillée à ces domaines et MAINTZ *et al.* [64] pour une classification des différents algorithmes de recalages qui en font usage.

1.3 Organisation du manuscrit

Nous proposons ici une méthode permettant l'étude quantitative des variations de forme et d'intensité de structures cérébrales au sein d'une population. Ces travaux ont été réalisés dans un cadre pratique visant des applications cliniques. Ainsi, nous avons développé des outils interactifs permettant à un clinicien d'identifier rapidement les régions normales et anormales d'une structure d'intérêt et d'obtenir des informations quantitatives sur l'amplitude des anomalies présentes.

Nous détaillons dans le chapitre 2 la méthode de recalage utilisée pour cette thèse. Elle permet un recalage précis et est très peu sensible aux différences de distribution d'intensité entre les images.

Nous présentons ensuite dans le chapitre 3 une technique automatique et rapide permettant, à l'aide de notre technique de recalage, d'extraire de chaque image d'une BD d'images médicales tridimensionnelle une même région arbitrairement définie tout en évitant les techniques usuelles de segmentation automatique et les problèmes qui s'y rattachent. Cette technique permet à un médecin d'obtenir des informations quantitatives sur les différences de forme et d'intensité locale d'une image par rapport à une autre.

Finalement, utilisant notre technique de recalage, nous avons développé dans le chapitre 4 une méthode de construction de modèles anatomiques moyens du cerveau à partir d'une BD d'images médicales et étudié sa convergence vers le centroïde de la distribution de cet ensemble d'images. Nous montrons également comment obtenir des informations quantitatives sur la variabilité des différentes structures du cerveau. Jumelé aux travaux précédents portant sur l'étude d'une structure particulière, il devient ainsi possible d'évaluer rapidement ses variations normales et anormales et d'en mesurer l'importance.

1.4 Notation

La rédaction des articles composant cette thèse s'étale sur quatre ans. Durant cette période, la notation utilisée a quelque peu évolué. Ainsi, nous tenons à avertir le lecteur de quelques variations et abus de langage employés dans les chapitres 3 et 4 qui sont les moins

récents. En particulier, le terme *reference* est employé pour désigner la cible et le terme *model* pour désigner la source. Ceci correspond à la terminologie employée par Thirion dans la description de sa technique de recalage [89]. On notera également dans ces chapitres que nous employons par abus de langage les termes *deformations* et *deformation field* pour désigner *displacement field.*

Chapitre 2

Mise en correspondance

Sommaire

Avant-propos

Dans les prochains chapitres, la méthode de recalage utilisée est celle présentée dans l'article qui suit [44]. À la section 2.2.1, nous nous plaçons dans un contexte où les structures anatomiques correspondantes ont la même intensité dans toutes les images. Sous cette

contrainte, nous décrivons la manière utilisée afin d'évaluer les différences de forme entre cerveaux et relions notre méthode à différents concepts populaires en recalage non-linéaire monomodal. Cette partie de notre méthode est une petite variation de la méthode des démons présentée aux sections 1.2.3 et 2.2.1.

Cependant, un des problèmes important rencontré en recalage monomodal est la différence d'intensité entre structures correspondantes dans différentes images. Dans des conditions idéales (sujets sains, même scanner, même heure d'acquisition, etc.) cette différence est pratiquement nulle, mais il est fréquent d'obtenir des images de scanners différents et/ou dont les valeurs d'intensité ont subit différents traitements. Il devient alors important de faire une correction d'intensité puisque notre méthode est basée sur la contrainte de même intensité pour les structures correspondantes des images à l'étude.

Ainsi, nous présentons à la section 2.2.2 une méthode de correction d'intensité s'intégrant au sein de la méthode d'évaluation de différences de forme. La technique présentée permet d'évaluer les différences d'intensité dues à des paramètres d'acquisition différents ainsi qu'à des modalités d'acquisition différentes.

La méthode de recalage utilisée dans les chapitres suivants est celle des démons [89, 93, 92] qui assume une dépendance linéaire entre les intensités des images à recaler et est équivalente à celle proposé ici sous cette contrainte. Le lecteur pourrait se demander s'il ne serait pas plus judicieux d'utiliser notre méthode avec un polynôme de degré plus élevé, mais comme présenté dans l'article, augmenter le degré du polynôme a comme effet de permettre des transformations d'intensité qui ne sont pas justifiées pour le recalage d'images de sujets normaux. Pour le recalage de sujets anormaux, notre approche est cependant recommandée.

L'article qui suit est une version modifiée d'un article soumis à la revue *IEEE Transaction on Medical Imaging* dont la référence bibliographique est la suivante :

> A. GUIMOND, A. ROCHE, N. AYACHE, et J. MEUNIER. « Three-Dimensional Multimodal Brain Warping Using the Demons Algorithm and Adaptive Intensity Corrections ». *IEEE Transactions in Medical Imaging*, 1999. Soumis.

Three-Dimensional Multimodal Brain Warping Using the Demons Algorithm and Adaptative Intensity Corrections

Abstract

This paper presents an original method for three-dimensional elastic registration of multimodal images. We propose to make use of a scheme that iterates between correcting for intensity differences between images and performing standard monomodal registration. The core of our contribution resides in providing a method that finds the transformation that maps the intensities of one image to those of another. It makes the assumption that there are at most two functional dependences between the intensities of structures present in the images to register, and relies on robust estimation techniques to evaluate these functions. We provide results showing successful registration between several imaging modalities involving segmentations, T1 magnetic resonance (MR), T2 MR, proton density (PD) MR and computed tomography (CT). We also argue that our intensity modeling may be more appropriate than mutual information (MI) in the context of evaluating high-dimensional deformations, as it puts more constraints on the parameters to be estimated and thus permits a better search of the parameter space.

keywords: Multimodality, Elastic registration, Intensity correction, Robust estimation, Medical imaging.

2.1 Introduction

Over the last decade, automatic registration techniques of medical images of the head have been developed following two main trends: 1) registration of multimodal images using low degree transformations (rigid or affine), and 2) registration of monomodal images using high-dimensional volumetric maps (elastic or fluid deformations). The first category mainly addresses the fusion of complementary information obtained from different imaging modalities. The second category's predominant purpose is the evaluation of either the anatomical evolution process present in a particular subject or of anatomical variations between different subjects.

These two trends have evolved separately mainly because the combined problem of identifying complex intensity correspondences along with a high-dimensional geometrical transformation defines a search space arduous to traverse. Recently, three groups have imposed different constraints on the search space, enabling them to develop automatic multimodal non-affine registration techniques. All three methods make use of block matching techniques to evaluate local translations. Two of them use mutual information (MI) [102, 62] as a similarity measure and the other employs the correlation ratio [78].

The major difficulty in using MI as a similarity measure for registration is to compute the conditional probabilities of one image's intensities with respect to those of the other. To do so, Maintz *et al.* [64] proposed to use conditional probabilities after rigid matching of the images as an estimate of the real conditional probabilities after local transformations. Hence, the probabilities are evaluated only once before fluid registration. However, Gaens *et al.* [33] argued that the assumption that probabilities computed after affine registration are good approximations of the same probabilities after fluid matching is unsuitable. They also proposed a method in which local displacements are found so that the global MI increases at each iteration, permitting incremental changes of the probabilities during registration. Their method necessitates the computation of conditional probabilities over the whole image for every voxel displacement. To alleviate themselves from such computations owing to the fact that MI requires many samples to estimate probabilities, Lau *et al.* [59] have chosen a different similarity measure. Due to the robustness of the correlation ratio with regards to sparse data [78], they employed it to assess the similarity of neighboring blocks. Hence no global computation is required when moving subregions of the image.

Our method distinguishes itself by looking at the problem from a different angle. In the last years, our group has had some success with monomodal image registration using the demons method [90, 93], an optical flow variant when dealing with monomodal volumetric images. If we were able to model the imaging processes that created the images to register, and assuming these processes are invertible, one could transform one of the images so that they are both represented in the same modality. Then, we could use our monomodal registration algorithm to register them. We have thus developed a completely automatic method to transform the different structures intensities in one image so that they match the

intensities of the corresponding structures in another image, and this without resorting to any segmentation method.

The rational behind our formulation is that there is a functional relationship between the intensity of a majority of structures when imaged with different modalities. This assumption is partly justified by the fact that the Woods criterion [106] as well as the correlation ratio [78], which evaluate a functional dependence between the images to match, have been used with success in the past, and sometimes lead to better results than MI [77, 76], which assumes a more general constraint.

The idea of estimating an intensity transformation during registration is not new in itself. For example, Feldmar *et al.* [29] as well as Barber [4] have both published methods in which intensity corrections are proposed. These methods restrict themselves to estimating linear intensity transformations in a monomodal registration context. Friston *et al.* [30] also proposed a method to estimate spatial and intensity functions to put PET and MR images into register using a standard least squares solution. Their modeling of the problem is similar to ours but their solution requires segmentation of the images and is not robust to outliers. We propose here a registration model based on one or two high degree polynomials found using a robust regression technique to enable the registration of raw images from different modalities.

The remaining sections of this paper are organized in the following manner. First, we detail our multimodal elastic registration method. We then describe what kind of images were used to test our method and how they were acquired. Next, results obtained by registering different images obtained from several modalities are presented and discussed. We conclude this paper with a brief discussion on future research tracks.

2.2 Method

Our registration algorithm is iterative and each iteration consists of two parts. The first one transforms the intensities of anatomical structures of a source image S so that they match the intensities of the corresponding structures of a target image T. The second part regards the registration of S (after intensity transformation) with T using our elastic registration

algorithm.

In the following, we first describe the three-dimensional geometrical transformation model and then the intensity transformation model. We believe this ordering is more convenient since it is easier to see what result must provide the intensity transformation once the geometrical transformation procedure is clarified. However, we wish to make clear to the reader that *each iteration* of our registration method proceeds first by estimating the intensity transformation and then the geometrical transformation.

2.2.1 Modeling the Geometrical Transformation

Many algorithms have been developed that deform one brain so its shape matches that of another [98]. The procedure used in the following work was influenced by a variety of methods, primarily the demons algorithm [90, 93]. It finds the displacement $v(x)$ for each voxel x of T so it matches the corresponding anatomical location in S. The solution is found using the following iterative scheme,

$$v_{n+1}(x) = G_\sigma \otimes \left(v_n + \frac{S \circ h_n(x) - T(x)}{||\nabla(S \circ h_n)(x)||^2 + [S \circ h_n(x) - T(x)]^2} \nabla(S \circ h_n)(x) \right), \qquad (2.1)$$

where G_σ is a Gaussian filter with a variance of σ^2, $\otimes$ denotes the convolution, $\circ$ denotes the composition and the transformation $h(x)$ is related to the displacement by $h(x) = x + v(x)$. As is common with registration methods, we also make use of multilevel techniques to accelerate convergence. Details about the number of levels and iterations as well as filter implementation issues are addressed in Section 2.4. We here show how our method can be related to other registration methods, notably the minimization of the sum of squared difference (SSD) criterion, optical flow and the demons algorithm.

Relation with SSD Minimization

In this framework, we find the transformation h that minimizes the sum of squared differences between the transformed source image and the target image. The SSD between the two images for a given transformation h applied to the source is defined as

$$SSD(h) = \frac{1}{2} \sum_{x=1}^{N} [S \circ h(x) - T(x)]^2. \qquad (2.2)$$

Minimization of Equation (2.2) is performed using a gradient descent algorithm. Thus, differentiating the above equation we get

$$\nabla SSD(h) = -[S \circ h(x) - T(x)]\nabla(S \circ h)(x). \tag{2.3}$$

The iterative scheme is then of the form

$$h_{n+1} = h_n + \alpha[S \circ h_n(x) - T(x)]\nabla(S \circ h_n)(x), \tag{2.4}$$

where α is the step length. This last equation implies

$$v_{n+1} = v_n + \alpha[S \circ h_n(x) - T(x)]\nabla(S \circ h_n)(x). \tag{2.5}$$

If we set α to a constant value, this method corresponds to a first order gradient descent algorithm. By comparing Equation (2.5) to Equation (2.1), one sees that our method sets

$$\alpha = \frac{1}{||\nabla(S \circ h_n)(x)||^2 + [T(x) - S \circ h_n(x)]^2} \tag{2.6}$$

and applies a Gaussian filter to provide a smooth displacement field. Cachier *et al.* [15, 74] have shown that using Equation (2.6) closely relates Equation (2.1) with a second order gradient descent of the SSD criterion, in which each iteration n sets h_{n+1} to the minimum of the SSD quadratic approximation at h_n. We refer the reader to these articles for a more technical discussion on this subject as well as for the formula that corresponds to a true second order gradient descent.

Relation with Optical Flow

T and S are considered as successive time samples of an image sequence represented by $I(x,t)$, where $x = (x_1, x_2, x_3)$ is a voxel position in the image and t is time. The displacements are computed by constraining the brightness of brain structures to be constant in time so that

$$\frac{dI(x,t)}{dt} = 0. \tag{2.7}$$

It is well known that Equation (2.7) is not sufficient to provide a unique displacement for each voxel. In fact, this constraint leads to

$$f(x) = -\frac{\partial I(x,t)/\partial t}{||\nabla_x I(x,t)||^2}\nabla_x I(x,t), \tag{2.8}$$

which is the component of the displacement in the direction of the brightness gradient $\nabla_x I(x,t) = \left(\frac{\partial I(x,t)}{\partial x_1}, \frac{\partial I(x,t)}{\partial x_2}, \frac{\partial I(x,t)}{\partial x_3}\right)^T$ [52]. Other constraints need to be added to Equation (2.7) to obtain the displacement components in other directions. Many methods have been proposed to fill this purpose and thus regularize the resulting vector field [5]. One that can be computed very efficiently was proposed by Thirion [93] in his description of the demons registration method using a complete grid of demons. It consists of smoothing each dimension of the vector field with a Gaussian filter G_σ. He also proposed to add $[\partial I(x,t)/\partial t]^2$ to the denominator of Equation (2.8) for numerical stability when $\nabla_x I(x,t)$ is close to zero, a term which serves the same purpose as α^2 in the original optical flow formulation of Horn and Schunck [52]. As is presented by Bro-Nielsen and Gramkow [13], this kind of regularization approximates a linear elasticity transformation model.

With this in mind, the displacement that maps a voxel position in T to its position in S is found using an iterative method,

$$v_{n+1}(x) = G_\sigma \otimes \left(v_n - \frac{\partial I(x,t)/\partial t}{||\nabla_x I(x,t)||^2 + [\partial I(x,t)/\partial t]^2} \nabla_x I(x,t) \right). \tag{2.9}$$

Spatial derivatives may be computed in several ways [52, 12, 82]. We have observed from practical experience that our method performs best when they are computed from the resampled source image of the current iteration. As shown in Section 2.2.1, this is in agreement with the SSD minimization. Temporal derivatives are obtained by subtracting the target images from the resampled source image of the current iteration. These considerations relate Equation (2.9) to Equation (2.1). The reader should note that the major difference between this method and other optical flow strategies based on differential techniques is that regularization is performed *after* the calculation of the displacements in the gradient direction instead of using an explicit regularization term in a minimization framework.

Relation with the Demons Algorithm

Our algorithm actually is a small variation of the demons method [90, 93] using a complete grid of demons, itself closely related to optical flow as described in the previous section. The

demons algorithm finds the displacements using the following formula,

$$v_{n+1}(x) = G_\sigma \otimes \left(v_n - \frac{T(x) - S \circ h_n(x)}{||\nabla T(x)||^2 + [T(x) - S \circ h_n(x)]^2} \nabla T(x) \right). \tag{2.10}$$

As can be seen from the last equation, the only difference from our formulation (Equation (2.1)) and the demons method is that derivatives are computed on the resampled source image of the current iteration. This modification was performed following the observations on the minimization of the SSD criterion.

Relevance of the Resulting Transformation

In the case of inter-subject non-affine registration, quantifying the accuracy of a method is difficult. One could deform an image I into I' using a known displacement field v, register I with I' and compare the result of the registration with v, but this comparison is biased by the way v is generated. For example, since our algorithm produces a smooth displacement field, if the vectors of v were to be generated randomly, the method is expected to perform poorly. Another method is to place landmarks in the images to register and evaluate differences between landmarks after registration (See for example [105].). No such study has been performed using our algorithm.

An approach which is a generalization of the previous one is to compare manual segmentations and automatic segmentations obtained with segmentation propagation. Using this method, an expert manually segments several structures in a set of images. One image is then selected as the target and each image of the set is registered with it. The manual segmentations of each image are then deformed using the corresponding displacement fields. At this point, all segmentations should have the same shape as the ones of the target. They can then be compared, the manual result of the target serving as ground truth (See for example [48].). We believe this approach may be better suited to evaluate the quality of high dimensional transformations such as the ones obtained using the demons algorithm (typically $3 \times 200^3 = 24 \times 10^6$ degrees of freedom).

Such a study has been performed previously by Dawant *et al.* [24] for the demons algorithm. To summarize their work, contours of different brain structures (the whole head, the cerebellum and the head of the caudate) have been segmented manually on nine MR images.

One of these images was mapped to all eight other images. Then, manual and propagated segmentations were compared. Their similarity index is defined as two times the area encircled by both contours divided by the sum of the areas encircled by each contour. This index ranges from zero to one, with zero indicating zero overlap and one indicating a perfect agreement between two contours. It is sensitive to both displacement and differences in shape and it is thus preferable to a simple area comparison. The average similarity indices between the manual and automatic segmentations was 0.96, 0.97 and 0.845 for the whole head, the cerebellum and the head of the caudate respectively. Compared with intra-rater results of 0.97, 0.97 and 0.88, the difference in the mean similarity indices between two manual delineations and between the manual delineations and the automatic segmentation method are statistically significant for the whole head and the caudate but not for the cerebellum. The authors put forth though that similarity indices over 0.85 correspond to contours that are virtually indistinguishable and that a more relevant comparison should be performed using inter-rater manual results which are known to have more discrepancies.

Concerning the physical relevance of the transformation, it should be pointed out that our algorithm does not explicitly make sure that the resulting transformation preserves the topology of S. In our experience on high resolution data, this problem does not seem to occur when using a sigma of 1 voxel to define the Gaussian filter used for smoothing the vector field. Still, this is a characteristic we would like to do without. Better regularization methods, such as proposed by Christensen *et al.* [19] or Bro-Nielsen and Gramkow [13] should provide more satisfying transformations, at least regarding singularities.

2.2.2 Modeling the Intensity Transformation

Previous to each iteration of the geometrical transformation an intensity correction is performed on S so that the intensities of its structures matches those in T, a requirement for the use of Equation 2.1. The intensity correction process starts by defining the set C of intensity couples from corresponding voxels of T and of the current resampled source image $S \circ h$, which will be designated by S in this section for simplicity. Hence, the set C is defined

as

$$C = \Big\{ \big(S(i), T(i)\big); 1 \leq i \leq N \Big\}, \tag{2.11}$$

where N is the number of voxels in the images. $S(i)$ and $T(i)$ correspond to the intensity value of the i^{th} voxel of S and T respectively when adopting the customary convention of considering images as one-dimensional arrays. From there, we show how to perform intensity correction if we can assume that a single intensity value in S has either 1) exactly one corresponding intensity value in T (monofunctional dependence) or 2) at least one and at most two corresponding intensity values in T (bifunctional dependence).

Monofunctional Dependence Assumption

Our goal is to model the transformation that characterizes the mapping from voxel intensities in S to those in T, knowing that some elements of C are erroneous, i.e. that would not be present in C if S and T were perfectly matched. If we can assume a monofunctional dependence of the intensities of T with regards to the those of S as well as additive stationary Gaussian white noise η on the intensity values of T, then we can adopt the model

$$T(i) = f(S(i)) + \eta(i), \tag{2.12}$$

where f is an unknown function to be estimated. This is exactly the model employed by Roche *et al.* [77, 76] which leads to the correlation ratio as the measure to be maximized for registration. In that approach, for a given transformation, the authors seek the function that best describes T in terms of S. They show that in a maximum likelihood context, the intensity function $\hat{f}$ that best approximates f is a least squares (LS) fit of T in terms of S.

The major difference between our respective problems is that we seek a high-dimensional geometrical transformation. As opposed to affine registration where the transformation is governed by the majority of good matches, we have seen in Section 2.2.1 that using the elastic registration model, displacements are found using mainly local information (i.e. gradients, local averages, etc.). Hence, we can not expect good displacements in one structure to correct for bad ones in another; we have to make certain each voxel is moved properly during each iteration. For this, since the geometrical transformation is found using intensity

similarity, the most precise intensity transformation is required. Consequently, instead of performing a standard least squares regression, we have opted for a robust linear regression estimator which will remove outlying elements of C during the estimation of the intensity transformation. To estimate f we use the least trimmed squares (LTS) method followed by a binary reweighted least squares (RLS) estimation [80]. The combination of these two methods provides a very robust regression technique with outlier detection, while ensuring that a maximum of pertinent points are used for the final estimation.

Least Trimmed Squares Computation For our particular problem, we will constrain ourselves the estimation of a polynomial function from the elements in C. We can then relate the intensity correspondences with a set of equations of the form

$$T(i) = \theta_0 + \theta_1 S(i) + \theta_2 S(i)^2 + \cdots + \theta_p S(i)^p, \tag{2.13}$$

where $\boldsymbol{\theta} = [\theta_0, \ldots, \theta_p]$ needs to be estimated and p is the degree of the polynomial function. A regression estimator will provide a $\hat{\boldsymbol{\theta}} = [\hat{\theta}_0, \ldots, \hat{\theta}_p]$ which can be used to predict the value of $T(i)$ from $S(i)$,

$$\hat{T}(i) = \hat{\theta}_0 + \hat{\theta}_1 S(i) + \hat{\theta}_2 S(i)^2 + \cdots + \hat{\theta}_p S(i)^p, \tag{2.14}$$

as well as the residual errors,

$$r(i) = T(i) - \hat{T}(i). \tag{2.15}$$

A popular method to obtain $\hat{\boldsymbol{\theta}}$ is to minimize the sum of squared residual errors,

$$\min_{\hat{\boldsymbol{\theta}}} \sum_{i=1}^{N} r(i)^2, \tag{2.16}$$

which leads to the standard LS solution. It is found by solving a linear system using the Singular Value Decomposition (SVD) method. See [76] for a more detailed study. This method is known to be very sensitive to outliers and thus is expected to provide a poor estimate of the monofunctional mapping from S to T. The LTS method solves this problem by minimizing the same sum on a subset of all residual errors, thus rejecting large ones

corresponding to outliers,

$$\min_{\hat{\boldsymbol{\theta}}} \sum_{i=1}^{c} \rho(i), \tag{2.17}$$

where $\rho(i)$ is the i^{th} smallest value of the set $\{r(1)^2, \ldots, r(N)^2\}$. This corresponds to a standard LS on the c values that best approximates the function we are looking for. Essentially, c/N represents the percentage of "good" points in C and must be at least $\frac{(N+p+2)}{2N}$, which is the breakdown value of the LTS method [79], i.e. the minimum percentage of points required for a proper estimate. A lesser value would allow to estimate parameters that model a minority of points which could then all be outliers. c will vary according to the modalities registered. The values used for our result and the corresponding modalities are discussed in Section 2.4.

We have not developed a procedure to find c automatically but have found reasonable *ad hoc* estimates that provide satisfactory results. A more in depth analysis of the influence of c on our results and its relation with different modalities is beyond the scope of this article, but we have found from visual inspection that a variation of c by 5% does not influence the registration result in a significant way.

Our method for LTS minimization is a simple iterative technique. First, we randomly pick c points from C. We then iterate between calculating $\hat{\boldsymbol{\theta}}$ using the standard LS technique on the selected points and choosing the c closest points from C. Recently, Rousseeuw and Van Driessen [79] proved that this method reduces the error on $\hat{\boldsymbol{\theta}}$ at each iteration. Hence we carry this process until $\sum_{i=1}^{c} \rho(i)$ stops decreasing, usually requiring less than 5 iterations. This provides adequate results for our purposes, Note that this finds a local minimum, although not guarantying the global minimum. Since we assume a good global registration previous to the estimation process, that might not make a large difference. Still, in the same paper, the authors also proposed a new efficient algorithm to find a good approximate solution of the LTS minimization. This strategy will be looked into in future implementations.

Reweighted Least Squares Computation Once $\hat{\boldsymbol{\theta}}$ is obtained using LTS, we can compute the standard error σ of our points with respect to our estimate. Of course, this value

will also be an estimate corresponding to

$$\hat{\sigma} = \sqrt{\frac{1}{KN}\sum_{i=1}^{c}\rho(i)}, \quad K = \frac{\int_{-\alpha}^{\alpha} x^2 g(x)\,dx}{\int_{-\alpha}^{\alpha} g(x)dx} = \frac{\int_{-\alpha}^{\alpha} x^2 g(x)dx}{c/N}, \tag{2.18}$$

where $g(x)$ is the normalized Gaussian distribution ($\mu = 0, \sigma^2 = 1$) and α is the $(0.5 + c/2N)^{\text{th}}$ quantile of $g(x)$. In Equation (2.18), K is a normalization factor introduced because $\sqrt{1/N\sum_{i=1}^{c}\rho(i)}$ is a consistent estimator of σ when the $\rho(i)$ are distributed like $N(0,\sigma^2)$. This is not the case in LTS regression since we only choose the c/N smallest $\rho(i)$.

Using this average deviation of the points from the estimates, we then perform an RLS regression by finding a new $\hat{\boldsymbol{\theta}}$ that minimizes the sum of squared residual for all points within $3\hat{\sigma}$ of the previous estimate,

$$\min_{\hat{\boldsymbol{\theta}}} \sum_{i=1}^{N} w_i\rho(i), \quad \text{where} \quad w_i = \begin{cases} 1 & \text{if } \rho(i) \leq 3\hat{\sigma}, \\ 0 & \text{otherwise.} \end{cases} \tag{2.19}$$

This optimizes the number of points used to compute $\hat{\boldsymbol{\theta}}$ by considering all the points that relate well to the LTS estimate, not only the best c/N.

Bifunctional Dependence Assumption

Functional dependence as expressed in Equation (2.12) implicitly assumes that two structures having similar intensity ranges in S should also have similar intensity ranges in T. With some combinations of multimodal images, this is a crude approximation. For example, ventricles and bones generally give similar response values in a MR T1 weighted image while they appear with very distinct values in a CT scan. Conversely, white and black matter are well contrasted in a T1 image while corresponding to similar intensities in a CT.

To circumvent this difficulty, we have developed a strategy that enables the mapping of an intensity value in S to not only one, but two possible intensity values in T. This method is a natural extension of the previous method. Instead of computing a single function that maps the intensities of S to those of T, two functions are estimated and the mapping becomes a weighted sum of these two functions.

We start with the assumption that if a point has an intensity s in S, the corresponding point in T has an intensity t that is normally distributed around two possible values depending on s, $f_{\boldsymbol{\theta}}(s)$ and $f_{\boldsymbol{\psi}}(s)$. In statistical terms, this means that given s, t is drawn from a mixture of Gaussian distribution,

$$P(t|s) = \pi_1(s)N(f_{\boldsymbol{\theta}}(s), \sigma^2) + \pi_2(s)N(f_{\boldsymbol{\psi}}(s), \sigma^2), \tag{2.20}$$

where $\pi_1(s)$ and $\pi_2(s) = 1 - \pi_1(s)$ are mixing proportions that depend on the intensity in the source image, and σ^2 represents the variance of the noise in the target image. Consistently with the functional case, we will restrict ourselves to polynomial intensity functions, i.e. $f_{\boldsymbol{\theta}}(s) = \theta_0 + \theta_1 s + \theta_2 s^2 + \cdots + \theta_p s^p$, and $f_{\boldsymbol{\psi}}(s) = \psi_0 + \psi_1 s + \psi_2 s^2 + \cdots + \psi_p s^p$.

An intuitive way to interpret this modeling is to state that for any voxel, there is a binary "selector" variable $\epsilon = \{1, 2\}$ that would tell us, if it was observed, which of the two functions $f_{\boldsymbol{\theta}}$ or $f_{\boldsymbol{\psi}}$ actually serves to map s to t. Without knowledge of ϵ, the best intensity correction to apply to S (in the minimum variance sense) is seen to be a weighted sum of the two functions,

$$f(s,t) = P(\epsilon = 1|s,t)f_{\boldsymbol{\theta}}(s) + P(\epsilon = 2|s,t)f_{\boldsymbol{\psi}}(s), \tag{2.21}$$

in which the weights correspond to the probability that the point be mapped according to either the first or the second function. Applying Bayes' law, we find that for $\epsilon = \{1, 2\}$:

$$P(\epsilon|s,t) = \frac{P(\epsilon|s)P(t|\epsilon,s)}{P(t|s)}, \tag{2.22}$$

and thus, using the fact that $P(\epsilon|s) = \pi_\epsilon(s)$ and $P(t|\epsilon,s) = G_\sigma(t - f_\epsilon(s))$, the weights are determined by

$$P(\epsilon|s,t) = \frac{\pi_\epsilon(s)\, G_\sigma(t - f_\epsilon(s))}{\pi_1(s)\, G_\sigma(t - f_{\boldsymbol{\theta}}(s)) + \pi_2(s)\, G_\sigma(t - f_{\boldsymbol{\psi}}(s))}, \tag{2.23}$$

where it should be clear from the context that $f_\epsilon \equiv f_{\boldsymbol{\theta}}$ if $\epsilon = 1$, and $f_\epsilon \equiv f_{\boldsymbol{\psi}}$ if $\epsilon = 2$.

In order to compute the intensity correction (Equation (2.21)), we now need to identify the parameters of our model, i.e. the polynomial coefficients $\boldsymbol{\theta}$ and $\boldsymbol{\psi}$, as well as the mixing proportions $\pi_1(s)$ and $\pi_2(s)$ and the variance σ^2. For this, we employ an ad hoc strategy that proceeds as follows.

First, $\boldsymbol{\theta}$ is estimated using the method described in Section 2.2.2. The points not used to compute $\boldsymbol{\theta}$, in a number between 0 and $N - c$, are used to estimate $\boldsymbol{\psi}$ still using the same method. Note that if this number is less than $10 \times p$, p being the polynomial degree, functional dependence is assumed and we fall back to the method described in the previous section.

This provides a natural estimation of the "selector" variable for each voxel: the n_1 points that were used to build $f_{\boldsymbol{\theta}}$ are likely to correspond to $\epsilon = 1$, while the n_2 points used to build $f_{\boldsymbol{\psi}}$ are likely to correspond to $\epsilon = 2$. Finally, the points that are rejected while estimating $\boldsymbol{\psi}$ are considered as bad intensity matches. A natural estimator for the variance σ^2 is then

$$\hat{\sigma}^2 = \frac{n_1}{n_1 + n_2}\hat{\sigma}_1^2 + \frac{n_2}{n_1 + n_2}\hat{\sigma}_2^2, \tag{2.24}$$

where $\hat{\sigma}_1^2$ and $\hat{\sigma}_2^2$ are the variances found respectively for $f_{\boldsymbol{\theta}}$ and $f_{\boldsymbol{\psi}}$ during the RLS regression (See Section 2.2.2.). Similarly, the mixing proportions are computed according to

$$\hat{\pi}_\epsilon(s) = \frac{n_\epsilon(s)}{n_1(s) + n_2(s)}, \qquad \epsilon = \{1, 2\}, \tag{2.25}$$

in which $n_\epsilon(s)$ is the number of voxels having an intensity s and used to build the function f_ϵ. Notice that in the case where $n_1(s) = n_2(s) = 0$ (i.e. no voxel corresponding to the intensity s has been taken into account in the computation of $f_{\boldsymbol{\theta}}$ or $f_{\boldsymbol{\psi}}$), then we arbitrarily set the mixing proportions to $\hat{\pi}_1(s) = \hat{\pi}_2(s) = 0.5$.

The intensity correction of S can now be performed by reinjecting the estimated parameters in Equations (2.23) and (2.21).

2.2.3 Combining the Intensity and Geometrical Transformations

As stated previously, the use of Equation 2.1 in Section 2.2.1 to model geometrical transformations makes the assumption that the intensities of structures in S matches those in T. When dealing with images obtained from different modalities, this requirement is not met. To solve this problem, we presented in Section 2.2.2 a method to rectify intensity differences between corresponding structures in S and T using an underlying monofunctional or bifunctional model. The result of this intensity correction on S for the n^{th} iteration will be denoted

by $S_n^\star$ with $S_0^\star = S$. Considering this and Equation 2.1, the geometrical transformation is found using

$$v_{n+1}(x) = G_\sigma \otimes \left(v_n + \frac{S_n^\star \circ h_n(x) - T(x)}{||\nabla(S_n^\star \circ h_n)(x)||^2 + [S_n^\star \circ h_n(x) - T(x)]^2} \nabla(S_n^\star \circ h_n)(x) \right). \quad (2.26)$$

The reader might wonder why we restricted our technique to estimating at most two functions. In theory, our technique can well accommodate for more than two. The problem encountered regards finding proper values for c, i.e. the number of points used for the LTS computation of each function. As mentioned previously, c needs to be at least $(N+p+2)/2$ for the first polynomial. The number of points available to compute the second function are then at most $(N-p-2)/2$ and may well be less due to the RLS regression. This means that at best, less than 25% of all points would be available to compute a third function, 12.5% for a fourth function, and so on. We expect that the intensity correspondences reflected by these third and fourth functions would not be of real value, especially during the first iterations of the registration process, where the number of outliers in C in at its highest.

2.2.4 Mutual Information

Another approach we tested to compute incremental displacements was inspired by the works of Viola *et al.* [102] and Maes *et al.* [62]. In these approaches, the rigid/affine registration between two images is formulated as a maximization of their MI. This choice is motivated by the fact that MI models the similarity between the images while resorting to assumptions that are much more general than functional dependence. Consequently, and contrary to the approach that was presented in Section 2.2.2, they do not attempt to apply an intensity correction to one image so that it matches the other. Instead, they model the intensity dependence in a purely statistical fashion. Viola *et al.* [102] do this modeling using Parzen windowing, which enables them to differentiate the MI criterion with respect to the geometrical transformation.

As shown in Section 2.2.1, our incremental displacements closely relate with a gradient descent on the SSD criterion. Using this analogy, we implemented an alternative matching strategy where the incremental displacements given by Equation (2.1) are replaced with the

following formula,

$$v_{n+1}(x) = G_\sigma \otimes (v_n + \alpha \nabla MI(v_n)), \tag{2.27}$$

in which α is a positive constant and $\nabla MI(v_n)$ is the gradient of the MI criterion with respect to the n^{th} displacement vector, whose mathematical expression is found in [102]. This updating corresponds to a first order gradient descent on the MI criterion, of course up to the Gaussian filtering which is used as a regularization constraint.

Non-rigid registration results using mutual information as presented here are shown in Section 2.4.3.

2.3 Data

Most of the data used in the following experiments were obtained from BrainWeb [11, 20]. This tool uses an atlas [23] with a resolution of $1 \times 1 \times 1\text{mm}^3$ comprising nine segmented regions (See Table 2.1.) from which T1, T2 and PD images can be generated [58]. We made use of the discrete phantom atlas and of three simulated MR images, one of each modality, with the same resolution as the atlas, 5% noise and no intensity non-uniformity. Since they are generated from the same atlas, they represent the same underlying anatomy and are all perfectly matched.

Tissue type	Intensity	Tissue type	Intensity
Background	0	Muscle / Skin	140
CSF	28	Skin	168
Gray Matter	56	Skull	196
White Matter	84	Glial Matter	224
Fat	112	Connective	252

Table 2.1: Intensity values corresponding to the different tissue types present in the discrete phantom atlas.

We also made use of a T1 MR image and a CT image, both from different subjects and having a resolution of $1 \times 1 \times 1\text{mm}^3$. Both these images were affinely registered with the

atlas using the correlation ratio method [78]. To differentiate the T1 image obtained with the atlas from the other T1 image, the latter will be referenced as SCH.

The images all respect the neurological convention, i.e. on coronal and axial slices, the patient's left is on the left side of the image.

2.4 Results and Discussion

In the following section we present registration results involving images obtained from several different kinds of modalities. First, we show a typical example where monofunctional dependence can be assumed: registration of an atlas with an MR image. Then, more practical examples are shown where images from different modalities are registered and where bifunctional dependence may be assumed. We also provide registration results obtained from our implementation of MI maximization as described in Section 2.2.4.

The multilevel process was performed at three resolution levels, namely 4mm, 2mm and 1mm per voxel. Displacement fields at one level are initialized from the result of the previous level. The initial displacement field v_0 is set to a zero. 128 iterations are performed at 4mm/voxel, 32 at 2mm/voxel and 8 at 1mm/voxel. These are twice the number of iterations used for registration of monomodal images using the conventional demons algorithm. We believe that making use of a better stopping criterion, such as the difference of the SSD values between iterations, would probably improve the results shown below but this aspect has not been investigated. It should be in future implementations. The Gaussian filter G_σ used to smooth the displacement field has a standard deviation of 1 voxel regardless of the resolution. This models stronger constraints on the deformation field at the beginning of the registration process to correct for gross displacements, and weaker constraints near the end when fine displacements are sought.

2.4.1 Monofunctional Dependence

We present here the result of registering the atlas with SCH. Since the atlas can be used to generate realistic MR images, it is safe to assume a functional dependence between the

intensity of the atlas and those of SCH. Also, since SCH and the atlas are well aligned due to the affine registration, we have roughly estimated that the number of points already well matched, i.e. the number of good points in C, are at least $0.80 \times N$, to which we have set the value of c. Since 10 classes are present in the atlas, the polynomial degree chosen was set to 9.

The result of registration is presented in Figures 2.1, 2.2 and 2.3. The first image (a) shows slices of the atlas. The second one (b) is the corresponding slice of SCH. The third and fourth images (c and d) present the result of registering the atlas with SCH using our algorithm. The third one (c) shows the result without the intensity transformation; we have simply applied to the atlas the geometrical transformation resulting from the registration procedure. The fourth image (d) shows the image resulting from the registration process. It has the same shape as the resampled atlas and intensities have been transformed using the intensity correction.

As can be seen, there is one obvious problem with this result: although the shape of the atlas seems well corrected, the CSF intensity is not, as can be seen in the ventricles and around the cortex (See arrows in Figures 2.1(b), 2.2(b) and 2.3(b).). This reflects on the matching, as can be observed around the anterior aspect of the lateral ventricles on Figure 2.2(b).

This problem can also be observed by looking at the intensity transformation function presented in Figure 2.4 (Intensity values corresponding to the different tissue types present in the atlas are shown in Table 2.1.). This is due to a spatial overlap of the CSF in the atlas and the gray and white matter in SCH, especially around the cortical area which is known to present large variations between subjects. We believe this is due to the strong smoothness constraints imposed by the Gaussian regularization which may prevent the assessment of large and uneven displacements required to match the cortex.

To verify this assumption, we registered T1 with SCH and deformed T1 using the resulting displacement field. This provided an image SCH' that closely resembles SCH (Compare Figure 2.1(b) with Figure 2.5(b), Figure 2.2(b) with Figure 2.6(b) and Figure 2.3(b) with Figure 2.7(b)) and for which we are assured that the shape variation from the atlas can be assessed by our algorithm. We then registered the atlas with SCH'. This result is presented in

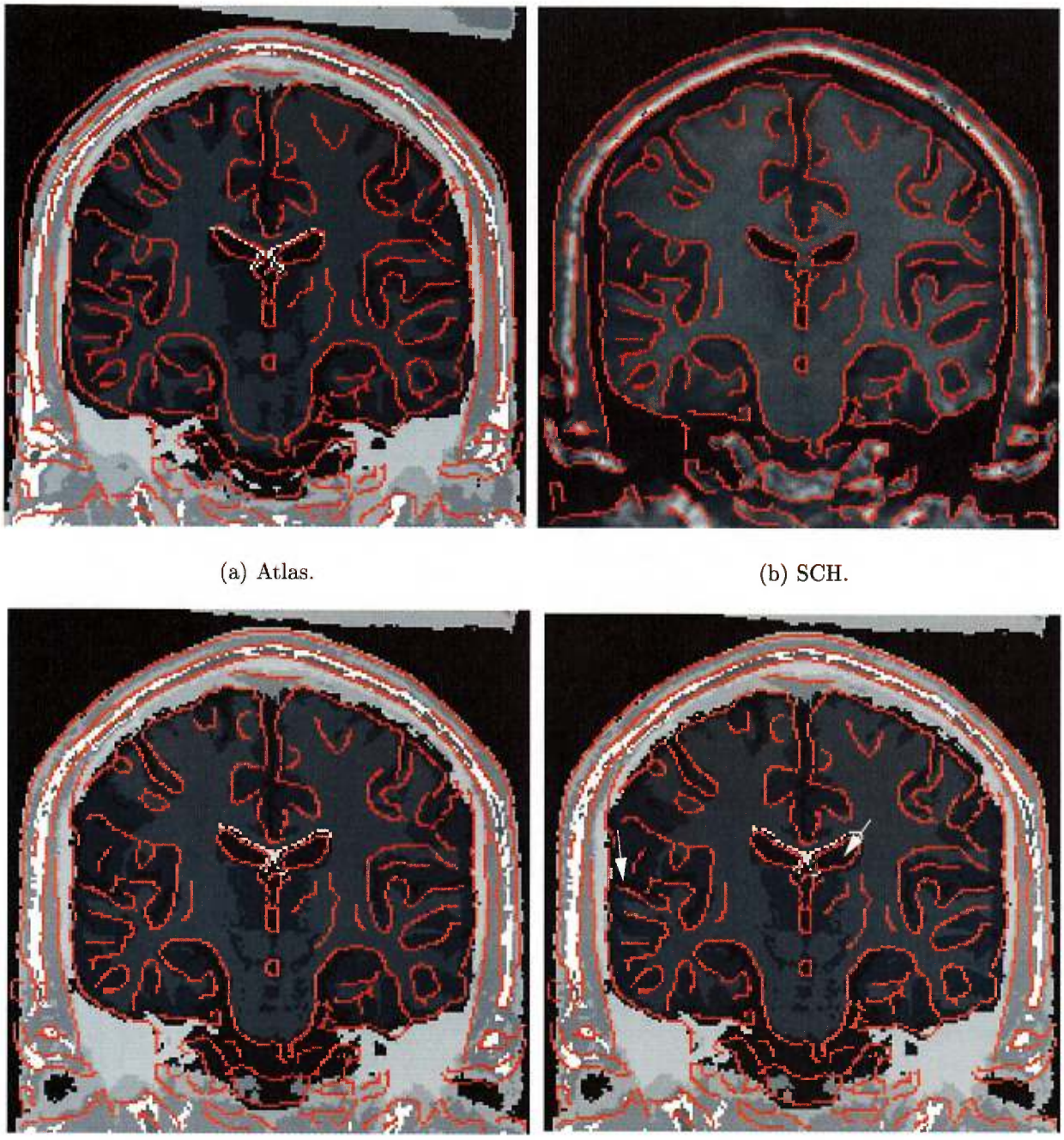

(a) Atlas.

(b) SCH.

(c) Atlas without intensity correction after registration with SCH

(d) Atlas with intensity correction after registration with SCH.

Figure 2.1: Corresponding coronal slices of the atlas to SCH registration result. Contours were obtained using a Canny-Deriche edge detector on SCH (Figure 2.1(b)) and overlaid on the other images to better assess the quality of registration. Arrows point to examples of bad intensity correction.

(a) Atlas.

(b) SCH.

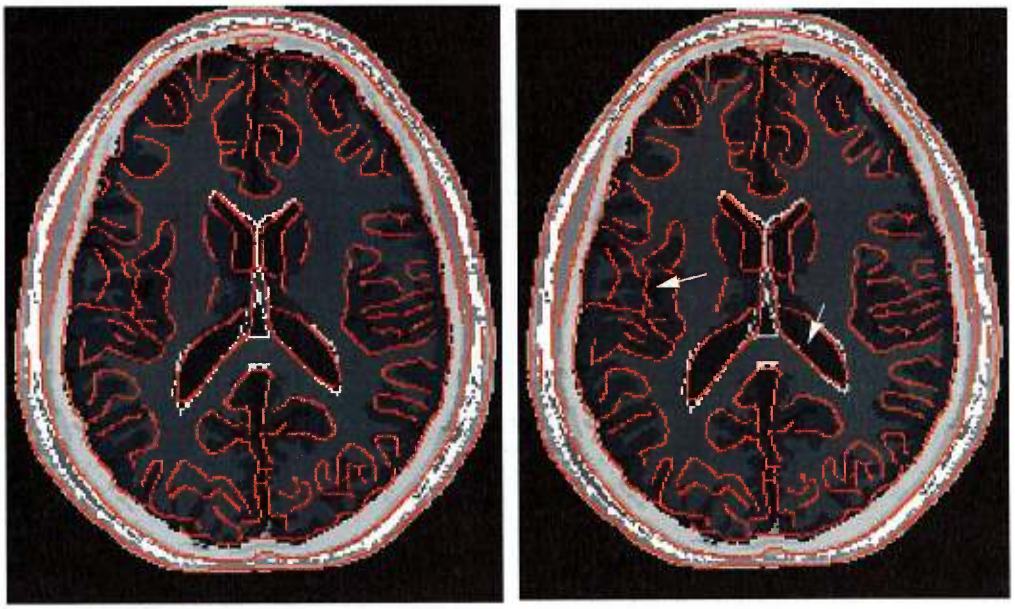

(c) Atlas without intensity correction after registration with SCH

(d) Atlas with intensity correction after registration with SCH.

Figure 2.2: Corresponding axial slices of the atlas to SCH registration result. Contours were obtained using a Canny-Deriche edge detector on SCH (Figure 2.2(b)) and overlaid on the other images to better assess the quality of registration. Arrows point to examples of bad intensity correction.

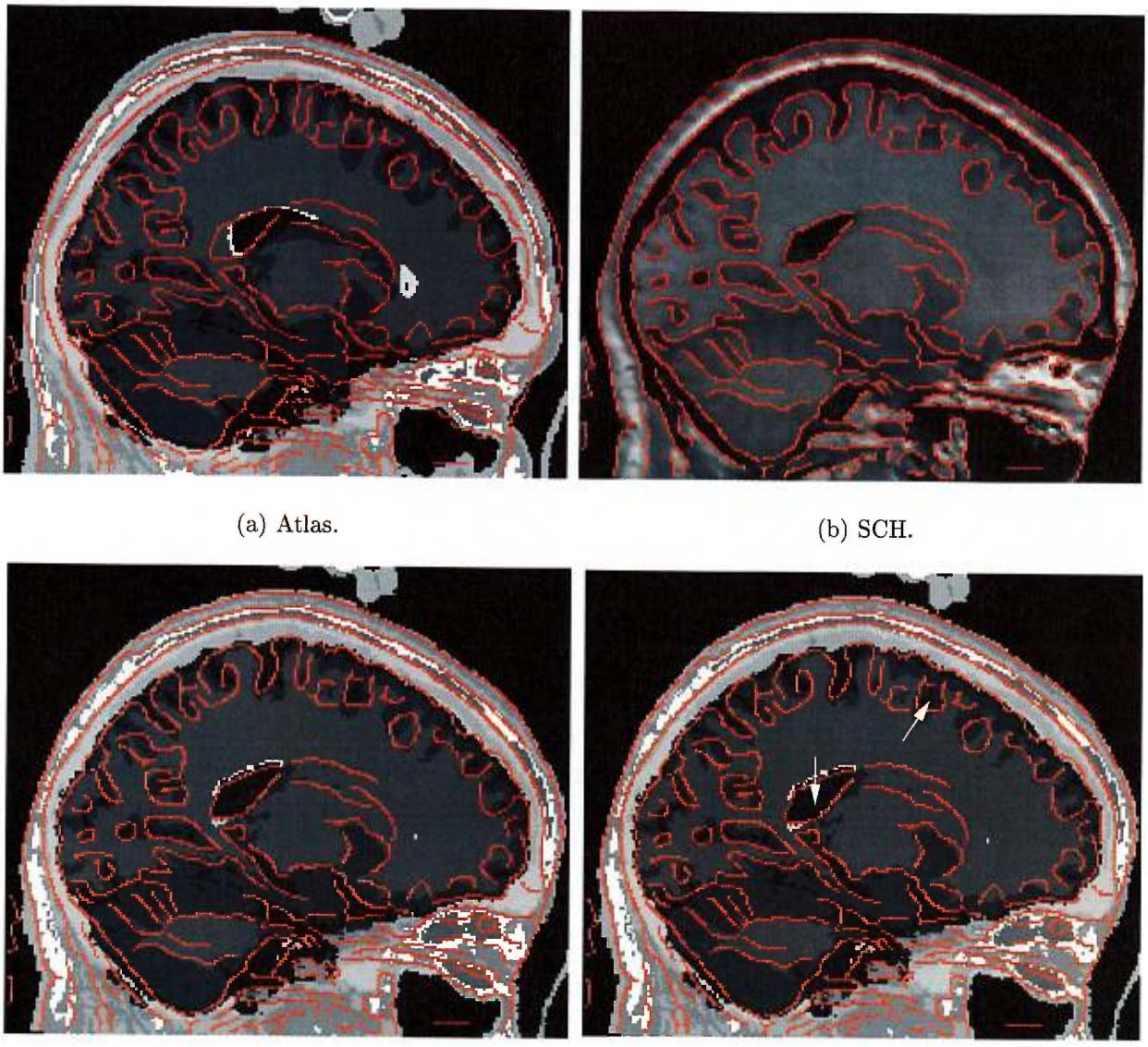

(a) Atlas.

(b) SCH.

(c) Atlas without intensity correction after registration with SCH

(d) Atlas with intensity correction after registration with SCH.

Figure 2.3: Corresponding sagittal slices of the atlas to SCH registration result. Contours were obtained using a Canny-Deriche edge detector on SCH (Figure 2.3(b)) and overlaid on the other images to better assess the quality of registration. Arrows point to examples of bad intensity correction.

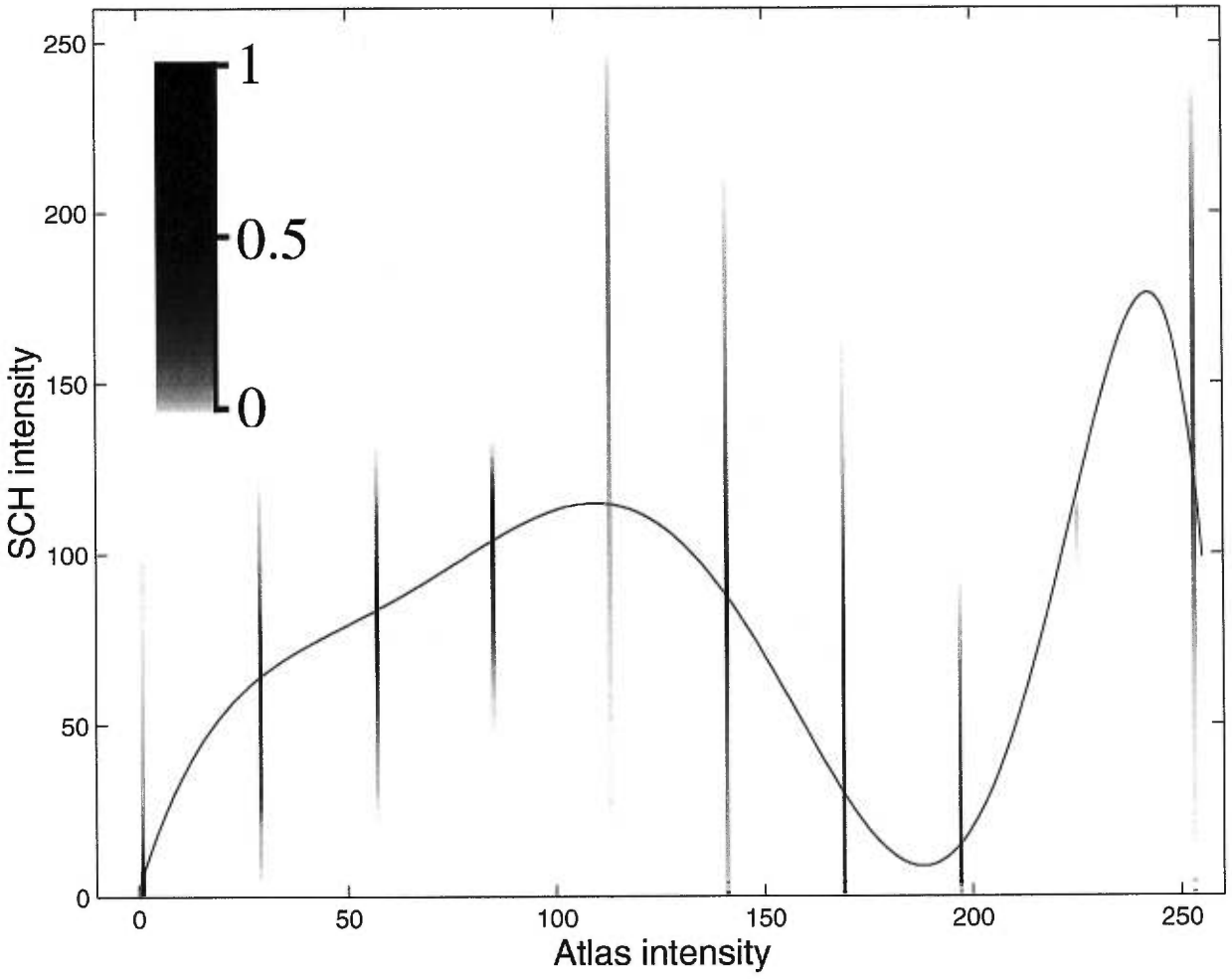

Figure 2.4: Intensity transformation found by registering the atlas with SCH and assuming monofunctional dependence. The function f is overlaid on the joint histogram of the two images after registration. The joint histogram values have been compressed logarithmically and normalized as is depicted in the color scale. The tissue types corresponding to the different atlas intensities are presented in Table 2.1.

Figures 2.5, 2.6 and 2.7. As can be observed, the CSF intensity value is now well corrected. By looking at the intensity transformation shown in Figure 2.8, we also notice that each atlas structure has corresponding intensity ranges in SCH that are less extended as those of Figure 2.4, reflecting a better match between the images. This finding puts forth that the displacement field regularization has to be able to accommodate the large uneven displacement of the cortex. To cope with large displacements, Gaussian filtering may probably be replaced with another regularization strategy such as that based on a fluid model [19] or on a non-quadratic potential energy [49].

Another difference between Figures 2.4 and 2.8 is the difference in the intensity mapping of the glial matter (Intensity 224 in the atlas.). This structure forms a small envelope around the ventricles and is represented by so few points that they are considered as outliers. This could be corrected by considering more points during the intensity transformation. In fact, c should be increased at each iteration to reflect that, during registration, S gradually aligns with T and more points in C can be considered as well matched.

2.4.2 Bifunctional Dependence

When registering images from different modalities, monofunctional dependence may not necessarily be assumed. Here, we applied the method described in Section 2.2.2 where two polynomial functions of degree 12 are estimated. This number was set arbitrarily to a relatively high value to enable important intensity transformations.

Figures 2.9, 2.10 and 2.11 present the result of registering T1 with CT. Using these last two modalities, most intensities of T1 should be mapped to gray and only the skull, representing a small portion of the image data, should be mapped to white. After affine registration almost all voxels are well matched, i.e. the number of good points in C is large. Hence, in this particular case, we have chosen a high value for c set to $0.90 \times N$.

As we can see in Figures 2.9, 2.10 and 2.11, the skull, shown in black in the MR image and in white in the CT scan, is well registered and the intensity transformation adequate. Figure 2.12(a) presents the joint histogram of the two images after registration. This histogram is color-coded and ranges from red representing high point densities to blue depicting

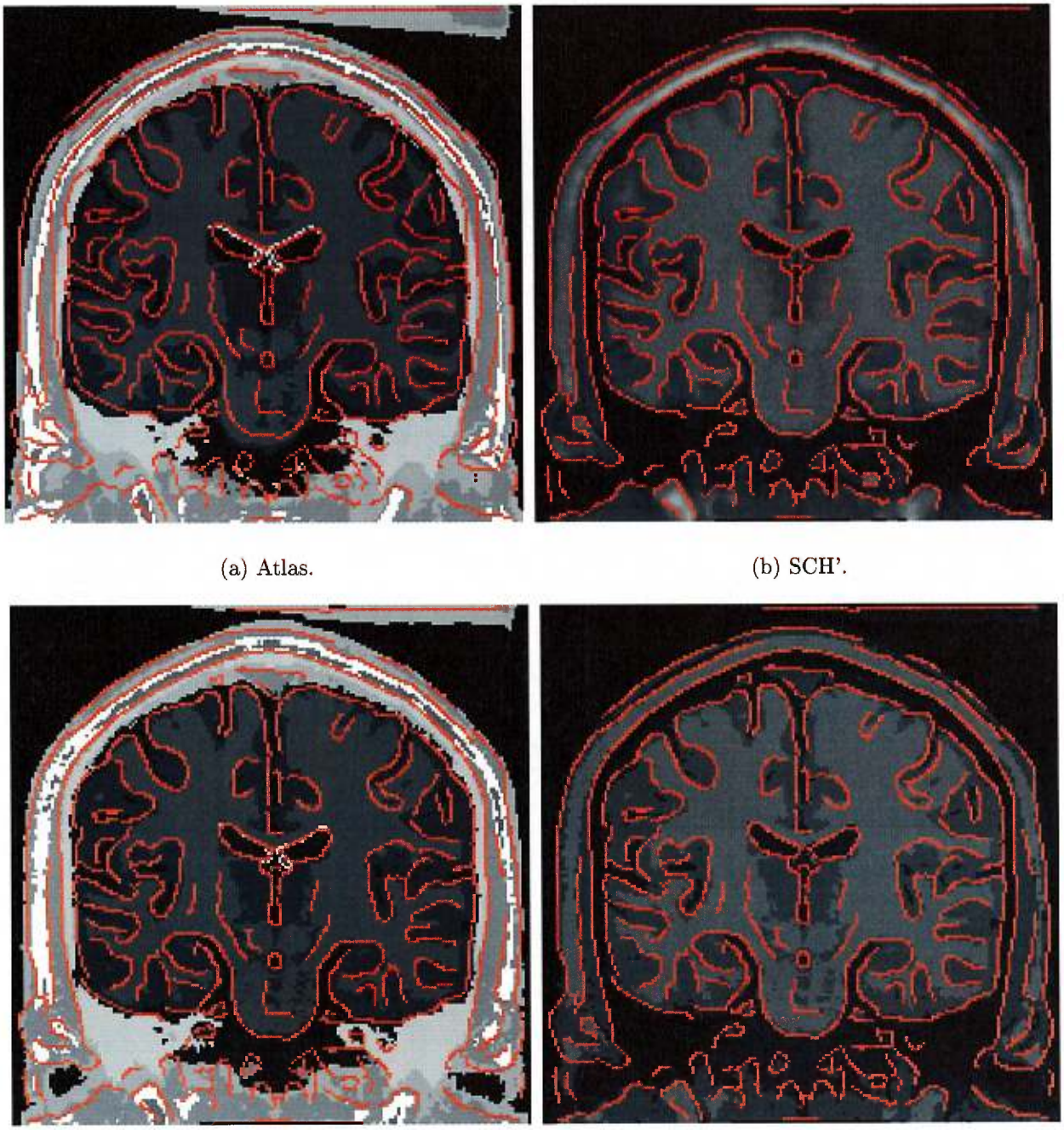

(a) Atlas.

(b) SCH'.

(c) Atlas without intensity correction after registration with SCH'.

(d) Atlas with intensity correction after registration with SCH'.

Figure 2.5: Corresponding coronal slices of the atlas to SCH' registration result. Contours were obtained using a Canny-Deriche edge detector on SCH' (Figure 2.5(b)) and overlaid on the other images to better assess the quality of registration.

(a) Atlas.

(b) SCH'.

(c) Atlas without intensity correction after registration with SCH'.

(d) Atlas with intensity correction after registration with SCH'.

Figure 2.6: Corresponding axial slices of the atlas to SCH' registration result. Contours were obtained using a Canny-Deriche edge detector on SCH' (Figure 2.6(b)) and overlaid on the other images to better assess the quality of registration.

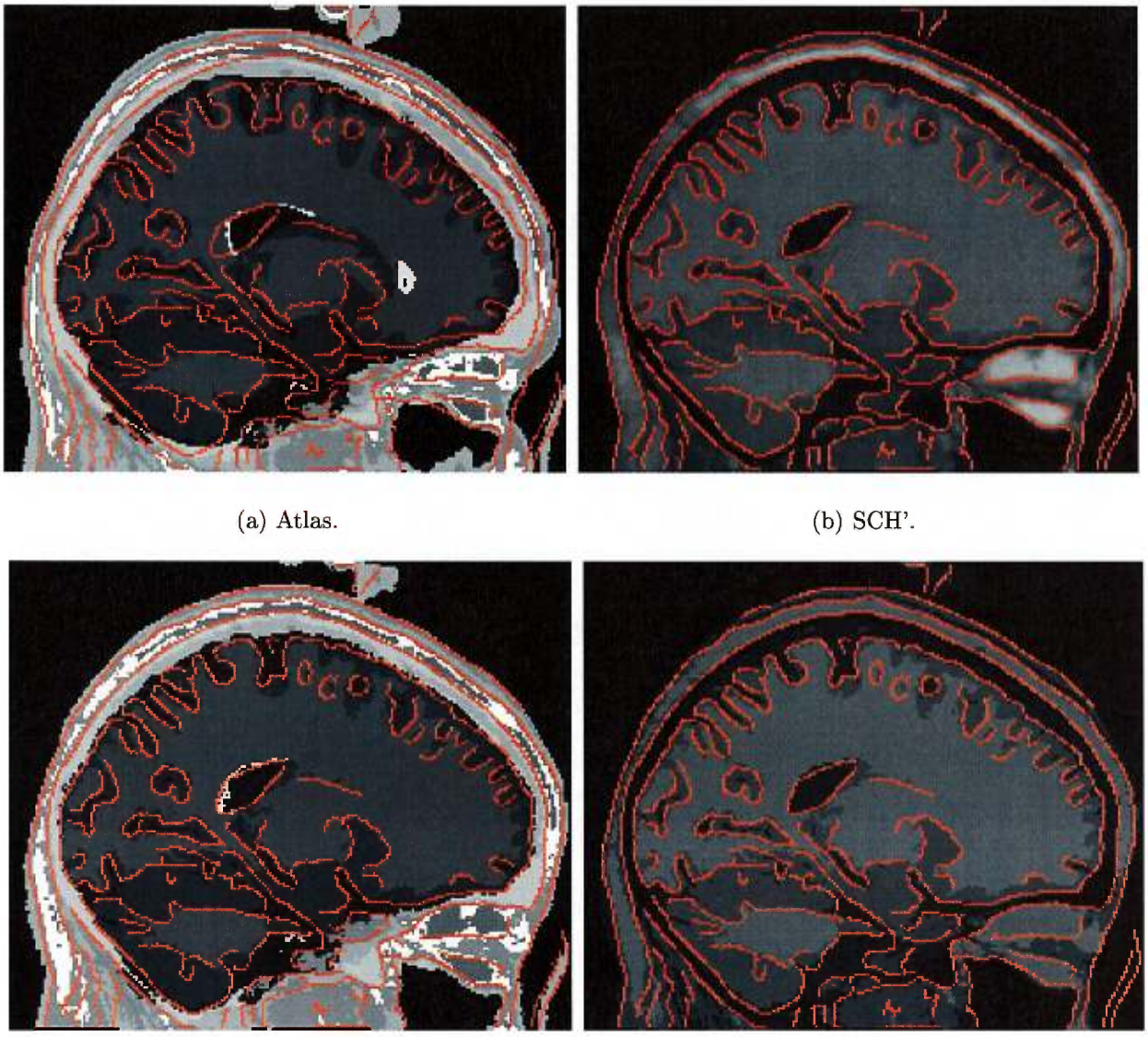

(a) Atlas.

(b) SCH'.

(c) Atlas without intensity correction after registration with SCH'.

(d) Atlas with intensity correction after registration with SCH'.

Figure 2.7: Corresponding sagittal slices of the atlas to SCH' registration result. Contours were obtained using a Canny-Deriche edge detector on SCH' (Figure 2.7(b)) and overlaid on the other images to better assess the quality of registration.

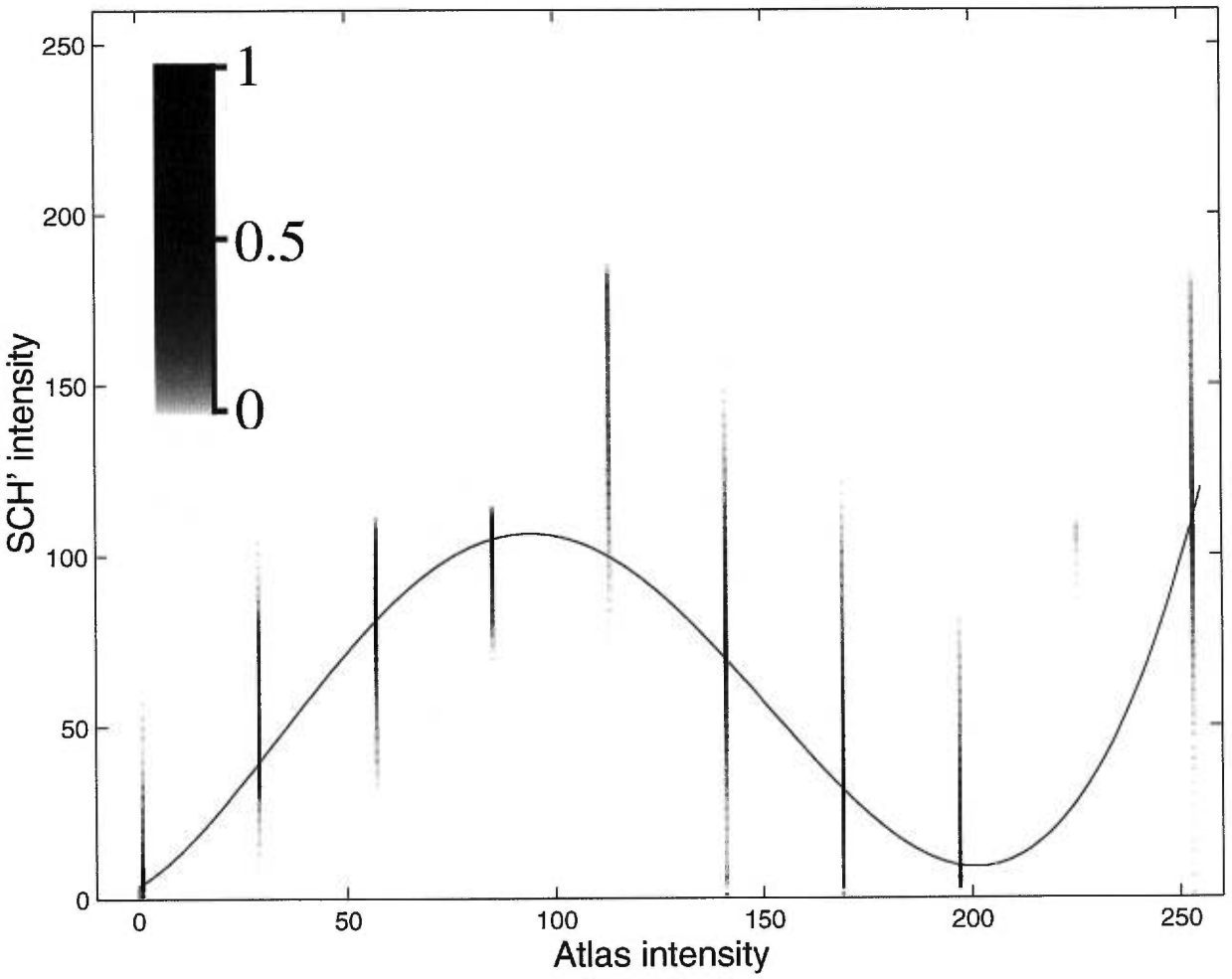

Figure 2.8: Intensity transformation found by registering the atlas with SCH' and assuming monofunctional dependence. The function f is overlaid on the joint histogram of the two images after registration. The joint histogram values have been compressed logarithmically and normalized as is depicted in the color scale. The tissue types corresponding to the different atlas intensities are presented in Table 2.1.

low point densities. Figure 2.12(b) presents the functions f_{θ} and f_{ψ} found during the registration process. The red line corresponds to f_{θ} and the blue one to f_{ψ}. The line width for a given intensity s is proportional to the value of the corresponding $\pi_{\epsilon}(s)$. The gray values represent the joint histogram after registration.

As can be observed in Figure 2.12(b), the polynomials found fit well with the high density clusters of the joint histogram. Still, some points need to be addressed.

We can observe that due to the restricted polynomial degree, f_{θ}, (shown in red) oscillates around the CT gray value instead of fitting a straight line. This is reflected in the intensity corrected image, shown in Figures 2.9(d), 2.10(d) and 2.11(d), where the underlying anatomy can still be observed by small intensity variations inside the skull. This artifact has insubstantial consequences during the registration process since the difference between most of the voxels of T and S is 0, resulting in null displacements. The displacements driving the deformation will be those of the skull and the skin contours, and will be propagated in the rest of the image with the Gaussian filtering of the displacement field.

We also notice that f_{ψ} (shown in blue), which is mainly responsible for the mapping of the skull, does not properly model the cluster it represents for intensities smaller than 5. The mapping for these intensities is slightly underestimated. This may have two causes. First, as in the previous case, it might be due to the restricted polynomial degree. Second, we can notice that some of the background values in T1 that have an intensity close to 0 are mapped to gray values in the CT which correspond to soft tissues. This means that some of the background in the T1 is matched with the skin in the CT. This has the effect of "pulling" f_{ψ} closer to the small cluster positioned around (2,65). If the underestimation of f_{ψ} arises because of the second reason, letting the algorithm iterate longer might provide a better result.

In Figures 2.13, 2.14 and 2.15 and in Figures 2.17, 2.18 and 2.19, we present the result of registering T2 and PD respectively with SCH. Figures 2.16 and 2.20 show the corresponding intensity transformations. For these experiments, c was set to $0.60 \times N$, a value we have found to be effective for these types of modalities after affine registration.

One observation that can be made by looking at the joint histograms of Figures 2.16(a) and 2.20(a) is that there seems to be a functional dependence between the images intensities,

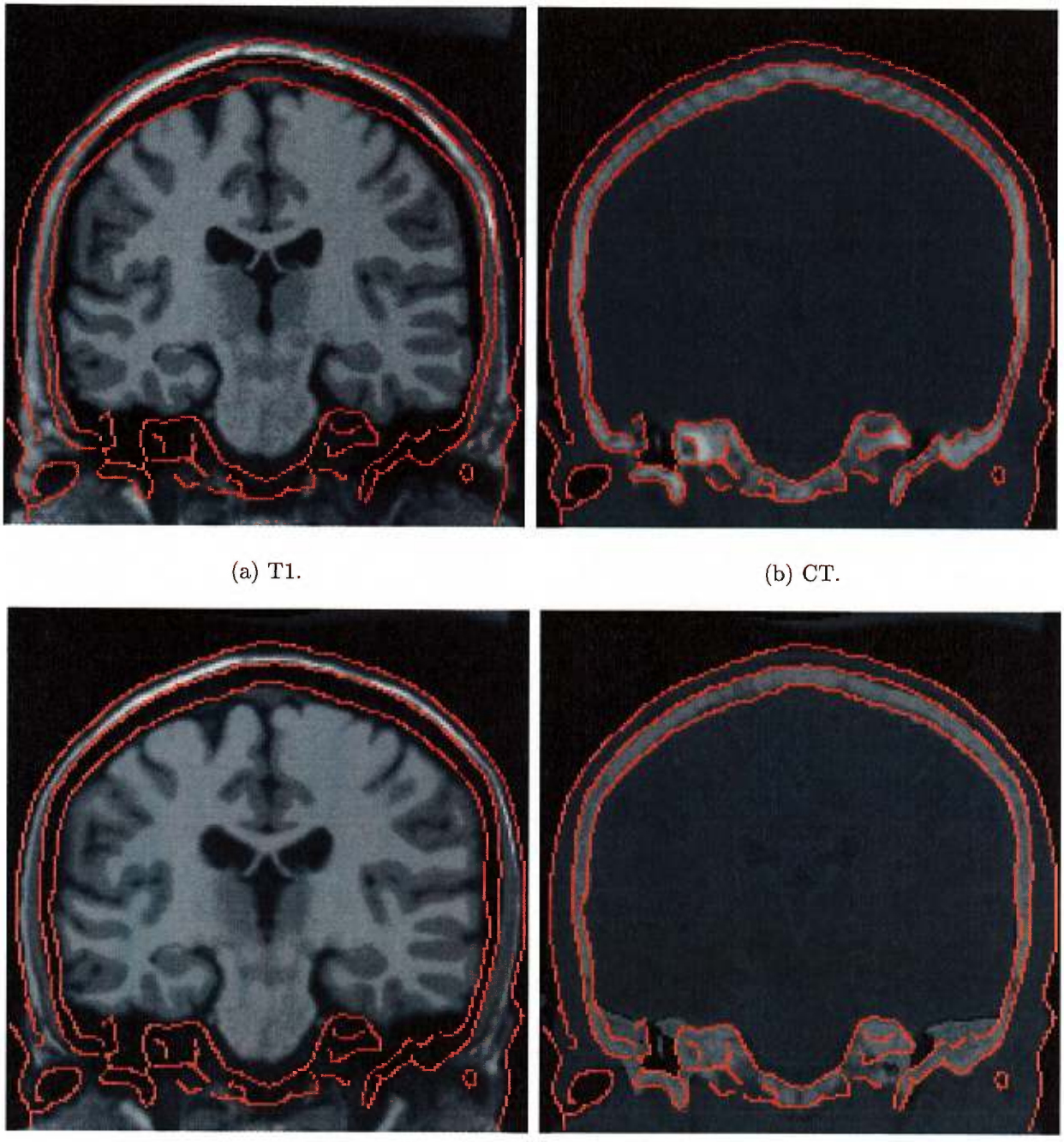

(a) T1.

(b) CT.

(c) T1 without intensity correction after registration with CT.

(d) T1 with intensity correction after registration with CT.

Figure 2.9: Corresponding coronal slices of T1 to CT registration result. Contours were obtained using a Canny-Deriche edge detector on CT (Figure 2.9(b)) and overlaid on the other images to better assess the quality of registration.

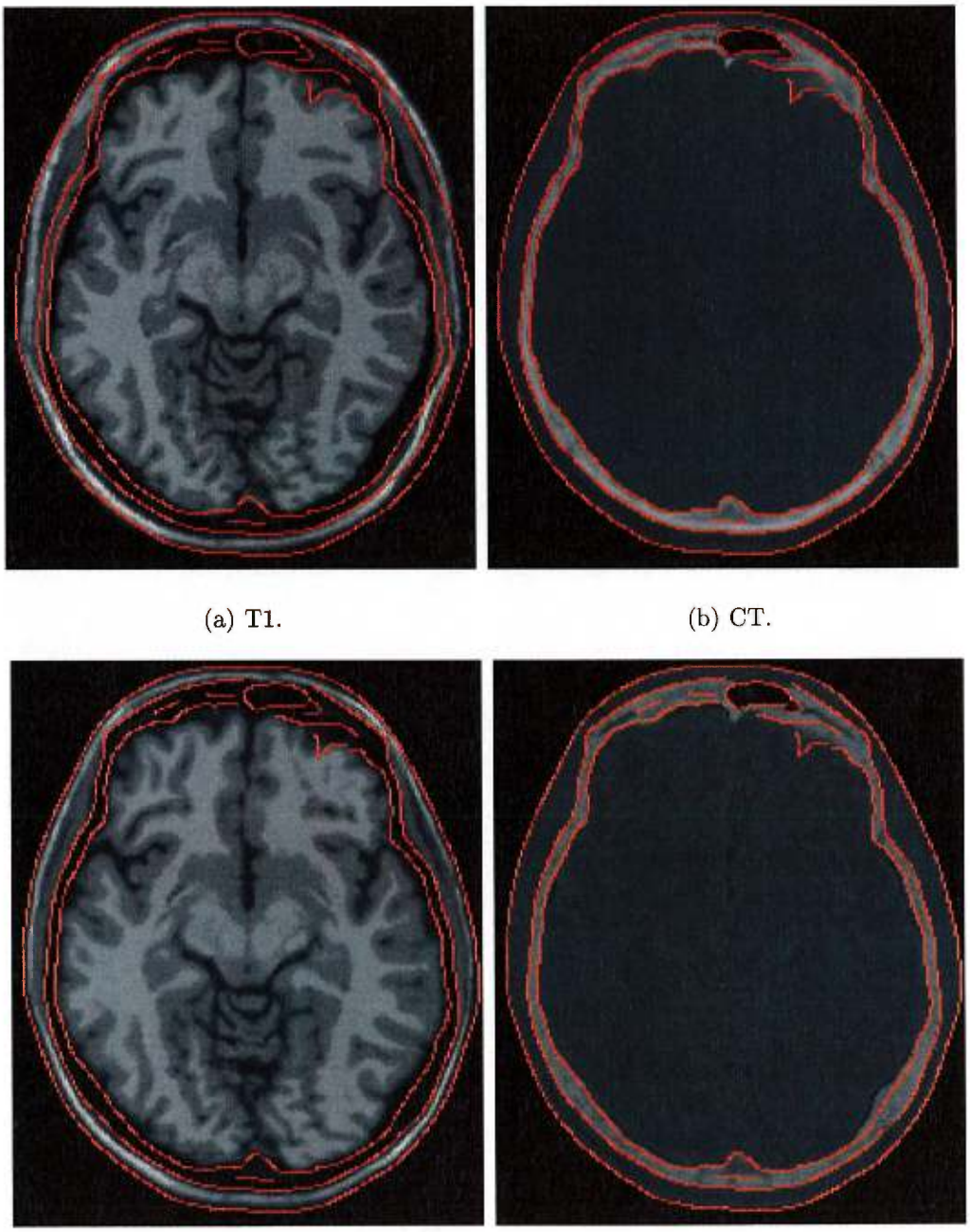

(a) T1.

(b) CT.

(c) T1 with intensity correction after registration with CT.

(d) T1 without intensity correction after registration with CT.

Figure 2.10: Corresponding axial slices of T1 to CT registration result. Contours were obtained using a Canny-Deriche edge detector on CT (Figure 2.10(b)) and overlaid on the other images to better assess the quality of registration.

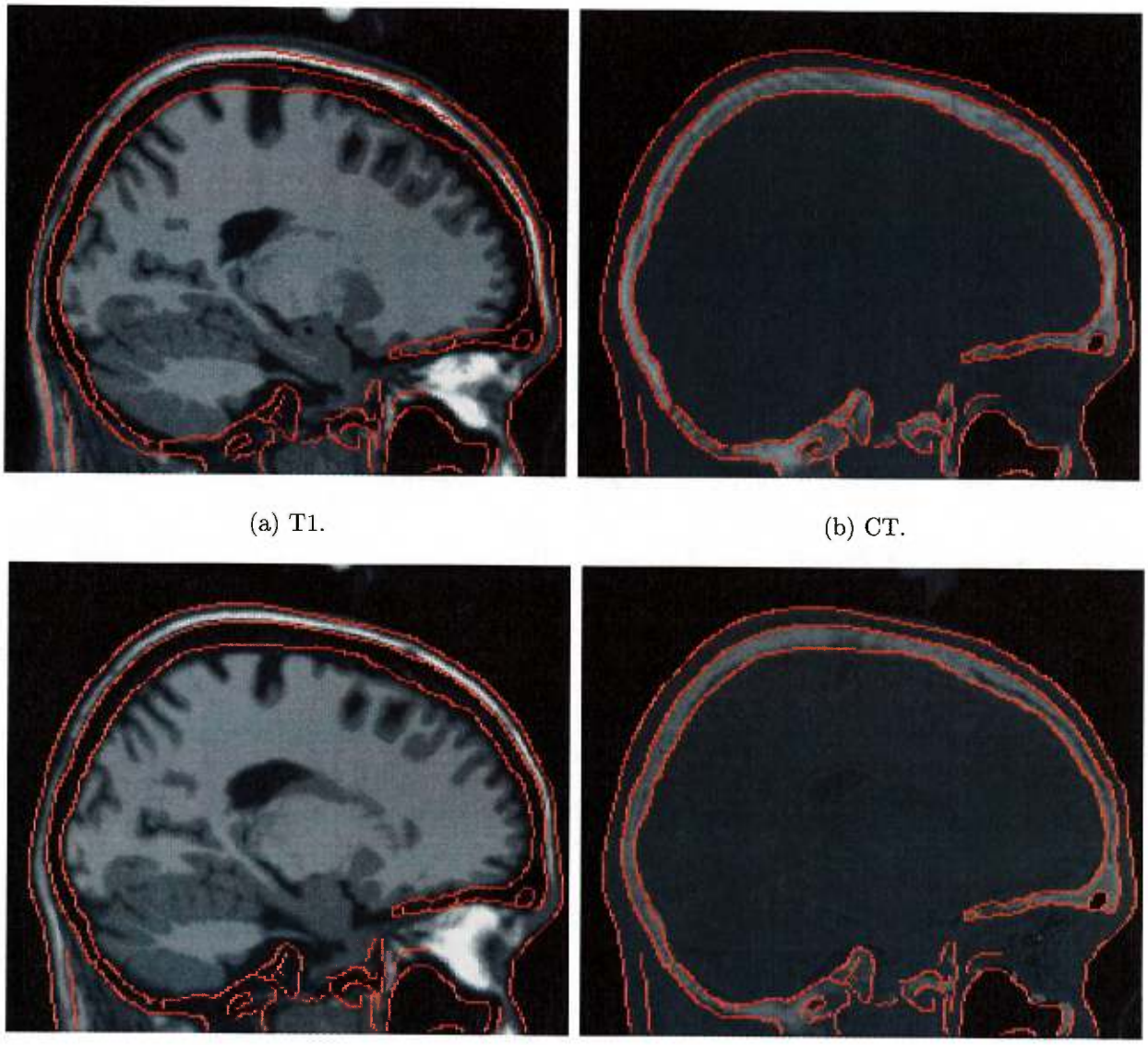

(a) T1.

(b) CT.

(c) T1 without intensity correction after registration with CT.

(d) T1 with intensity correction after registration with CT.

Figure 2.11: Corresponding sagittal slices of T1 to CT registration result. Contours were obtained using a Canny-Deriche edge detector on CT (Figure 2.11(b)) and overlaid on the other images to better assess the quality of registration.

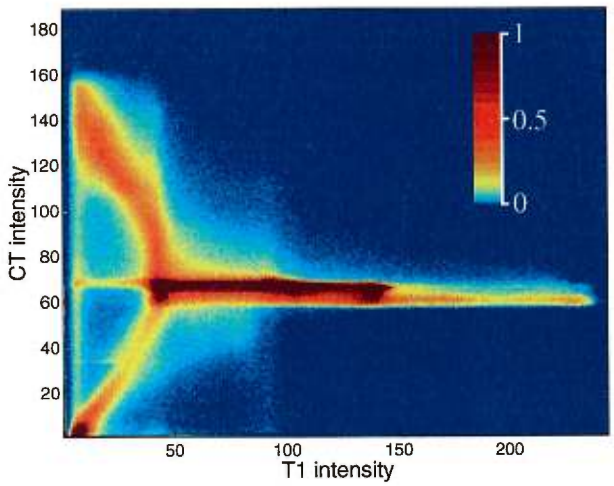

(a) The joint histogram of T1 and CT after registration. The joint histogram values have been compressed logarithmically and normalized as is depicted in the color scale. Values range from red representing high point densities to blue depicting low point densities.

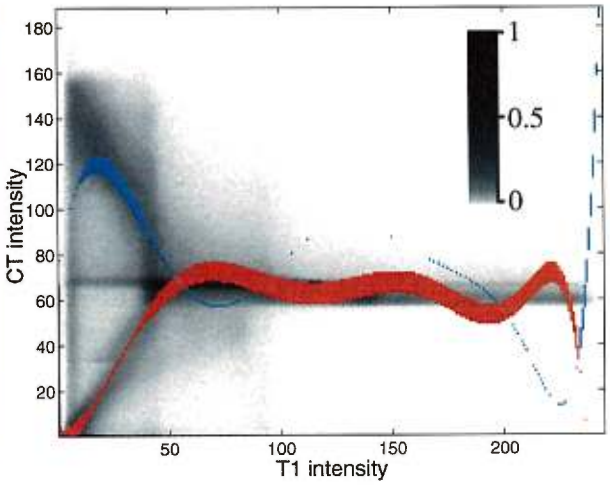

(b) The red line corresponds to f_θ and the blue one to f_ψ. The line width for a given intensity value s in T1 corresponds to the value of the corresponding $\pi_\epsilon(s)$. The gray values represent the joint histogram after registration.

Figure 2.12: Intensity transformation found when registering T1 with CT and assuming bifunctional dependence.

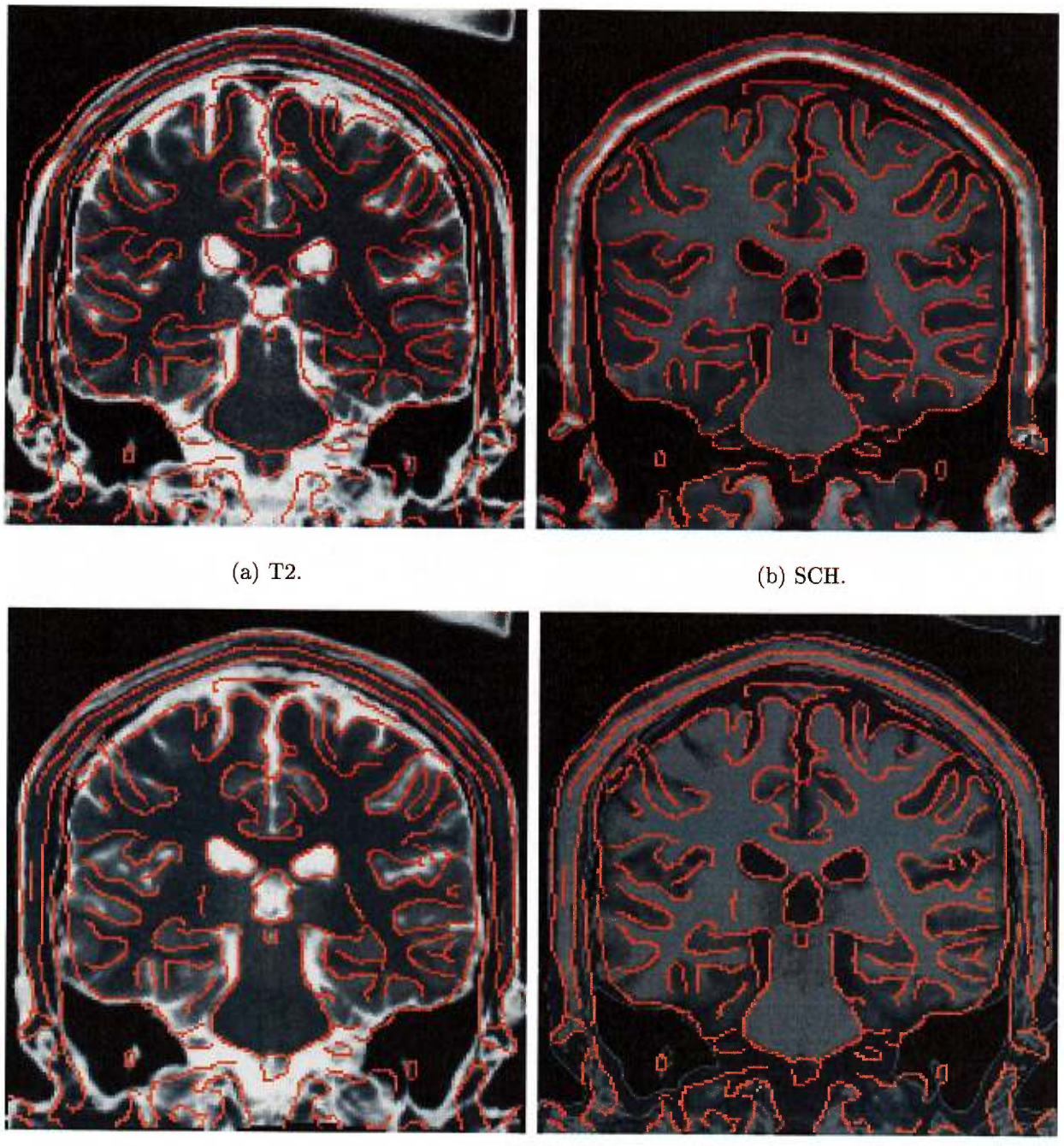

(a) T2.

(b) SCH.

(c) T2 without intensity correction after registration with SCH.

(d) T2 with intensity correction after registration with SCH.

Figure 2.13: Corresponding coronal slices of T2 to SCH registration result. Contours were obtained using a Canny-Deriche edge detector on SCH (Figure 2.13(b)) and overlaid on the other images to better assess the quality of registration.

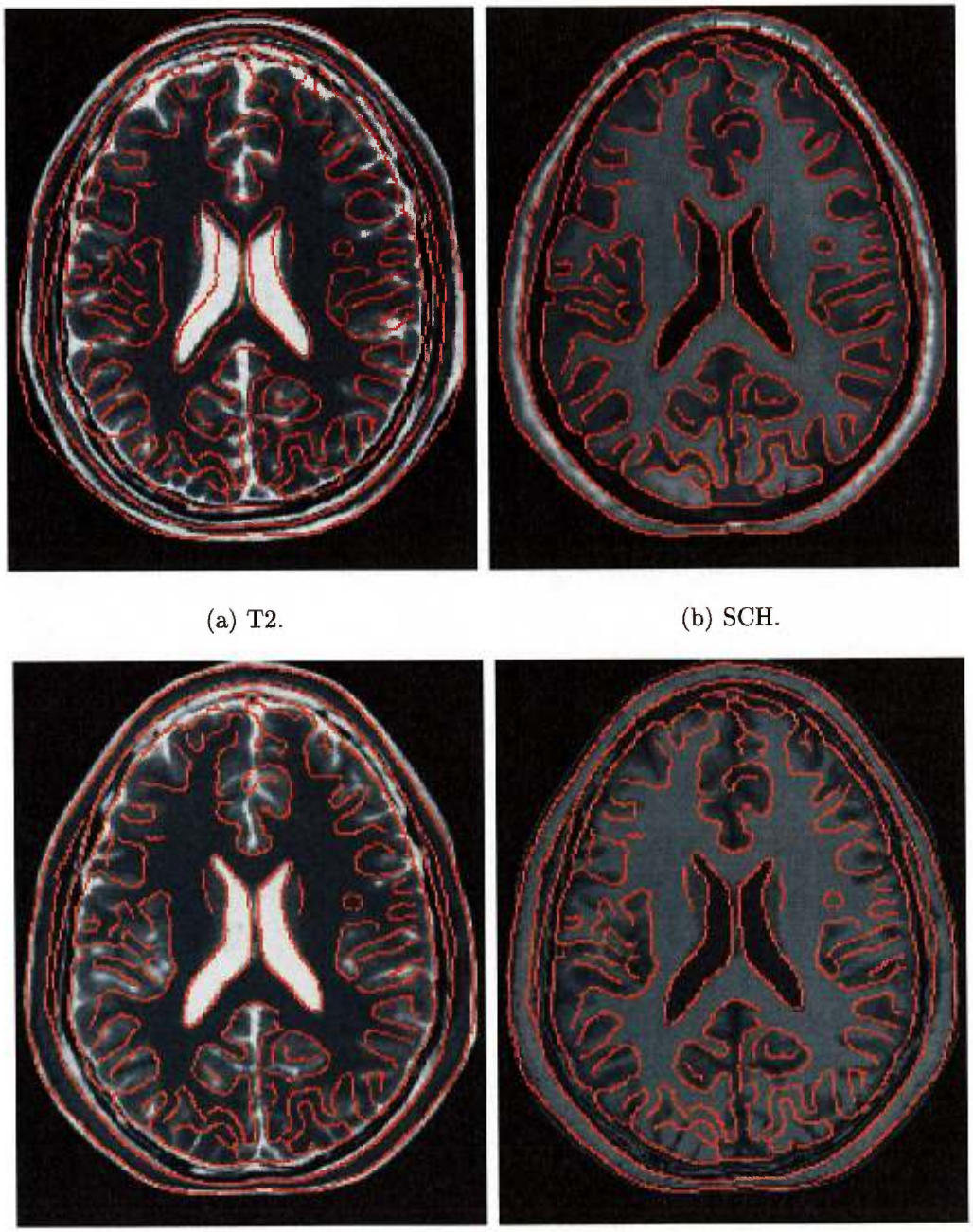

(a) T2.

(b) SCH.

(c) T2 without intensity correction after registration with SCH.

(d) T2 with intensity correction after registration with SCH.

Figure 2.14: Corresponding axial slices of T2 to SCH registration result. Contours were obtained using a Canny-Deriche edge detector on SCH (Figure 2.14(b)) and overlaid on the other images to better assess the quality of registration.

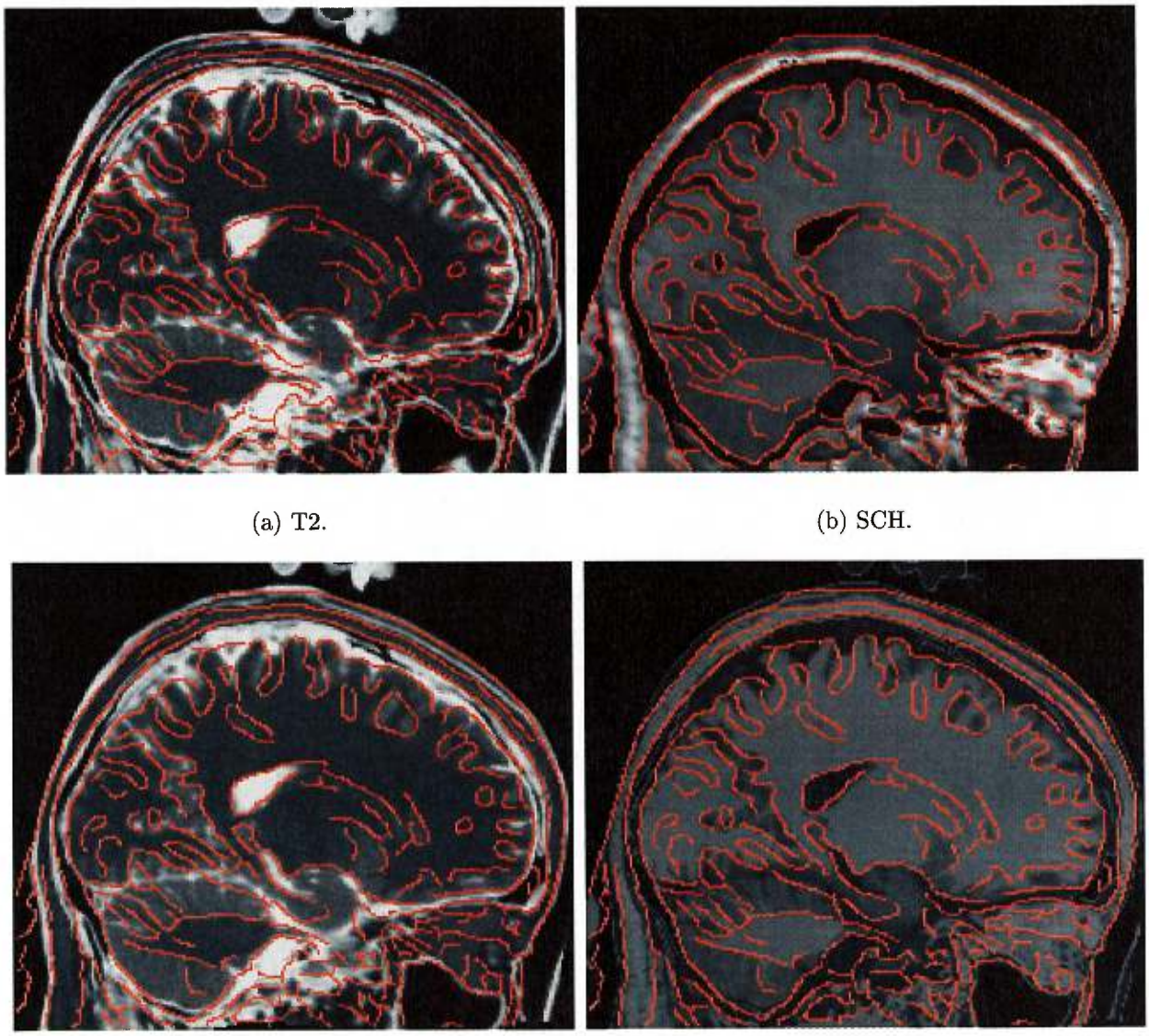

(a) T2.

(b) SCH.

(c) T2 without intensity correction after registration with SCH.

(d) T2 with intensity correction after registration with SCH.

Figure 2.15: Corresponding sagittal slices of T2 to SCH registration result. Contours were obtained using a Canny-Deriche edge detector on SCH (Figure 2.15(b)) and overlaid on the other images to better assess the quality of registration.

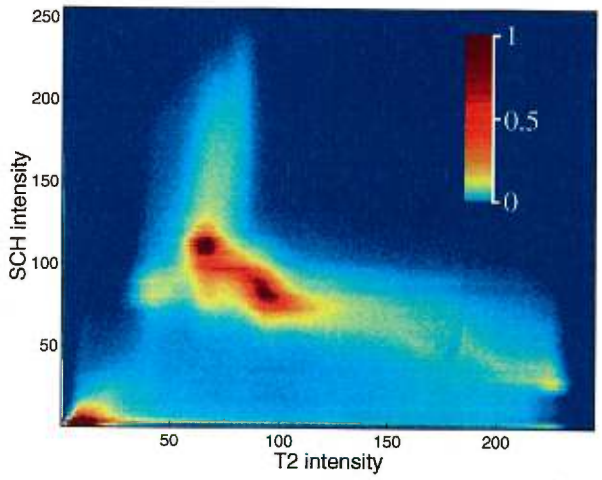

(a) The joint histogram of T2 and SCH after registration. The joint histogram values have been compressed logarithmically and normalized as is depicted in the color scale. Values range from red representing high point densities to blue depicting low point densities.

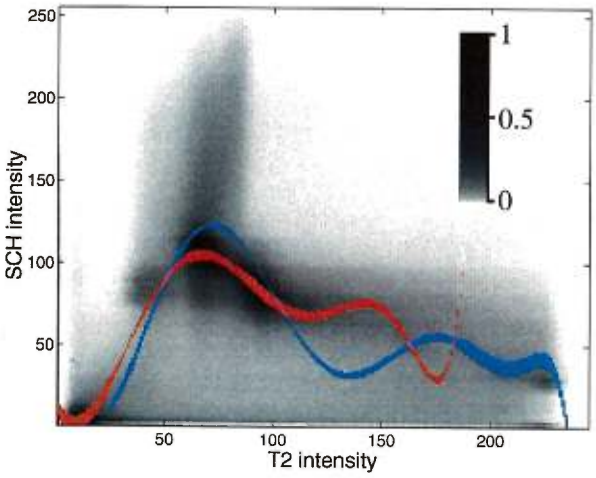

(b) The red line corresponds to f_{θ} and the blue one to f_{ψ}. The line width for a given intensity value s in T2 corresponds to the value of the corresponding $\pi_{\epsilon}(s)$. The gray values represent the joint histogram after registration.

Figure 2.16: Intensity transformation found when registering T2 with SCH and assuming bifunctional dependence.

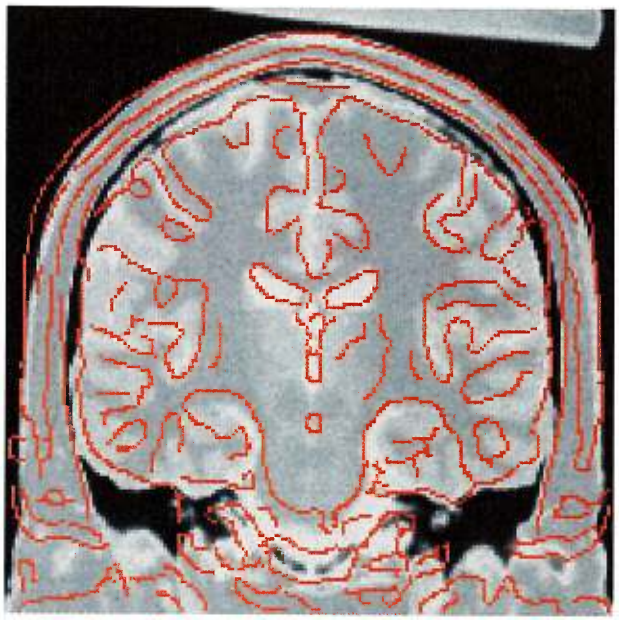

(a) PD.

(b) SCH.

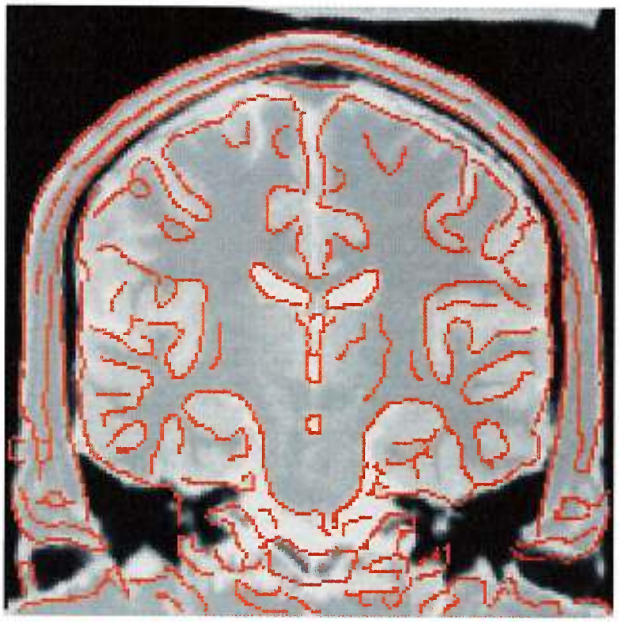

(c) PD without intensity correction after registration with SCH.

(d) PD with intensity correction after registration with SCH.

Figure 2.17: Corresponding coronal slices of PD to SCH registration result. Contours were obtained using a Canny-Deriche edge detector on SCH (Figure 2.17(b)) and overlaid on the other images to better assess the quality of registration.

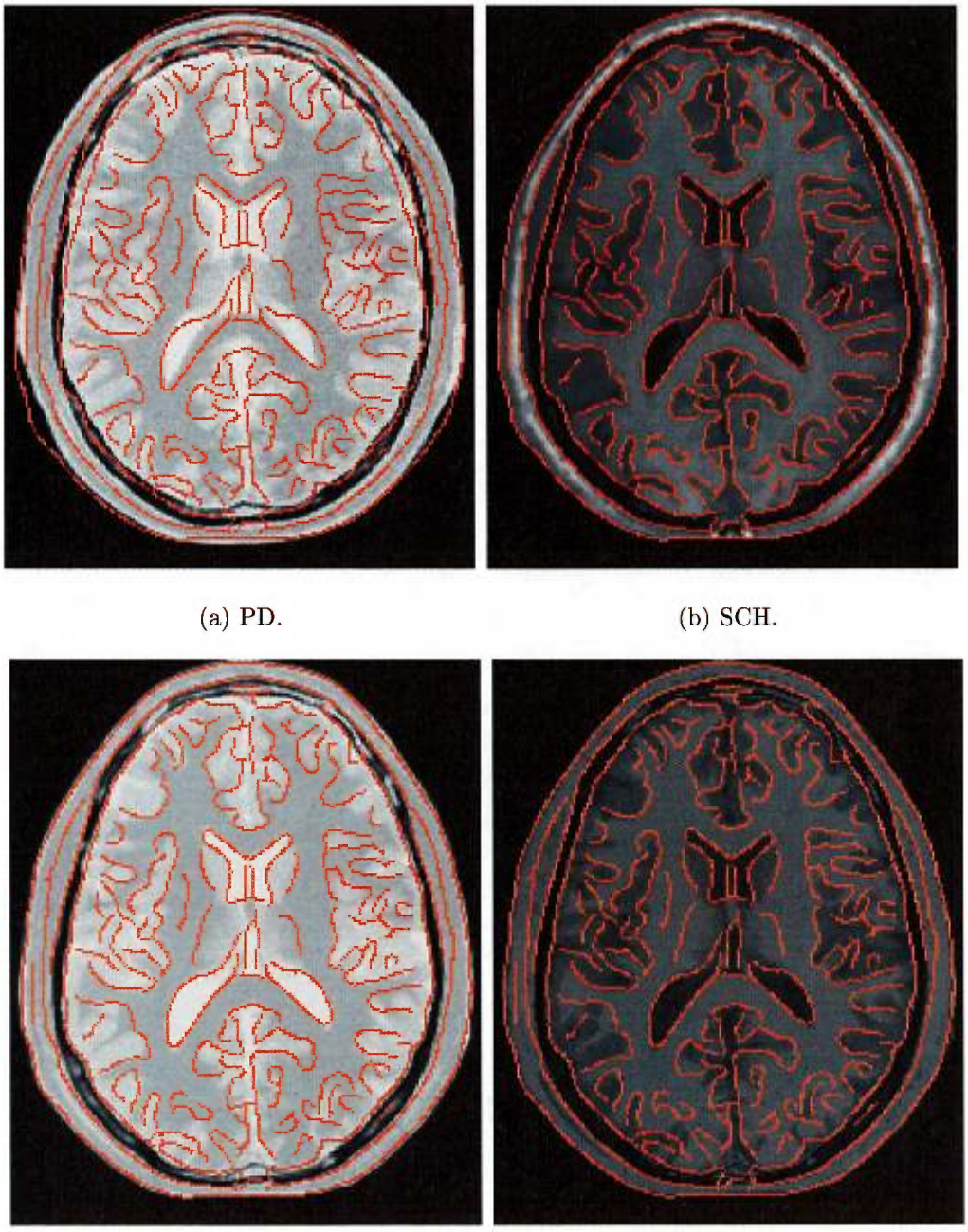

(a) PD.

(b) SCH.

(c) PD without intensity correction after registration with SCH.

(d) PD with intensity correction after registration with SCH.

Figure 2.18: Corresponding axial slices of PD to SCH registration result. Contours were obtained using a Canny-Deriche edge detector on SCH (Figure 2.18(b)) and overlaid on the other images to better assess the quality of registration.

(a) PD.

(b) SCH.

(c) PD without intensity correction after registration with SCH.

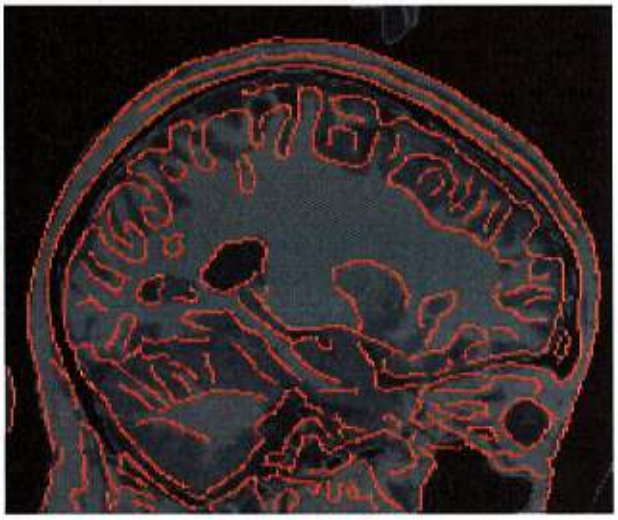

(d) PD with intensity correction after registration with SCH.

Figure 2.19: Corresponding sagittal slices of PD to SCH registration result. Contours were obtained using a Canny-Deriche edge detector on SCH (Figure 2.19(b)) and overlaid on the other images to better assess the quality of registration.

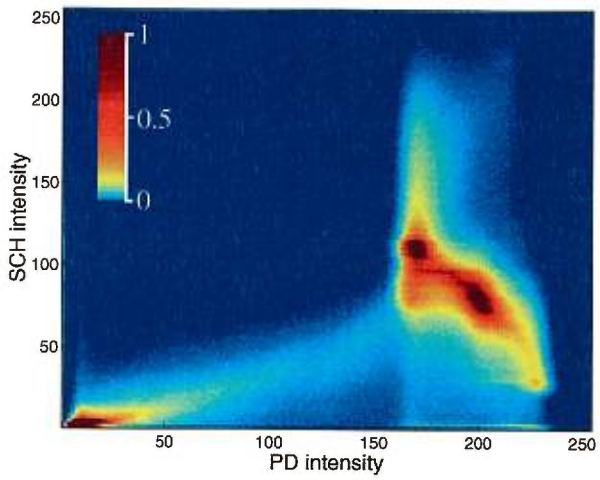

(a) The joint histogram of PD and SCH after registration. The joint histogram values have been compressed logarithmically and normalized as is depicted in the color scale. Values range from red representing high point densities to blue depicting low point densities.

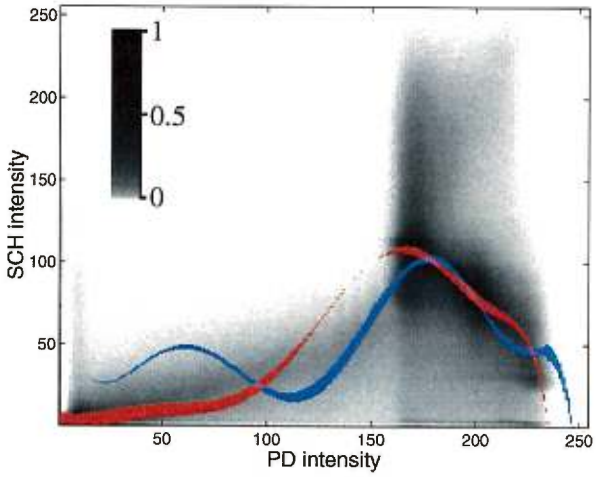

(b) The red line corresponds to f_{θ} and the blue one to f_{ψ}. The line width for a given intensity value s in PD corresponds to the value of the corresponding $\pi_{\epsilon}(s)$. The gray values represent the joint histogram after registration.

Figure 2.20: Intensity transformation found when registering PD with SCH and assuming bifunctional dependence.

i.e. there is a function that can go though the major clusters of the joint histograms. This is also reflected by the closely similar shapes of the corresponding f_{θ} and f_{ψ}.

Thus, we have registered PD with SCH using the monofunctional model and $c = 0.8$. This result is presented in Figures 2.21, 2.22 and 2.23. As can be seen by comparing the Figure 2.17(d) with Figure 2.21(d), Figure 2.18(d) with Figure 2.22(d) and Figure 2.19(d) with Figure 2.23(d), the intensity transformation does not correct as well the CSF intensities and the distinction between the different structures is less contrasted.

This may be explained by a closer look at our bifunctional intensity modeling. Equation 2.20 reflects the assumption that if an anatomical point has an intensity s in S, the corresponding point has an intensity t in T that is distributed normally around two possible values depending on s. But it makes no assumption about how the intensities in S are distributed. This models the intensities of S without noise, which may not necessarily be well justified, but enables the use of linear regression to estimate the intensity transformation.

The effect of noise in S is reflected in the joint histograms by enlarging clusters along the x axis. This, added to bad matches and partial volume effect, creates many outliers in C and makes the assessment of the true intensity transformation more difficult and more resistant to our robust regression technique. Preprocessing of S using for example anisotropic diffusion may narrow the clusters and provide better results [77].

Adding the estimation of a second function in the bifunctional model helps counter the effect of noise on S. For example, the CSF in the PD image has intensity values ranging from about 200 to 240 and gray matter from about 175 to 210. In SCH, these ranges are about 30 to 70 and 55 to 80 respectively. As can be seen in Figure 2.20, f_{θ} models well the gray matter cluster but fails to reflect the CSF transformation. This is also well depicted in Figures 2.21, 2.21 and 2.23 in which the CSF and gray matter intensity transformation is modeled using a single polynomial. In this case, the CSF is often mapped as gray matter. Estimating the second polynomial f_{ψ} solves this problem by considering the CSF cluster.

Note that for the registration of the atlas to SCH and of the T1 to the CT, we have always deformed the image with the most information, i.e. the one with the higher number of perceivable structures. This is simply because our algorithm permits many structures of the deformed image to be mapped to a single intensity, as is the case when transforming a

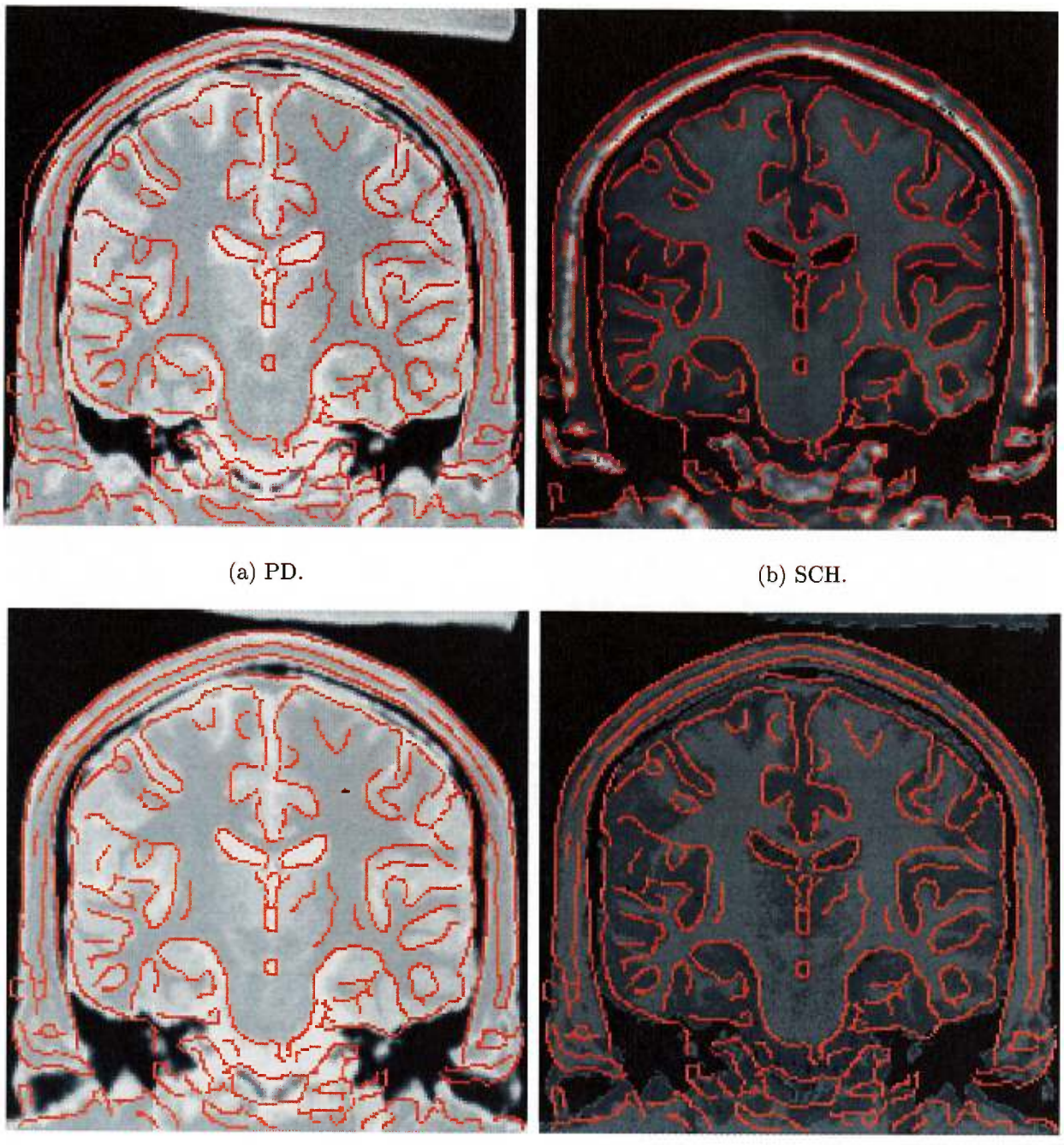

(a) PD.

(b) SCH.

(c) PD without intensity correction after registration with SCH.

(d) PD with intensity correction after registration with SCH.

Figure 2.21: Corresponding coronal slices of PD to SCH registration result using the monofunctional model. Contours were obtained using a Canny-Deriche edge detector on SCH (Figure 2.21(b)) and overlaid on the other images to better assess the quality of registration.

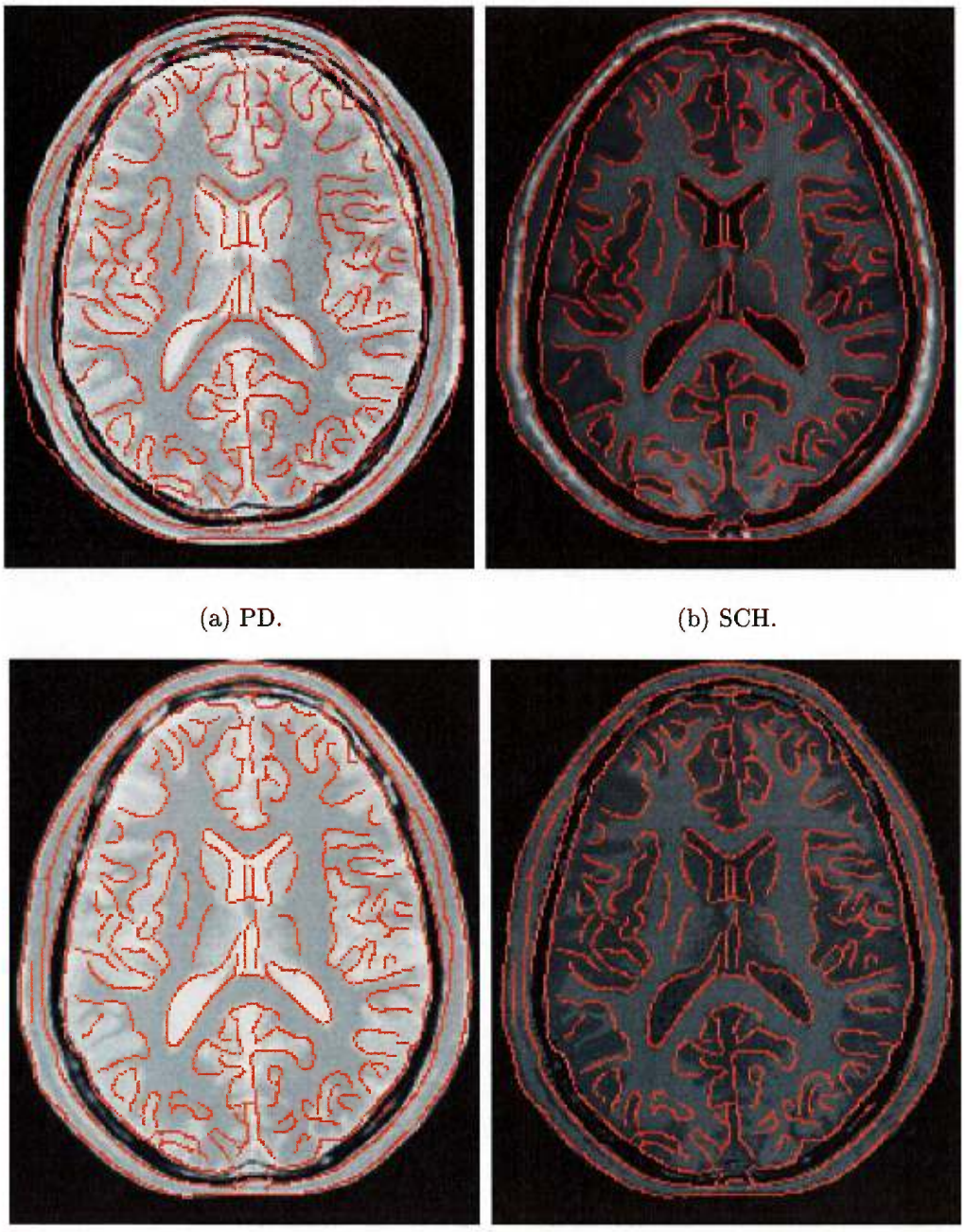

(a) PD.

(b) SCH.

(c) PD without intensity correction after registration with SCH.

(d) PD with intensity correction after registration with SCH.

Figure 2.22: Corresponding axial slices of PD to SCH registration result using the mono-functional model. Contours were obtained using a Canny-Deriche edge detector on SCH (Figure 2.21(b)) and overlaid on the other images to better assess the quality of registration.

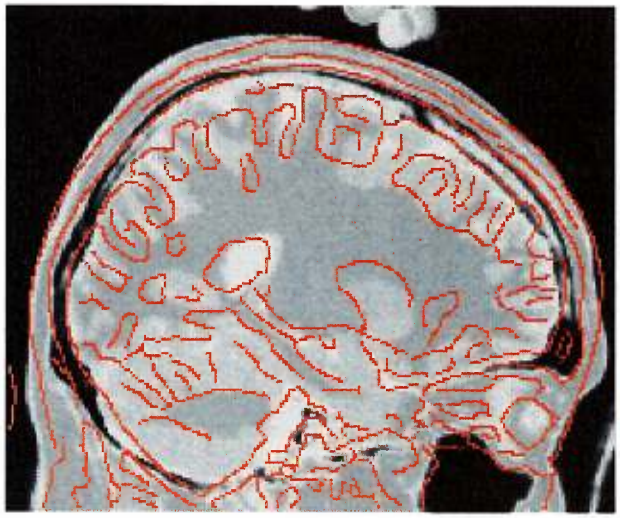

(a) PD.

(b) SCH.

(c) PD without intensity correction after registration with SCH.

(d) PD with intensity correction after registration with SCH.

Figure 2.23: Corresponding sagittal slices of PD to SCH registration result using the monofunctional model. Contours were obtained using a Canny-Deriche edge detector on SCH (Figure 2.23(b)) and overlaid on the other images to better assess the quality of registration.

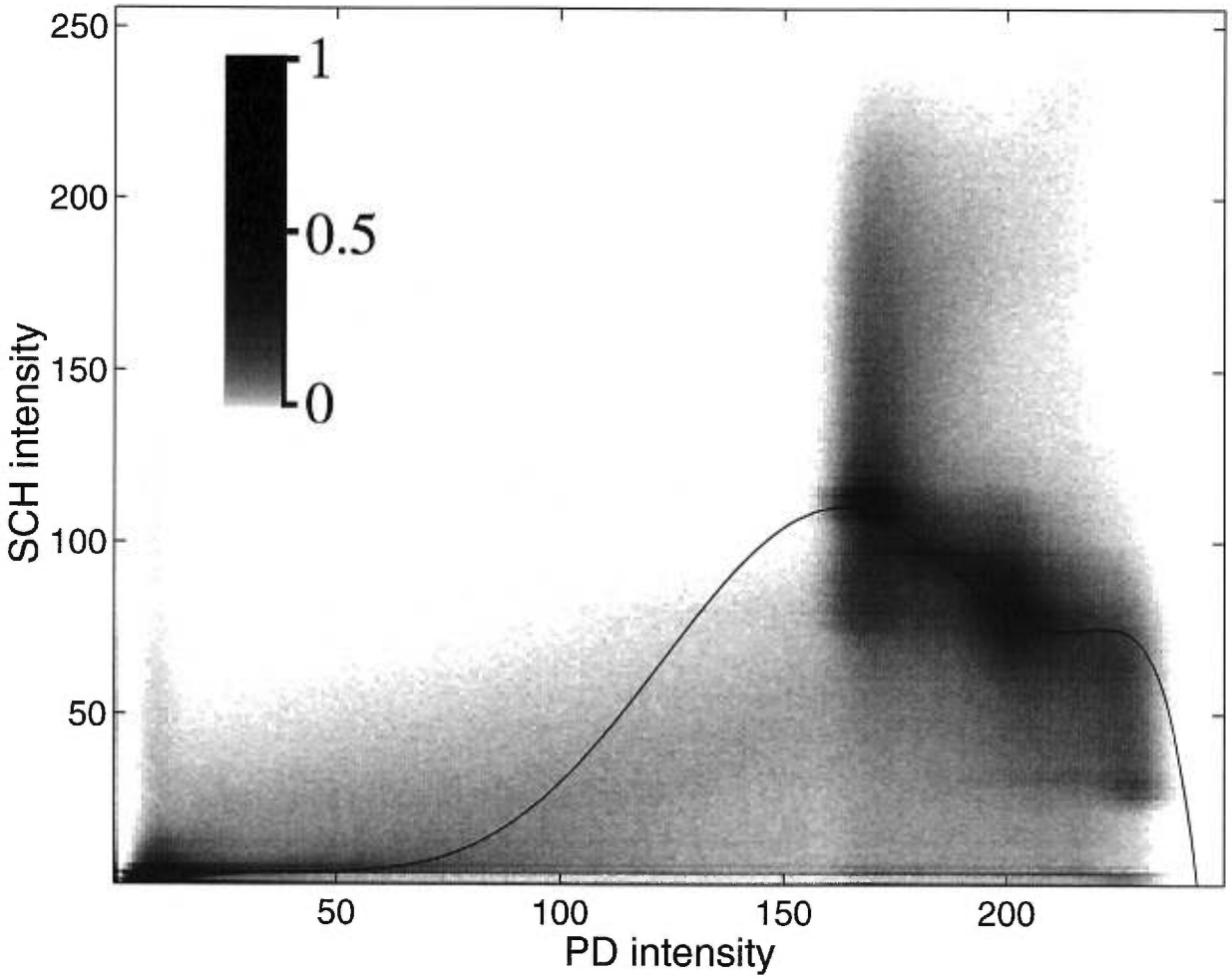

Figure 2.24: Intensity transformation found by registering PD with SCH and assuming monofunctional dependence. The function f is overlaid on the joint histogram of the two images after registration. The joint histogram values have been compressed logarithmically and normalized as is depicted in the color scale.

T1 image into a CT image (See Figures 2.9, 2.10 and 2.11.). But a single intensity in the deformed image can be mapped to at most two intensities in the target image. For example, if we used the CT image as the image to be deformed, the dominant gray intensity value in this image would have to be mapped to gray matter, white matter, CSF, etc. This would require more than two functions to be estimated and complicates the algorithm. Hence, it is always better to use the image with the most number of structures visible as the source image.

2.4.3 Mutual Information

We present in Figures 2.25, 2.26 and 2.27 the result of registering the T1 image with the CT image using the MI method described in Section 2.2.4. A typical difference between using our bifunctional method instead of our MI implementation can be appreciated by comparing Figure 2.9(c) with Figure 2.25(c), Figure 2.9(c) with Figure 2.25(c) and Figure 2.9(c) with Figure 2.25(c). As can be seen, the contours of corresponding structures do not match after registration using MI. The head contours seem to be attracted by the image borders, which means that the driving forces have misleading directions in this region. This outcome might be due to the fact that Parzen windowing provides too little information on how to match the intensities of the images. As a consequence, the direction of the MI gradient, from which the local driving force are derived, might be unreliable. Many registrations were performed using the MI criterion with varying values for α and several Parzen window sizes. The results we obtained using this strategy were much less convincing than the ones we obtained using our bifunctional method; the source image deformed very little unless the α parameter was set to a high value, in which case the displacements looked random.

The poor results obtained with our implementation of MI might sound surprising as MI performs generally very well in rigid/affine registration. Although it would be irrelevant to conclude that MI is not well-suited for elastic registration, a partial explanation may be given. What basically does MI is to model the dependence between the images by estimating their intensity joint distribution among the set of every possible distributions [77]. This set has a dimension $k_s \times k_t - 1$, where k_s and k_t are the numbers of intensity levels respectively in

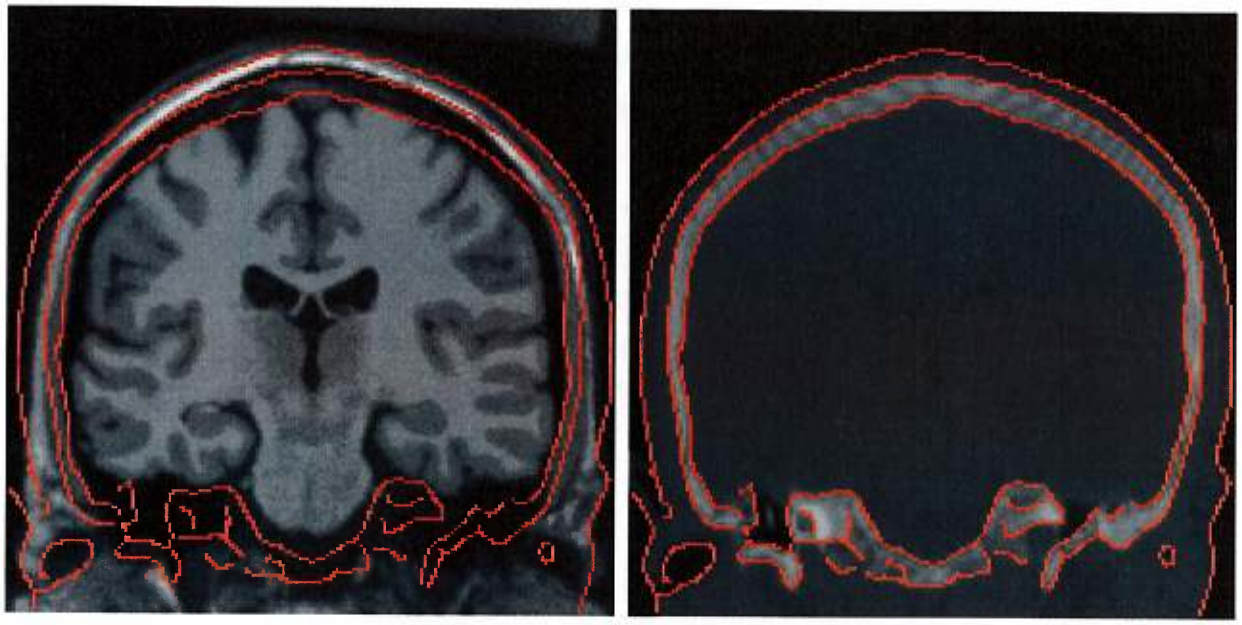

(a) T1.

(b) CT.

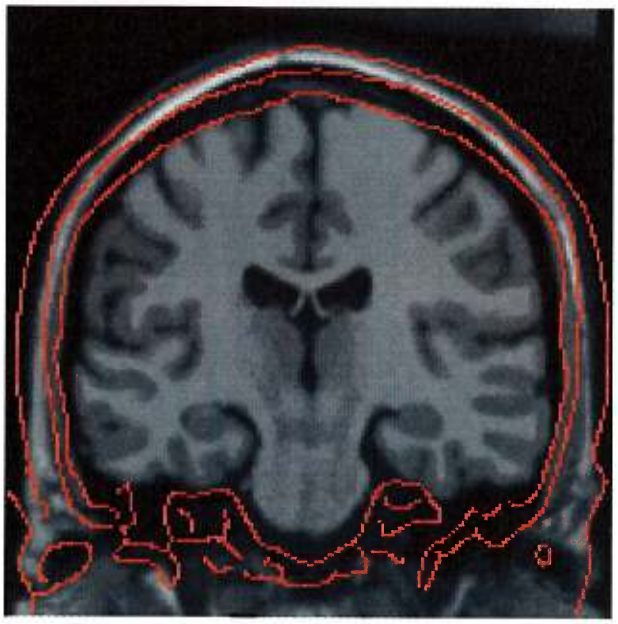

(c) T1 after registration with CT.

Figure 2.25: Corresponding coronal, sagittal and axial slices T1 to CT registration result using MI. Contours were obtained using a Canny-Deriche edge detector on CT (Figure 2.25(b)) and overlaid on the other images to better assess the quality of registration.

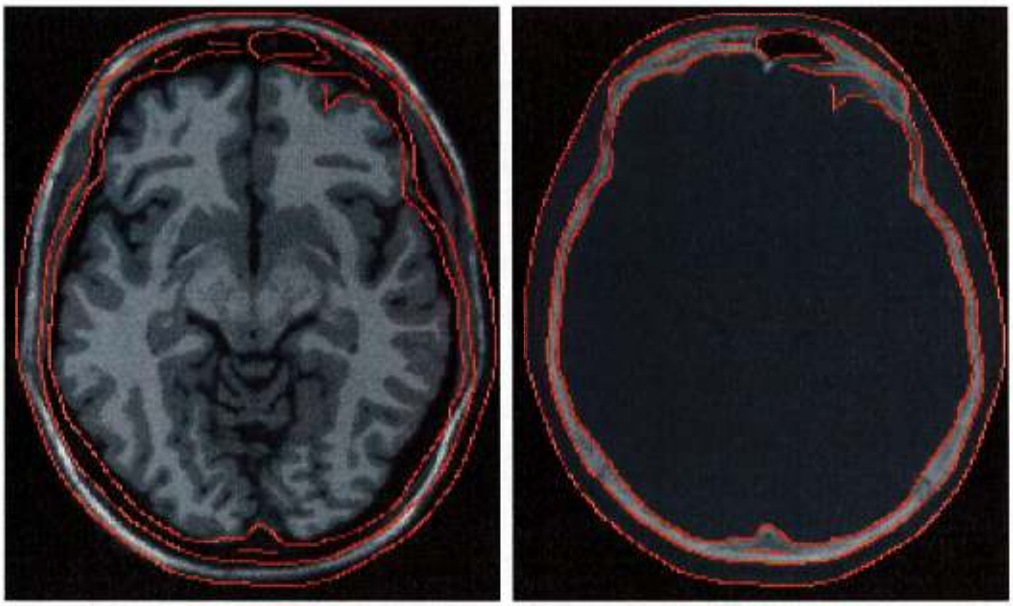

(a) T1. (b) CT.

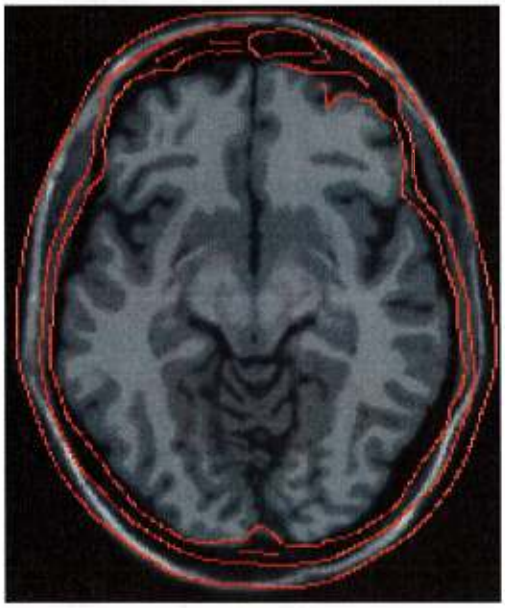

(c) T1 after registration with CT.

Figure 2.26: Corresponding coronal, sagittal and axial slices T1 to CT registration result using MI. Contours were obtained using a Canny-Deriche edge detector on CT (Figure 2.26(b)) and overlaid on the other images to better assess the quality of registration.

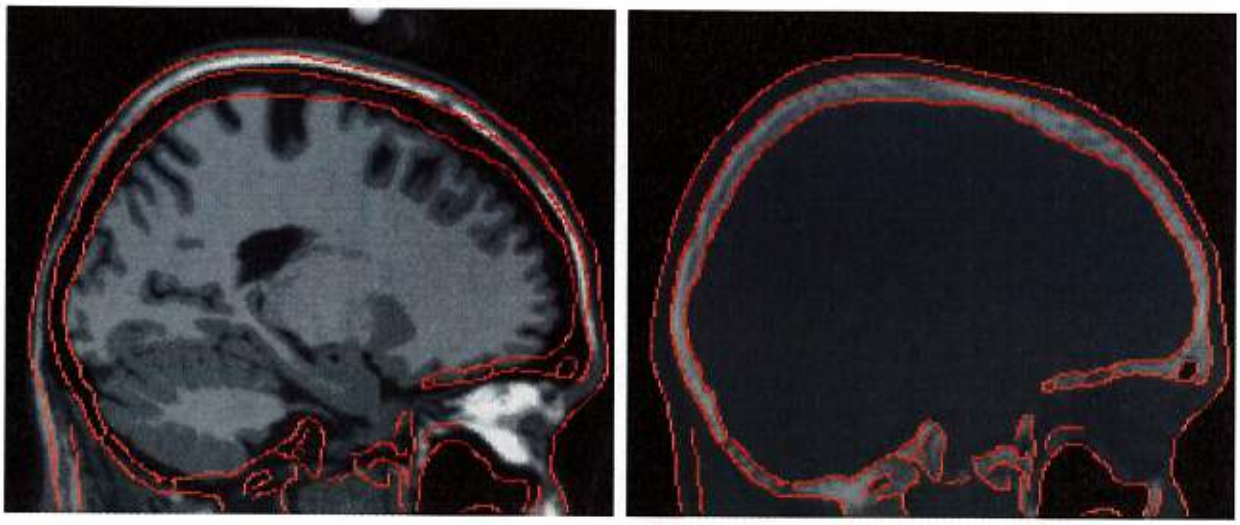

(a) T1.

(b) CT.

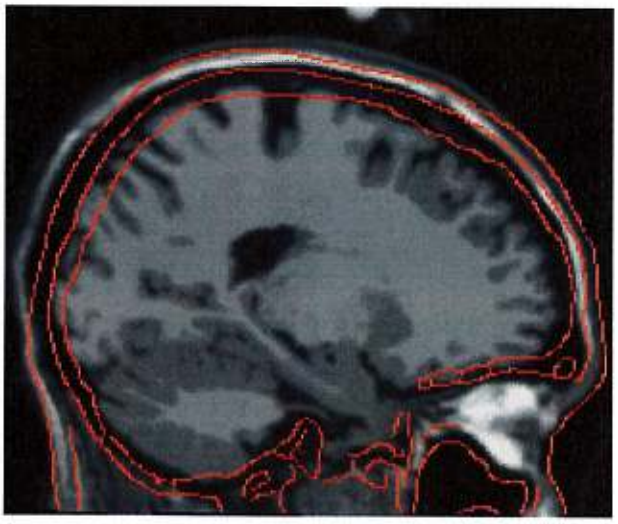

(c) T1 after registration with CT.

Figure 2.27: Corresponding coronal, sagittal and axial slices T1 to CT registration result using MI. Contours were obtained using a Canny-Deriche edge detector on CT (Figure 2.27(b)) and overlaid on the other images to better assess the quality of registration.

the source and target images. In the context of rigid/affine registration, where no more than 12 geometrical parameters need to be estimated, such an enormous search space is usually affordable. However, with elastic registration, the geometrical transformation is granted many degrees of freedom and maximizing MI might then become an under-constrained problem.

Our method distinguishes itself from MI by imposing strong constraints on the intensity space. In the case where monofunctional dependence is assumed, only $p + 1$ parameters are estimated to model the intensity dependence, p being the polynomial degree. When assuming a bifunctional relationship, this number becomes $2(p + 1) + 1 + 2k_s$. To give a numerical comparison in the typical case of one-byte encoded images ($k_s = k_t = 256$), and with a polynomial degree $p = 25$ (an upper bound), our method estimates 26 parameters in the monofunctional version and 565 parameters in the bifunctional version, whereas MI requires 65535 parameters to be estimated.

2.4.4 Displacement Field Comparison

Since the atlas, the T1, the T2 and the PD images have all been registered with SCH, it is relevant to compare some statistics of the resulting displacement fields to assess if our algorithm provides consistent results across modalities.

We computed statistics regarding the difference between any two of these displacement fields. The length of the vectors of the resulting difference fields were calculated. Each cell of Table 2.2 presents, for each combination of displacement fields, the median length, the average length with the corresponding standard deviation and the maximum length of the difference field.

The two largest average differences are 1.76mm and 1.58mm and were found when registering the atlas with T1 and PD respectively. This may be explained by the intensity correction bias for the CSF that would tend to attenuate displacements and produce larger errors, a problem invoked in Section 2.4.1. Aside from these, the average error length varies between 0.97mm and 1.40mm and the median error is between 0.85mm and 1.32mm. These are values in the range of the image resolution of 1.0mm. Note also that all the standard deviations are below this value.

We point out that these are global measures that are presented to provide an idea of the differences between the displacement fields. They do not strictly provide a validation of the method, but do show a certain coherence between the different results we obtained.

2.5 Conclusion

In this paper, we introduced an original method to perform non-rigid registration of multi-modal images. This iterative algorithm is composed of two steps: the geometrical transformation and the intensity transformation. We have related the geometrical transformation model to several popular registration concepts: SSD, optical flow and the demons method. Two intensity transformation models were described which assume either monofunctional or bifunctional dependence between the images to match. Both of these models are built using robust estimators to enable precise and accurate transformation solutions. Results of registration were presented and showed that the algorithm performs very well for several kinds of modalities including T1 MR, T2 MR, PD MR, CT and segmentations, and provides consistent results across modalities. Our algorithm was compared with the maximization of the MI criterion and seems to be more apt at evaluating high-dimensional deformations, as it puts more constraints on the parameters to be estimated and thus permits a better search of the parameter space.

		Atlas-SCH	Atlas-SCH'	T1-SCH	T2-SCH	PD-SCH
Atlas-SCH	median		0.85	1.46	1.13	1.67
	average		0.97	1.58	1.23	1.76
	std. dev.		0.60	0.84	0.63	0.79
	maximum		4.57	6.99	5.14	7.10
Atlas-SCH'	median	0.85		0.89	0.95	1.15
	average	0.97		1.00	1.07	1.25
	std. dev.	0.60		0.55	0.60	0.64
	maximum	4.57		4.48	5.46	7.43
T1-SCH	median	1.46	0.89		1.00	1.01
	average	1.58	1.00		1.18	1.16
	std. dev.	0.84	0.55		0.78	0.71
	maximum	6.99	4.48		7.17	8.08
T2-SCH	median	1.13	0.95	1.00		1.32
	average	1.23	1.07	1.18		1.40
	std. dev.	0.63	0.60	0.78		0.68
	maximum	5.14	5.46	7.17		6.86
PD-SCH	median	1.67	1.15	1.01	1.32	
	average	1.76	1.25	1.16	1.40	
	std. dev.	0.79	0.64	0.71	0.68	
	maximum	7.10	7.43	8.08	6.86	

Table 2.2: Statistics regarding the displacements differences between each type of registration. Each cell presents the median length, the average length with the corresponding standard deviation and the maximum length. All measures are in millimeters.

Chapitre 3

Étude de régions anatomiques correspondantes

Sommaire

Avant-propos

La médecine est aujourd'hui à la recherche d'information quantitative sur le cerveau humain, mais le problème ne réside pas tant dans l'accès à cette information mais plutôt dans son analyse. Il existe en effet une quantité importante d'information provenant des différentes techniques imageries et d'autres tests médicaux, mais cette information est si abondante que l'analyser est ardu et de longue durée.

Dans ce prochain chapitre, une méthode est présentée permettant de parcourir rapidement un ensemble d'images non recalées et provenant de sujets différents afin d'y extraire la même région anatomique [45]. Cette méthode, locale et rapide, permet l'analyse de la même structure cérébrale d'un ensemble de sujets dans des délais applicables en milieu clinique. Elle a l'avantage de se restreindre à l'analyse de volumes locaux, ou volumes d'intérêts, ce qui permet de fournir un résultat indépendant des structures anatomiques éloignées de celle étudiée. Nous présentons des exemples d'application comme la construction de modèles moyens d'une région anatomique, une idée développée dans le chapitre 4, ainsi que des résultats préliminaires de classification selon la morphologie de la structure d'intérêt.

Beaucoup de travaux ont été réalisés sur la recherche d'objets dans des banques de données d'images, mais ces travaux sont généralement axés vers la reconnaissance d'objets tridimensionnels similaires dans des images bidimensionnelles. Leurs propriétés dominantes sont souvent leur invariance par rapport à différents types de transformations, la présence d'ombres, etc. Elles ont également souvent pour but de fournir le sous-ensemble d'images qui présentent un objet recherché. Ces propriétés sont ici peu enviables car les objets de notre banque de données sont complets et n'ont subi aucune perte d'information. De plus, nous ne cherchons pas la présence ou non d'un objet dans un ensemble d'images mais bien la position précise d'un objet, ou plutôt d'une structure anatomique, que nous savons présente dans toutes les images. Des mesures rapides telles que présentées dans nos travaux nous semblent suffisantes et ont apporté des résultats fort satisfaisants. Une étude plus importante de classification à laquelle nous avons collaboré et utilisant cette méthode d'extraction de régions d'intérêts peut être trouvée dans les travaux de WEBB *et al.* [103].

L'article qui suit est une version modifiée d'un article publié selon la référence bibliogra-

phique suivante :

A. GUIMOND, G. SUBSOL, et J.-P. THIRION. « Automatic MRI Database Exploration and Applications ». *International Journal of Pattern Recognition and Artificial Intelligence*, 11(8):1345–1365, décembre 1997.

Automatic MRI Database Exploration and Applications

Abstract

The design of representative models of the human body is of great interest to medical doctors. Qualitative information about the characteristics of the brain is widely available, but due to the volume of information that needs to be analyzed and the complexity of its structure, rarely is there quantification according to a standard model. To address this problem, we propose in this paper an automatic method to retrieve corresponding structures from a database of medical images. This procedure being local and fast, will permit navigation through large databases in a practical amount of time. We present as examples of applications the building of an average volume of interest and preliminary results of classification according to morphology.

keywords—image database, exploration, volume of interest (VOI), average patient, medical atlas, classification, registration, magnetic resonance imaging (MRI).

Introduction

Neurological disorders like epilepsy, multiple sclerosis, schizophrenia or Alzheimer's disease have for long been the subject of serious studies. It is believed that such conditions could be coupled with abnormal configurations of different brain structures [103, 53, 46]. Although anatomical brain atlases [88, 81, 10] provide information to analyze and compare brain structures, their characteristics, such as precise shape and variance among healthy subjects, are not yet clearly defined. Moreover, paper representations are not sufficient to answer today's problems in this field [68, 83]; such atlases are two dimensional, static and based on one or few studies. Computer guided diagnosis, multi-media medical teaching or surgical simulation robotics require more adaptable and complete sources of information.

Over recent years, the use of magnetic resonance imaging (MRI) has produced huge medical brain image databases. Study of these data could provide the information needed to build numerical atlases with quantification of brain structure characteristics. This article addresses the problem of exploring such databases to retrieve information about a specific part of the brain (see Figure 3.1). The idea is to provide tools for practitioners to define a

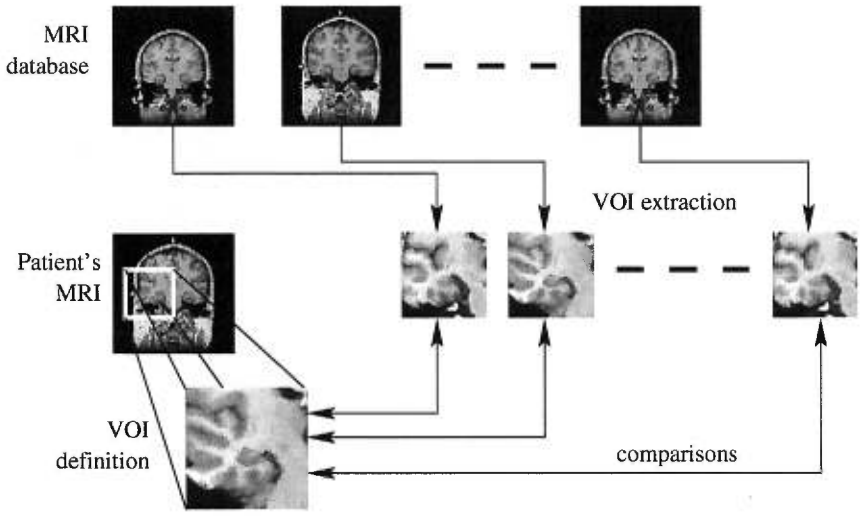

Figure 3.1: Volume of interest extraction and comparison are the principal ideas behind medical image database exploration.

volume of interest (VOI) within a patient's MRI and extract corresponding VOIs from the database. These VOIs can be viewed as either control subjects or representative elements of different classes of pathology. In the first case, contrast images would facilitate the identification of significant abnormalities in the patient's VOI. In the second, comparisons would reveal which pathologies the patient is most related to, with associated probabilities. For example, to study temporal lobe epilepsy, we could use a database composed of representatives of a normal subject, of an epileptic with an atrophied left hippocampus and of an epileptic with an atrophied right hippocampus. Following the extraction of the hippocampus and comparisons, a diagnostic would be automatically produced putting forward affinities between the patient and the database elements.

The heart of such an extraction procedure is a matching method that finds correspondences between the patient's brain and the database elements. Once the VOIs extracted, we can apply different kinds of processing: automatic measure of features, shape extraction and comparison, factor analysis, statistical ordering, etc. Thus, we present a new method to evaluate differences between VOIs and obtain quantitative information from the database.

The first part of this paper reports different techniques used to compare brains. The second part deals with brain structure differences between individuals and the type of infor-

mation they convey. We present our method in a third section, and explain how to identify important differences between images depending on the kind of information that we seek. The fourth part is an overview of possible applications including the construction of an average patient and some preliminary results of classification according to morphology. We conclude the paper with a brief discussion of future work.

3.1 Matching Methods

Matching a model image I_m with a scene image I_s, using a transformation class T and a similarity measure S, can be formalized as the process of finding the function $M = \arg_{t \in T} \min S(t(I_m), I_s)$. The application of this function to the model image $M(I_m)$ will be called a *mapping*, or equivalently a *warping*, of I_m onto I_s.

3.1.1 Previous Work

Many matching methods have been put forward to identify differences between brain images (see [99] for a comprehensive review). They can be divided in two main categories: feature based [85, 47, 28, 87] and intensity based [89, 22, 37, 13], the trade-off being between the size of data to register and the complexity of the registration procedure.

The class of transformation T used is also of importance. Various approaches exist. To name a few, registration methods have been developed using linear [21, 2, 66], piecewise linear [61], quadratic [39] and free-form [89, 22] classes (see Figure 3.2 for a rough classification).

A very common approach in brain mapping is to use the Talairach reference space, also known as the three-dimensional proportional grid system [88]. This system uses the bicommissural line and some other anatomical landmarks to partition the brain into twelve subspaces and is an attempt to model non-linear differences between data sets (see Figure 3.3).

We can generalize the idea of Talairach by finding more landmarks, which leads to additional subdivisions of the brain volume and make the transformations more local. The

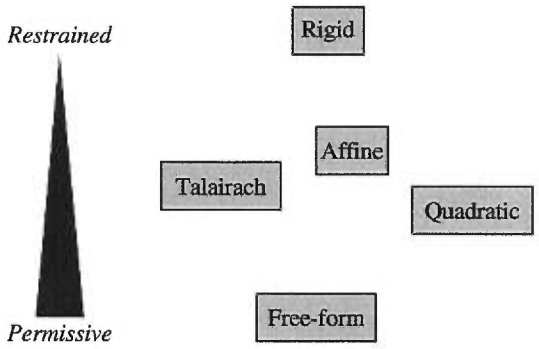

Figure 3.2: Classification of different transformation classes.

difficulty lies in the automatic detection of the landmarks. A promising solution relying on differential geometry criteria can be found in [25].

3.1.2 Our Matching Method

The matching method we developed differs from previous work by confining itself to a VOI. This has several advantages. It corresponds to doctors' need of studying particular brain structures. It also reflects the assumption that gross anatomical shape is only influenced by neighboring bodies. Finally, the database investigation must be fast. Using sub-images will help us achieve this end.

We propose a new method to quantify differences between two subjects in a localized volume of the brain using a three step approach that progressively refines the matching:

1. A global matching between the two entire data sets.

2. A regional matching between corresponding VOIs.

3. A local matching in a voxel's neighborhood.

The matching procedure we use is based on an analogy with Maxwell's demons. Briefly, given two images and a transformation class T, this algorithm delivers a mapping function M to warp a model image I_m onto a scene image I_s. It relies on polarity (inside/outside) information: the boundaries of the object in I_s are considered to be semi-permeable membranes, separating the inside of the object from the outside, and the voxels of the model

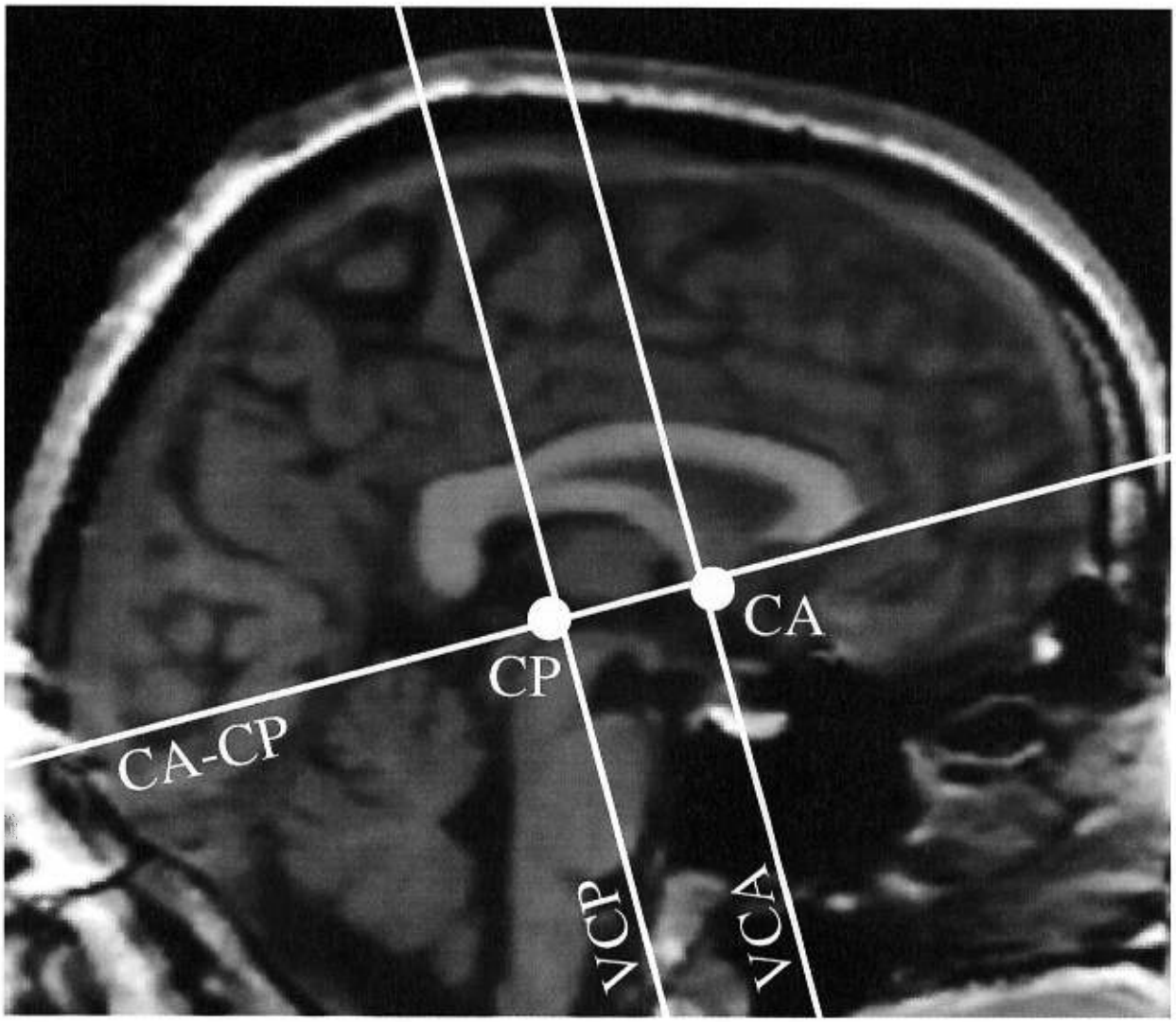

Figure 3.3: Sagittal view of the Talairach divisions. The AC-PC line touches the superior aspect of the AC (anterior commissure) and the inferior aspect of the PC (posterior commissure). The VAC line is perpendicular to the AC-PC line, touching the posterior edge of the AC.

images are considered to be particles, labeled "inside" or "outside" points. The scene object interfaces let the "inside" voxels of the model go inside, and the "outside" voxels go outside, but not the other way around. In other words, the model is "diffusing" into the scene image. The algorithm is iterative, trying to separate inside from outside while maintaining the shape of the model object by way of smoothness constraints on the displacement field estimated between I_m and I_s. For our purposes, the polarity information corresponds directly to the value of the MR image intensities, compared with iso-value constants, hence the interfaces, or "membranes" are iso-intensity surfaces. In order to be less sensitive to the intensity values, a global bias and gain between the intensities of the two images can also be estimated by the algorithm. This gives us results qualitatively similar to [3, 17] but with an implementation one or two orders of magnitude faster. More details can be found in [89, 91].

3.2 Brain Structure Variations

3.2.1 Types

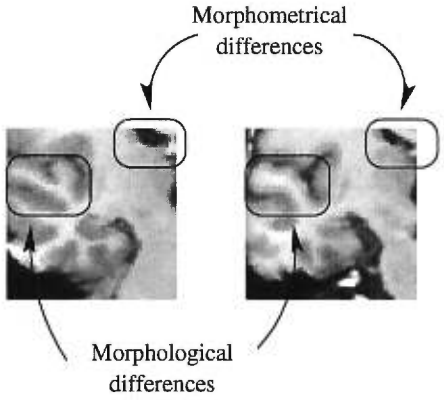

Figure 3.4: Morphometrical and morphological differences.

Variations between corresponding structures of different subjects can be separated in two categories:

Morphological These are differences due to the *presence* or the *absence* of a certain feature. For example, Figure 3.4 shows two different patients with morphological variations.

The subject on the left has two gyri and the one on the right only one. These are non-trivial differences since they require to deduce the location of absent features.

Morphometrical These are variations due to the different properties of *existing* features. For example, the length of a gyrus or the volume of the ventricles (Figure 3.4 presents two patients with different ventricle volumes). For the purpose of this article, morphometrical variations will be divided in three categories:

Global Brain scale morphometrical variations.

Regional VOI scale morphometrical variations.

Local Voxel scale morphometrical variations.

3.2.2 Irrelevant Variations

As previously mentioned, our interest lies in the study of particular brain structures. In that respect, it is generally agreed that for the vast majority of subjects, global morphometrical differences, such as whole brain width or length, are not really significant. Furthermore, this idea can hold for differences between sufficiently large VOIs. Our registration method will reflect those assumptions by correcting for affine differences at global and regional scales. This class of transformation will correct translation, rotation, scale and skew differences between VOIs.

Choosing this transformation class has some advantages over the Talairach alternative. The proportional grid system is a reference space that is frequently used by medical doctors, which is an important asset since they are the end-users. But it shows poor accuracy when matching structures away from the anterior and posterior commissures and limits the extraction procedure to the brain.

It is worth noting that correcting for affine differences between VOIs is in agreement with the Talairach philosophy of not considering structures away from the ones of concern. Since they are both based on linear transformations, their differences can be estimated by looking at the number of free parameters they hold. A Talairach conversion is defined by 1 3D point, 1 distance (from AC to PC), 1 rotation around each axis and 6 scaling factors for a total of

13 unknowns. An affine transformation accounts for 12 parameters: 1 3D translation and for each axis, 1 rotation, 1 skew and 1 scaling. So there is only 1 degree of freedom difference between them.

3.3 Extraction of VOIs

3.3.1 Method

As mentioned earlier, our method is divided in three steps: (1) global, (2) regional and (3) local matching to evaluate global, regional and local morphometrical differences respectively. These steps are detailed below and displayed in Figure 3.5.

Global morphometrical corrections The global correction procedure consists in *estimating* an affine transformation to map the database entry's dimensions to the ones of the reference image. This step is necessary to extract grossly corresponding VOIs needed for regional comparisons in the second step. To reduce computation, the matching is done on sub-sampled images, a justifiable approach since we are only looking for a gross correspondence.

Before registration, we apply to each of the two images the following transformations:

1. A transformation A to a standard axis view and voxel size. In our case these are coronal views and $1 \times 1 \times 1$ mm^3 per voxel. This transformation assures images coming from different sources are comparable. This matrix is constructed from information contained in the image header.
2. A resampling using the scale parameter S_g to the desired resolution for global registration. In practice, this is a useful parameter that influences the precision of the transformation obtained and the computation time.

After matching, we obtain the global affine transformation G.

Regional morphometrical corrections This procedure is similar to the previous one. Two steps differ. The first modification concerns the database entry for which we

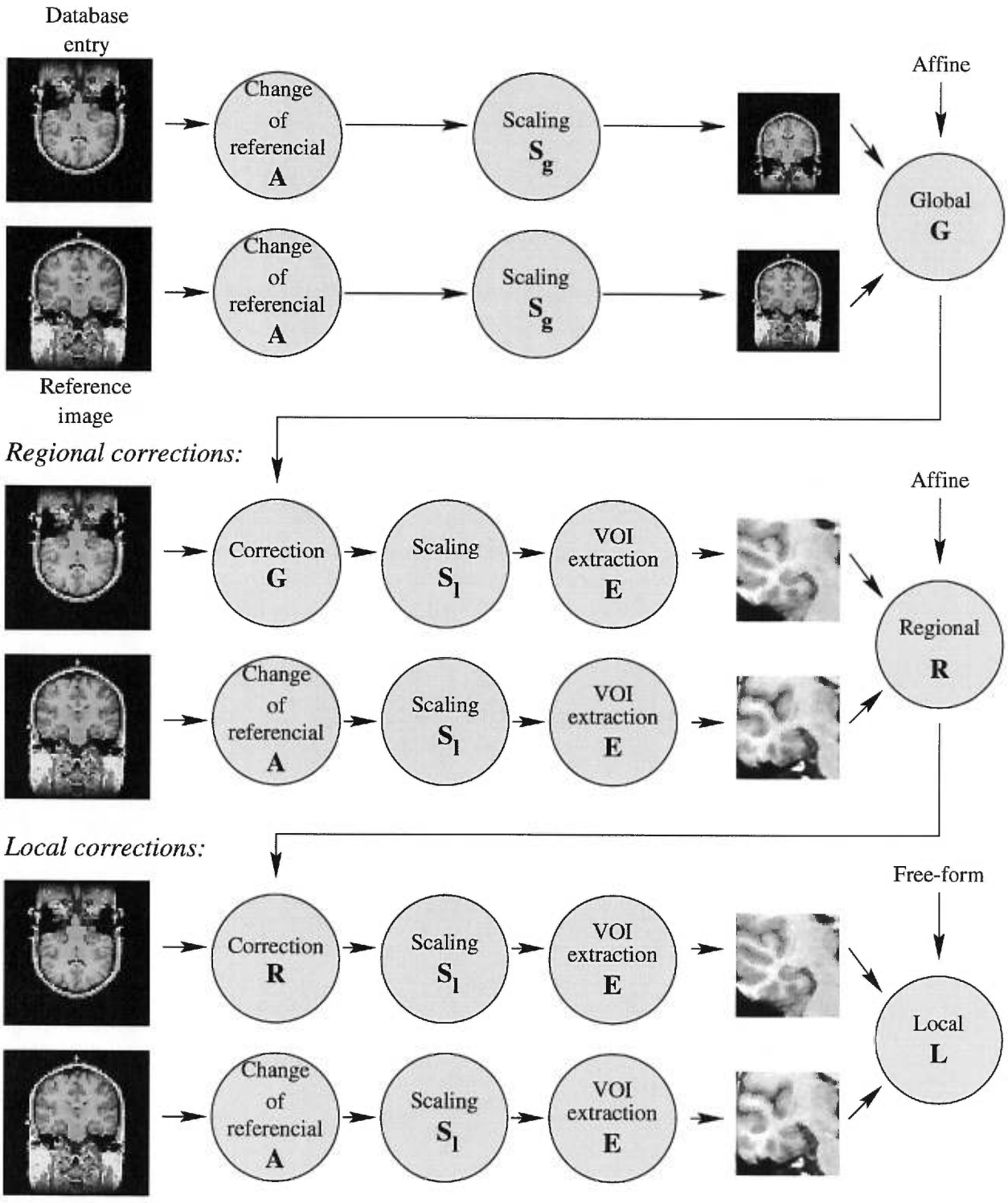

Figure 3.5: VOI extraction method using the reference image and a database entry.

substitute the change of referential by the global correction matrix G. As a second difference, the scaling factor for global registration S_g is replaced by its local equivalent S_l and a transformation E accounting for the VOI extraction. This last transformation is a cropping at identical locations for both images. In our work, it is implemented using a translation, to make it representable using matrices, and a size specification. This matching provides the regional affine transformation R.

Local morphometrical corrections Evaluation of local differences is done using the same procedure as before, with a correction matrix R updated with regional information, and a matching allowing a transformation class T of the free-form type.

Images after the regional correction are called *corresponding volumes of interest.* They differ only by morphological and local morphometrical variations. Hence, when considering structures of the same morphology, those images can be used to obtain information concerning morphometrical dissimilarities such as size differences.

Morphological variations can be obtained by applying the third step that corrects for local morphometrical differences. From this, the detection of particular features could be obtained.

An interesting aspect of our work is the combination of those transformations by way of 4×4 matrices in homogeneous coordinates, and optionally a displacement field derived from local variations, to end up with a single transformation and therefore a single resampling of the raw images.

It is also possible to completely eliminate the first part of the procedure since, for a given reference image, these transformations do not depend on the VOI definition. They can be precomputed to save time. Moreover, when the reference image changes, instead of recomputing the whole set of global transformations, it is sufficient to combine them with the transformation that brings the old reference image onto the new one (see Figure 3.6).

3.3.2 Data Sets

The following results were obtained using a database of 10 MR images of healthy subjects provided by Dr. Ron Kikinis of Brigham and Women's Hospital (see Figure 3.7). Each

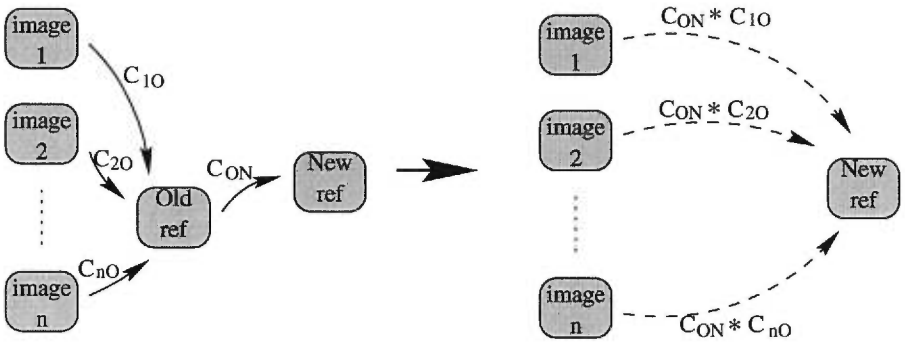

Figure 3.6: Matrix combination to change the reference image.

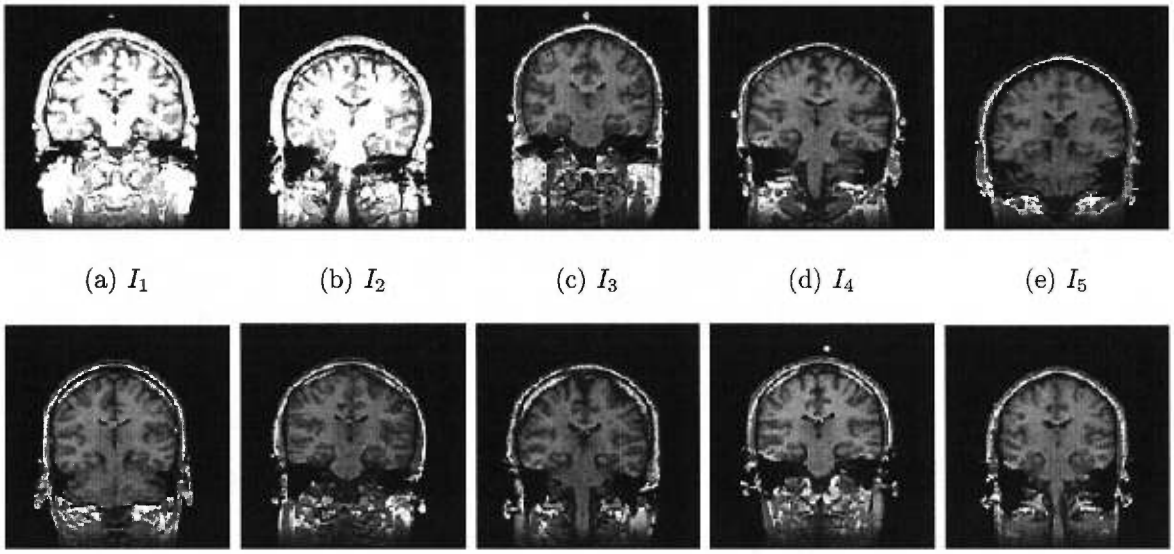

(a) I_1 (b) I_2 (c) I_3 (d) I_4 (e) I_5

(f) I_6 (g) I_7 (h) I_8 (i) I_9 (j) I_{10}

Figure 3.7: Coronal slice of each image composing the database. Images are numbered from 1 to 10 when counting from left to right, top to bottom. Note that the intensities of the first two images of the first row are much brighter than those of the other images. This is due to different preprocessings done by Brigham and Women's Hospital who provided the images. The intensities of these two images where thresholded rather than normalized.

image contains $256 \times 256 \times 123$ voxels each representing $1 \times 1 \times 1.5$ mm^3 with a possibility of 256 gray levels. A coronal slice of each of those images is shown in Figure 3.7 in which the subject's left side corresponds to the left side of the image. The images will be called $I_1, \ldots, I_{10}$, referring to the corresponding image when counting from left to right, top to bottom.

3.3.3 Results

We present the correction of morphometrical differences for a VOI in the left temporal lobe of the brain. The reference image is I_{10} in which we define a VOI of $64 \times 64 \times 20$ voxels of $1 \times 1 \times 1$ mm^3.

Figures 3.8 to 3.11 show the evolution of the VOIs throughout the correction procedure. The first image, Figure 3.8, presents the VOIs taken before any processing. It exhibits the differences due to intensity and positioning. After the first step which consists of intensity corrections and elimination of global morphometrical differences, the VOIs seem much more similar (see Figure 3.9).

Although affine dissimilarities are small, it is still possible to eliminate those variations by matching only the VOI images instead of the whole brain volume. Results of this second phase are shown in Figure 3.10. They represent corresponding VOIs and their differences are due only to morphology and local morphometry.

The third step is to eliminate those local morphometrical differences. After this (see Figure 3.11), we believe that only morphological differences are present.

3.4 Applications

Applications resulting from the correction of morphometrical differences can be divided in two categories: (1) studies of local morphometrical differences and (2) studies of morphological variations.

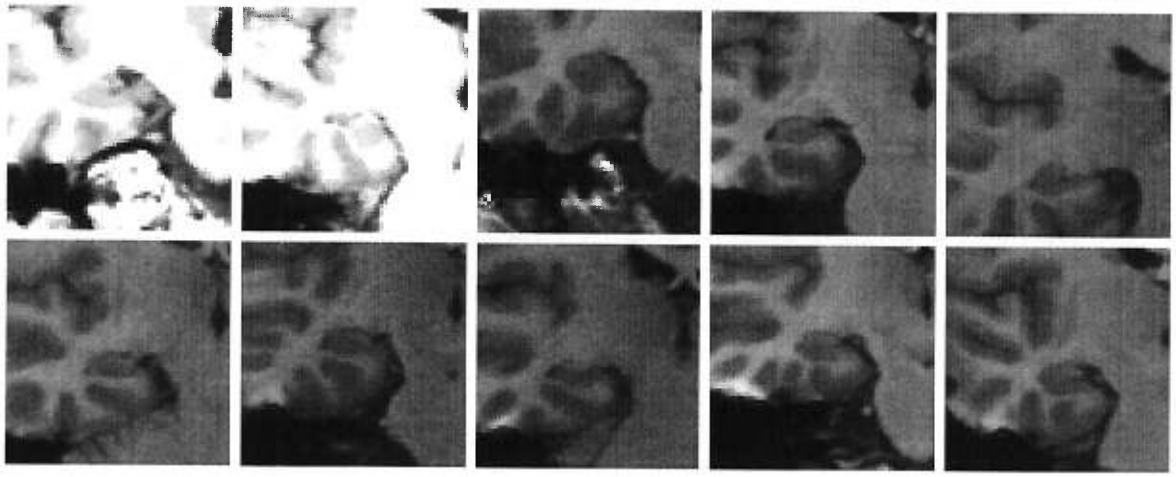

Figure 3.8: VOIs previous to any registration or intensity correction.

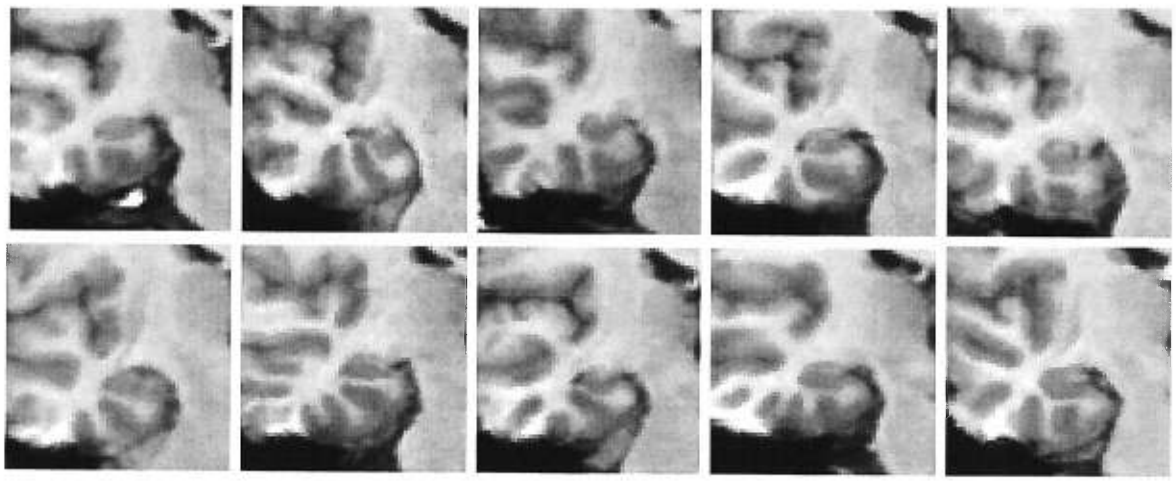

Figure 3.9: VOIs after global correction. Note that the global position of the VOI as well as the intensity differences between the images has been corrected.

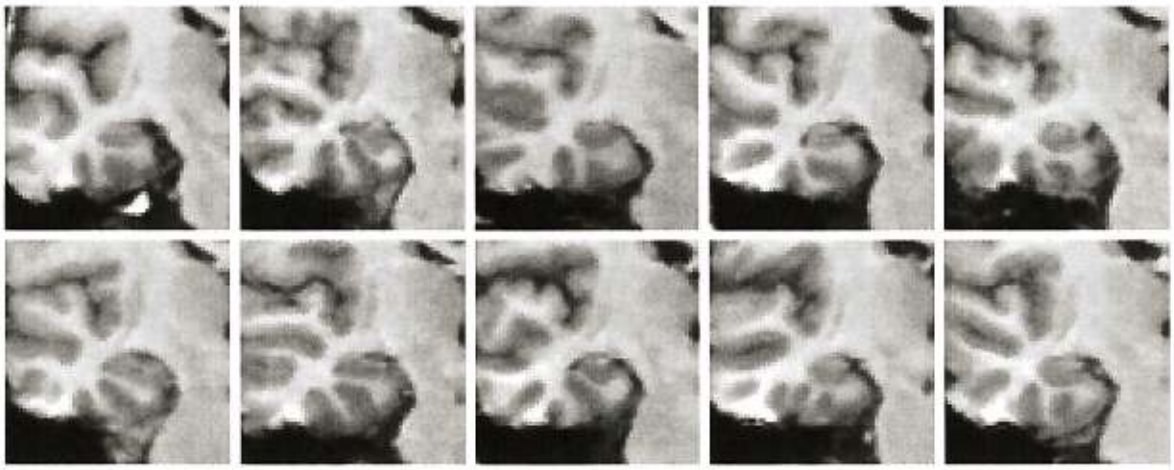

Figure 3.10: VOIs after regional correction.

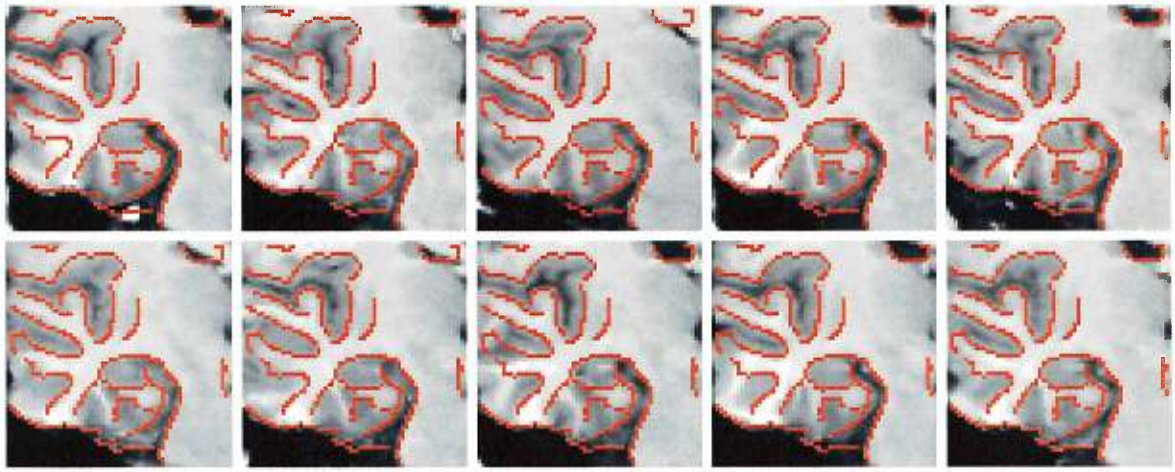

Figure 3.11: VOIs after all morphometrical correction. Contours obtained using a Canny-Deriche edge detector on I_{10} (last image of second row) were overlaid on each image to better assess the quality of registration.

3.4.1 Morphometrical Measures

This class of applications relies on measures of brain structures. For example, the comparisons of the basal ganglia's components volumes with a standard model to identify schizophrenia [51]. The construction of such a model relies on measures taken from a population of normal subjects. We have implemented this last idea.

Construction Method

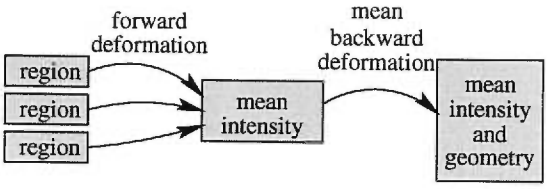

Figure 3.12: Procedure to build an average VOI from a set of images.

The idea behind the construction procedure is derived from [85, 84, 94, 21] and is depicted in Figure 3.12. Using the procedure described in section 3.3.1 on all the entries of the database, we can eliminate global and regional morphometrical differences to extract corresponding VOIs of our database. For each of those entries, we can compute the displacement field that maps the entry VOI onto the reference VOI (forward) and the reference VOI onto the entry VOI (backward). These displacements account for local morphometrical differences. The forward and backward displacement fields are found simultaneously so as to minimize the difference of their composition. This is done by removing from each displacement field at each iteration "half" of the residual transformation obtained by the composition of the forward and backward displacement fields. Applying to every region the forward displacement field produces images with the same morphometry as the reference VOI but with different intensities. Arithmetic averaging of corresponding voxel's intensities between VOIs produces a mean intensity image with the morphometry of the reference image and blurring due to residual morphometric variability not accounted for by the non-linear registration process. Furthermore, by applying the average backward displacement field to this last image, we eliminate the bias caused by the reference image and create a mean

intensity and morphometry representation of our database, or the "average" VOI.

Resulting "Average" Patients

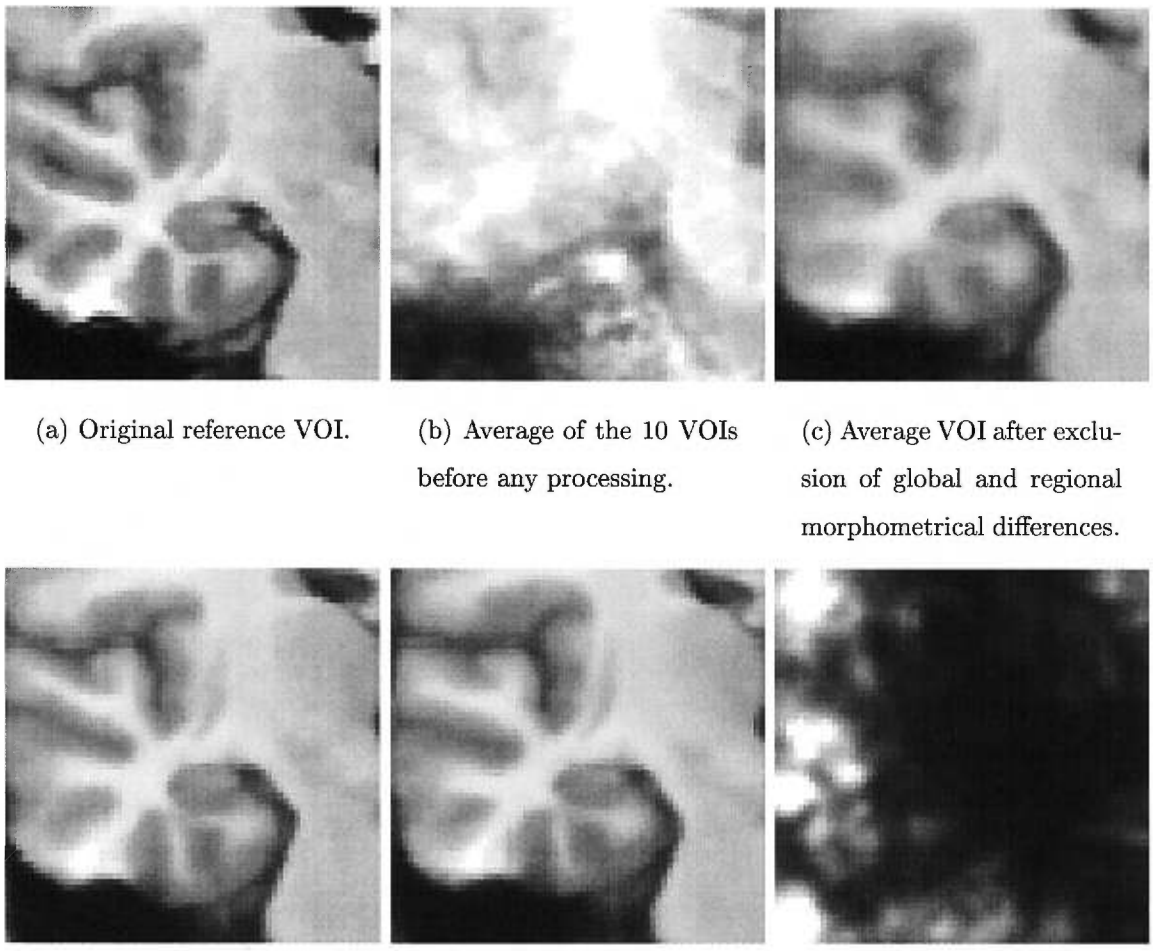

(a) Original reference VOI.

(b) Average of the 10 VOIs before any processing.

(c) Average VOI after exclusion of global and regional morphometrical differences.

(d) Average VOI without morphometrical differences (mean intensity).

(e) Average backward deformation applied to the average VOI without morphometrical differences (mean intensity and morphometry)

(f) Variance of the average backward deformation.

Figure 3.13: Different types of "average" patients.

Using all that has been computed up to now, we can obtain different kinds of "average" patients. Figure 3.13 shows such results. The first image is the reference VOI and is shown only for comparison purposes. To its right is a simple average of the VOIs taken from

each subject previous to any warping, putting forward the different patient positions during the acquisition. The intensity in this image is saturated because of I_1 and I_2 which have much higher intensity values than the other images. The third image presents the average of corresponding volumes of the database with intensity correction. Structures which are morphologically stable across subjects appear well contrasted while unstable ones are fuzzy. The first image of the second row is the average of the VOI intensities after elimination of morphometrical differences. Deforming this image with the average backward displacement field creates an image that represents the mean intensity and morphometry of the database, or the average VOI. It has the remarkable property of being an average image while not suffering from severe smoothing. Finally, we present the variance of the backward deformation fields' amplitude obtained from our database as a simple display of the variability of the different structures positions.

An advantage of our technique is that the average images it produces are of quality similar to the MR images of the database. Hence the same inter-patient matching method can be applied to compare a new patient to the average, which is an alternative to whole database exploration.

We have applied the same scheme to extract from the database the volumes that contain the ventricles. Averages have been built using the same method as for Figure 3.13 and are shown in Figure 3.14. The careful observer will notice that, although they were obtained using different methods, the average VOI after affine correction (Figure 3.14(c)) resembles a smoothed version of the average VOI (Figure 3.14(f)). This is especially true for the ventricles and strengthens the theory behind our method.

In this case, we have also applied to the segmented ventricles, the displacement field corresponding to the average local morphometrical differences. This permitted to construct ventricles that represent the average morphometry of our database. They are shown in Figure 3.15. To the left, the original ventricles and to its right, a display of their average morphometry. An obvious difference is the posterior tails of the lateral ventricles which are thinner for the average patient than for the original ventricles.

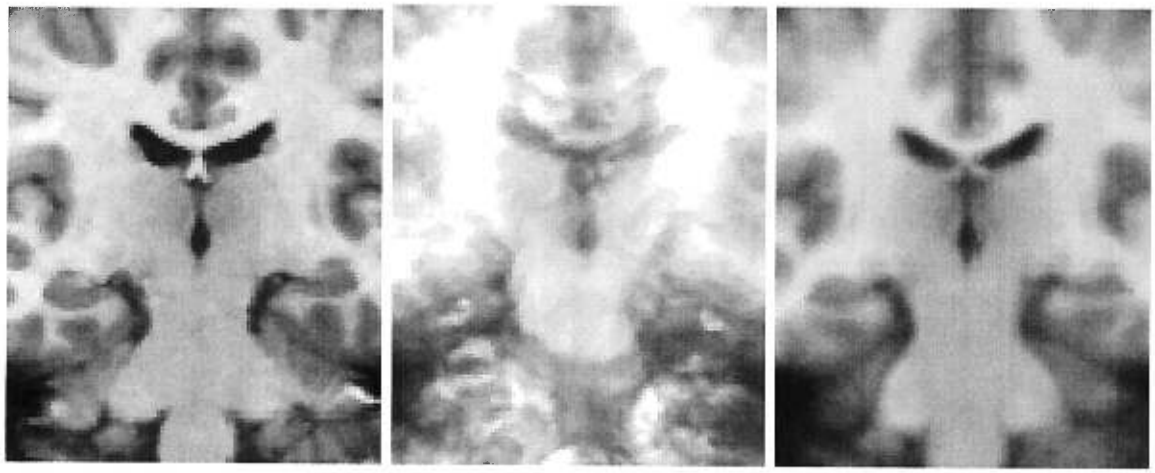

(a) Original reference VOI.

(b) Average of the 10 VOIs before any processing.

(c) Average VOI after exclusion of global and regional morphometrical differences.

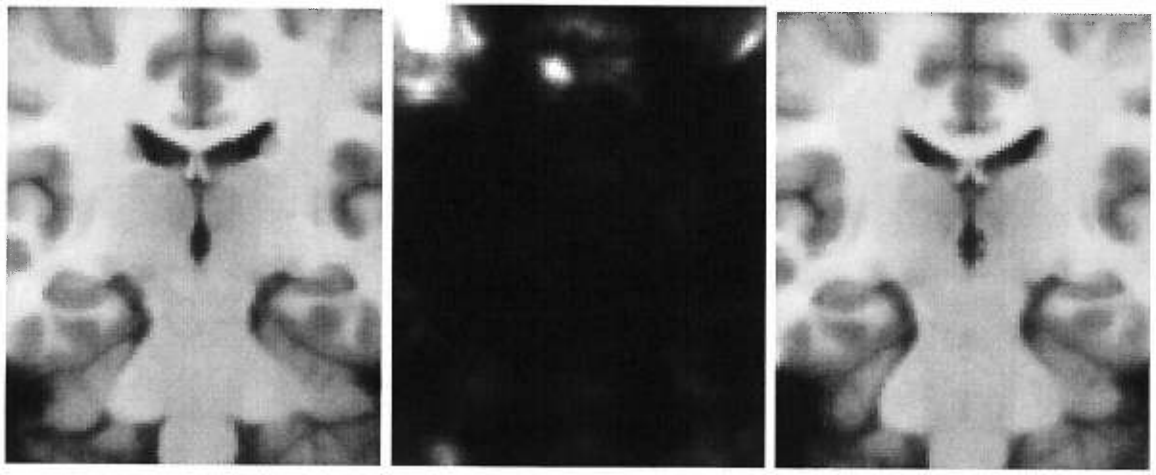

(d) Average VOI without morphometrical differences (mean intensity).

(e) Variance of the average backward deformation.

(f) Average backward deformation applied to the average VOI without morphometrical differences (mean intensity and morphometry)

Figure 3.14: Average VOI obtained from free-form registration.

Figure 3.15: **Left**: original ventricles. **Right**: morphometrical average ventricles of the database.

3.4.2 Morphological Measures

This class of applications is concerned with the presence or absence of features. Following this, we have just begun experiments to classify similar patients according to their morphology. This work requires methods related to sorting subjects, or more generally, the development of similarity criteria. There is a large literature on this topic [31, 73] but our goal here is neither to find the best measure nor to analyze its relationship with our registration procedure. We wish to show practical applications of VOI extraction and evaluate qualitatively different similarity criteria. Hence, the following experiments are to be considered as a first step of a feasibility study. Furthermore, the images at our disposal are of normal subjects. Consequently, we are not trying to evaluate pathologies or find anomalies.

Among available choices, we have chosen two: (1) the stochastic sign-change (SSC), which is based on zero-crossings, and (2) correlation. The method consists of extracting morphometrically corresponding VOIs automatically from the database using the method previously described. We then define a *working space* in which comparisons are done (see

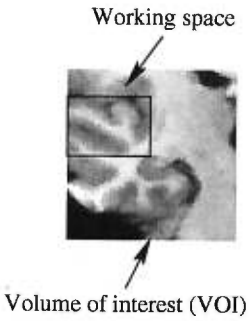

Figure 3.16: A slice of the VOI and working space. Only the working space is considered for comparisons.

Figure 3.16). We present the criteria used and show preliminary results of VOI classification according to their resemblance with I_{10}.

The Stochastic Sign-Change Criterion

This criterion was introduced by Venot *et al.* [100] for the comparison of scintigraphic images. It is a measure of similitude between two images and is based on zero-crossings (see Figure 3.17).

Let I_1 and I_2 be similar images that contain noise and $S = I_1 - I_2$. Originally, I_1 and I_2 are identical. Then, S is not zero but contains sign fluctuations because of noise. However, if the two images differ from one another in some region R of S, R will contain either mostly positive or mostly negative values and the number of sign changes in S is reduced. This shows that a high SSC count in S is a good indication of resemblance between two images.

To count the number of sign changes, we go through the subtraction image three times. Once comparing values in the X direction, once in the Y direction and a last time for the Z direction. This criterion can be normalized by considering the maximal value of SSC in the working space. Hence, values close to 1 shows good similitudes, and those close to 0, poor correspondence.

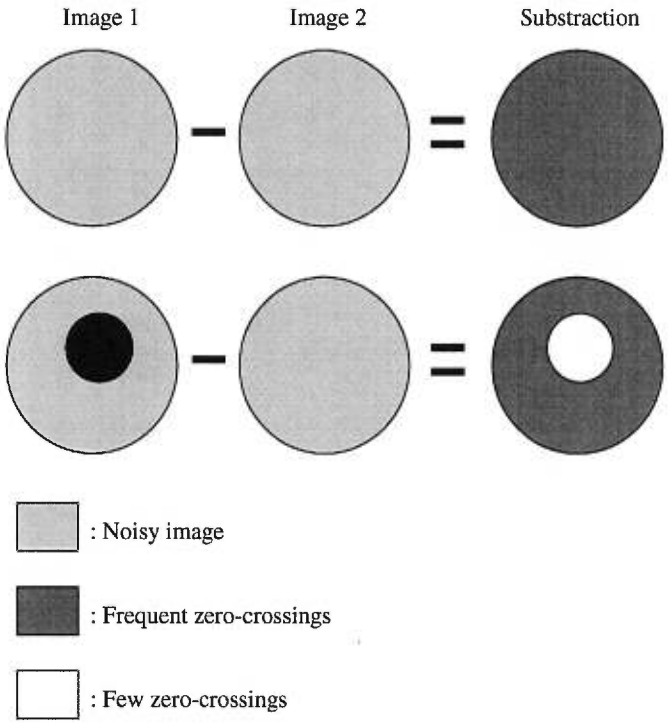

Figure 3.17: The stochastic sign-change criterion.

Correlation

The correlation between two working spaces X and Y each containing N voxels is computed using the following formula:

$$\mathbf{Corr}(X,Y) = \frac{\mathbf{Cov}(X,Y)}{\sqrt{\mathbf{Var}(X)\mathbf{Var}(Y)}} \tag{3.1}$$

where

$$\begin{aligned} \mathbf{Cov}(X,Y) &= \frac{1}{N}\sum_{i=1}^{N} X_i Y_i - \frac{1}{N^2}\sum_{i=1}^{N} X_i \sum_{i=1}^{N} Y_i \\ \mathbf{Var}(X) &= \mathbf{Cov}(X,X) \\ \mathbf{Var}(Y) &= \mathbf{Cov}(Y,Y) \end{aligned}$$

Image	SSC value (normalized)
10	1.000
4	0.325
7	0.315
6	0.305
9	0.285
5	0.284
3	0.282
2	0.279
8	0.271
1	0.268

Table 3.1: Classification using the SSC criterion.

Image	Correlation
10	1.000
4	0.917
6	0.906
3	0.906
1	0.888
7	0.879
5	0.858
9	0.845
8	0.844
2	0.836

Table 3.2: Classification using correlation.

Slice 1:

(a) I_{10} (1.000) (b) I_4 (0.325) (c) I_7 (0.315) (d) I_6 (0.305) (e) I_9 (0.285)

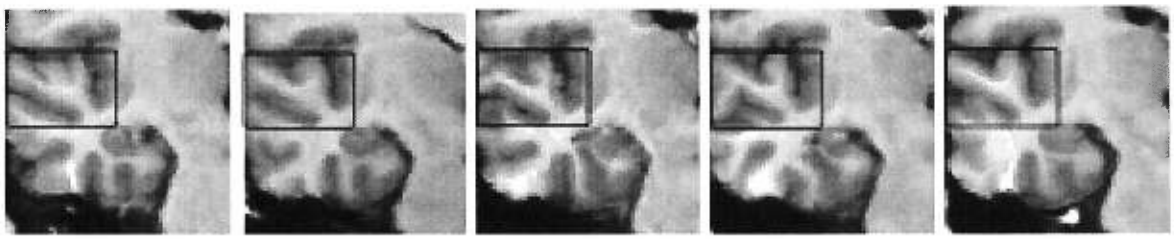

(f) I_5 (0.284) (g) I_3 (0.282) (h) I_2 (0.279) (i) I_8 (0.271) (j) I_1 (0.268)

Slice 2:

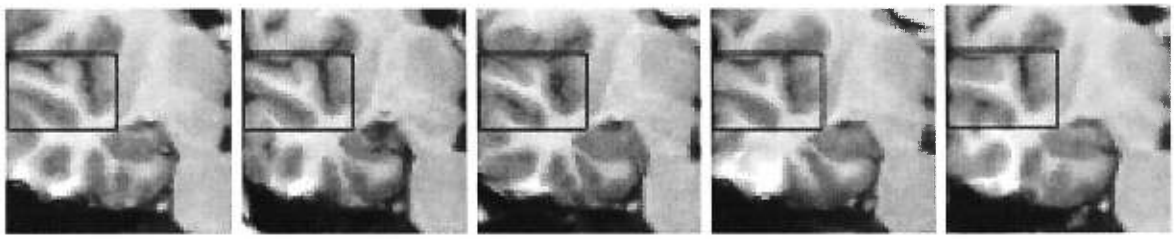

(k) I_{10} (1.000) (l) I_4 (0.325) (m) I_7 (0.315) (n) I_6 (0.305) (o) I_9 (0.285)

(p) I_5 (0.284) (q) I_3 (0.282) (r) I_2 (0.279) (s) I_8 (0.271) (t) I_1 (0.268)

Figure 3.18: Classification using the SSC criterion. Two volume slices are shown. SSC values are in parenthesis.

Slice 1:

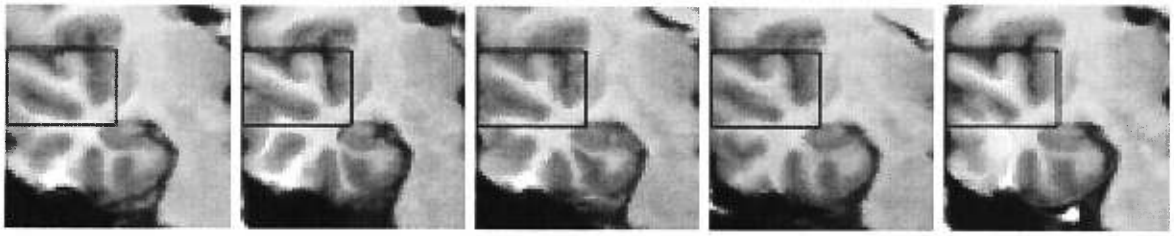

(a) I_{10} (1.000) (b) I_4 (0.917) (c) I_6 (0.906) (d) I_3 (0.906) (e) I_1 (0.888)

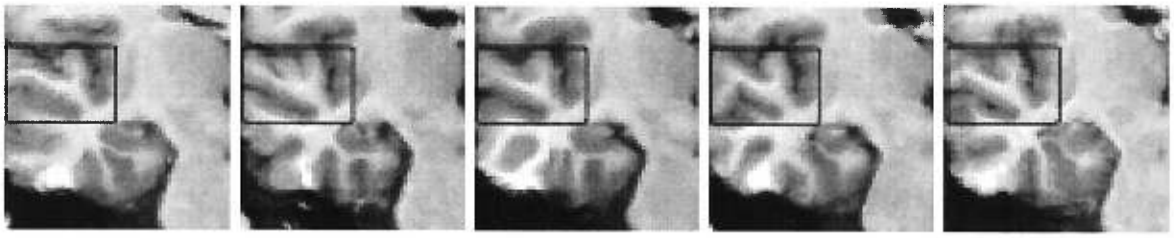

(f) I_7 (0.879) (g) I_5 (0.858) (h) I_9 (0.845) (i) I_8 (0.844) (j) I_2 (0.836)

Slice 2:

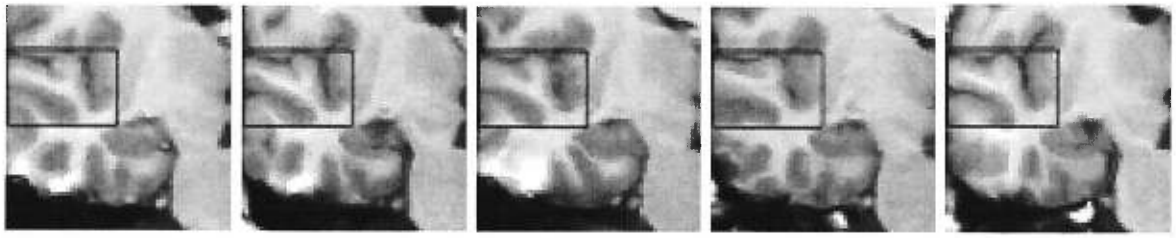

(k) I_{10} (1.000) (l) I_4 (0.917) (m) I_6 (0.906) (n) I_3 (0.906) (o) I_1 (0.888)

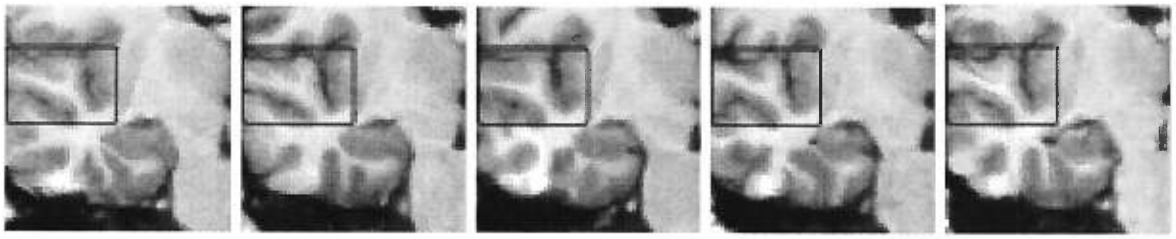

(p) I_7 (0.879) (q) I_5 (0.858) (r) I_9 (0.845) (s) I_8 (0.844) (t) I_2 (0.836)

Figure 3.19: Classification using correlation. Two volume slices are shown. Correlation values are in parenthesis.

Results

The SSC values are shown sorted in Table 3.1 and correlation coefficients in Table 3.2. We also present, using this ordering, the working spaces used for computations in Figures 3.18 and 3.19. Each of these figures contains two non-adjacent slices of the VOIs to get a better understanding of the tridimensional structure. They show the importance to our three dimensional approach since one would probably change this disposition by only looking at one slice.

The ordering obtained with the SSC criterion and with correlation are similar up to minor permutations. The only large difference has to do with I_1 which is identified as having the most different morphology using the SSC criterion and is placed fifth using correlation. By looking at both slices of this VOI, we can see that it is quite similar to I_{10}. Hence, preliminary results seem to indicate that correlation would be more appropriate to evaluate morphological differences than the SSC criterion. On light of those results, comparisons based on mutual information techniques are expected to give good classifications.

Although in this case we used an elastic registration procedure before classification, when assuming negligible morphological variations, this classification method can be used on corresponding VOIs thus using only affine transformation for registration purposes. In this case, an order on local morphometrical differences would be obtained.

3.4.3 Discussion

The main benefit of this method is that it is fast and fairly robust. The time to obtain the corresponding VOIs varies between 5 and 10 seconds on a DEC AlphaStation 400 4/233, and local warping doubles this time. This opens a new door on medical image database exploration. It is now possible to retrieve a large amount of corresponding volumes in a reasonable amount of time. Once those volumes extracted, further processing like classification and similarity matches can be operated to result into extrapolation of information contained in the database to other images. For example, this technology is presently being used for the study of morphometrical hippocampal variations in epileptic patients. We have only started to explore this field but preliminary results are encouraging.

3.5 Conclusion

We have presented a new method to obtain corresponding volumes of interest from medical image databases. This procedure has the advantage of restraining itself to local volumes of the brain and thus is not influenced by misleading information from other regions. It has been applied to the quantification of morphometrical and morphological variations. We believe that better results could be obtained by dividing subjects into subclasses of normal patients based on morphological similarities. This would facilitate the analysis of only morphometrical differences, to provide a better understanding of dissimilarities between a patient and the group of normal subjects with corresponding morphology.

Future applications and research on classification and extraction of similar patients for epidemiology statistics or computer aided diagnosis are envisioned. Such applications are a first step toward the extrapolation of information from an image database to other images.

Acknowledgments

Thanks to Dr. Ron Kikinis of Brigham and Women's Hospital, Boston, for the MR images. Part of this work was funded by the Natural Sciences and Engineering and Research Council of Canada (NSERC), the Fonds pour la Formation de Chercheurs et l'Aide à la Recherche du Québec (FCAR), the Association des Directeurs de Recherche Industrielle du Québec (ADRIQ) and the Département d'Informatique et de Recherche Opérationnelle de l'Université de Montréal (DIRO).

Chapitre 4

Modèles moyens et atlas probabilistes

Sommaire

Avant-propos

Nous présentons dans le chapitre suivant [42] une méthode complètement automatique de construction de modèle moyen anatomique « stable » du cerveau humain à partir d'un ensemble d'images de résonance magnétique (RM). Les modèles calculés présentent deux caractéristiques importantes : une intensité moyenne ainsi qu'une forme moyenne, les deux dans une même image. Nous fournissons des résultats montrant la convergence vers le centroïde

de l'ensemble d'images utilisé pour le calcul du modèle. En particulier, la distance moyenne entre les voxels des modèles et leurs correspondants anatomiques dans les images de RM se stabilise à l'intérieur d'un intervalle allant de 2.88 mm à 3.36 mm après une seule itération, cet intervalle allant initialement de 4.62 mm à 5.51 mm. Quant à l'influence de l'image cible choisie pour la construction du modèle, elle est minimale avec des différences d'environ 1 mm, celles-ci étant initialement d'approximativement 3.5 mm. Ces résultats assurent l'utilité de notre approche.

Brièvement, notre méthode identifie à partir d'images de RM les différences de forme entre les cerveaux étudiés. Les différences dues à des transformations linéaires (translation, rotation, changement d'échelle et cisaillement) sont exclues. Ceci permet de mettre de côté principalement les différences de position du patient dans le scanner ainsi que la taille de cerveau, donnant pour résultat la quantification de différences morphologiques pures. Le résultat est une image d'intensité et de forme moyenne représentant les caractéristiques des éléments de l'ensemble d'images utilisé pour la construction. En outre, nous montrons que ce modèle correspond au centroïde de l'ensemble d'images et ne dépend pas de l'image de référence utilisée pour son calcul. Cette stabilité est très importante pour assurer l'efficacité et l'utilité de notre méthode.

Dans l'article qui suit et contrairement à l'article précédent, le terme « morphologique » est employé pour signifier « morphologique et morphométrique ». Cet abus de langage est fréquemment rencontré dans la littérature.

L'article qui suit est une version modifiée d'un article publié selon la référence bibliographique suivante :

> A. GUIMOND, J. MEUNIER, et J.-P. THIRION. « Average Brain Models: A Convergence Study ». *Computer Vision and Image Understanding*, 1999. À paraître.

Average Brain Models: A Convergence Study

Abstract

We present a completely automatic method to build "stable" average anatomical models of the human brain using a set of magnetic resonance (MR) images. The models computed present two important characteristics: an average intensity and an average shape, both in a single image. We provide results showing convergence toward the centroid of the image set used for the computation of the model. In particular, the RMS distances between the model and the MR images contained in the set stabilize in a range of 2.88 mm to 3.36 mm from a range of 4.62 mm to 5.51 mm initially after only one iteration. As for the influence of the reference image chosen for the model construction, this is minimal with differences of about 1.0 mm, from approximately 3.5 mm initially. These results demonstrate the usefulness of our approach.

4.1 Introduction

An important tool used to diagnose abnormal anatomical variations are medical atlases [68]. Traditional ones, such as by Talairach & Tournoux [88] or Schaltenbrand & Wahren [81], are presented in textbooks, but computerized atlases comprising information in a more practical and quantitative manner are becoming available [3, 39, 61, 50, 26, 8, 16, 56, 60, 105, 40, 96, 86]. They usually include information obtained from a set of subjects, as opposed to a single individual in most paper atlases, making them more representative of a population. For example, the Montreal Neurological Institute (MNI) used three hundred and five (305) normal subjects to build an atlas comprising intensity variations after affine registration in the stereotactic space defined by Talairach & Tournoux [26]. These methods also enable the calculation of normal shape variations, such as in the work of Gee *et al.* [36] which present a statistical framework for the construction of upgradable statistical atlases, and Thompson & Toga [97] which presents a probabilistic atlas of the human brain based on random vector field transformations.

The following work aims to develop and validate a concept drafted in a previous paper [45] to build an average model of the human brain using a set of magnetic resonance (MR) images

obtained from normal subjects. This model has two important characteristics: average tissue intensity and average tissue shape up to an affine transformation. We intend to demonstrate that the model construction converges toward the centroid of the MR image set.

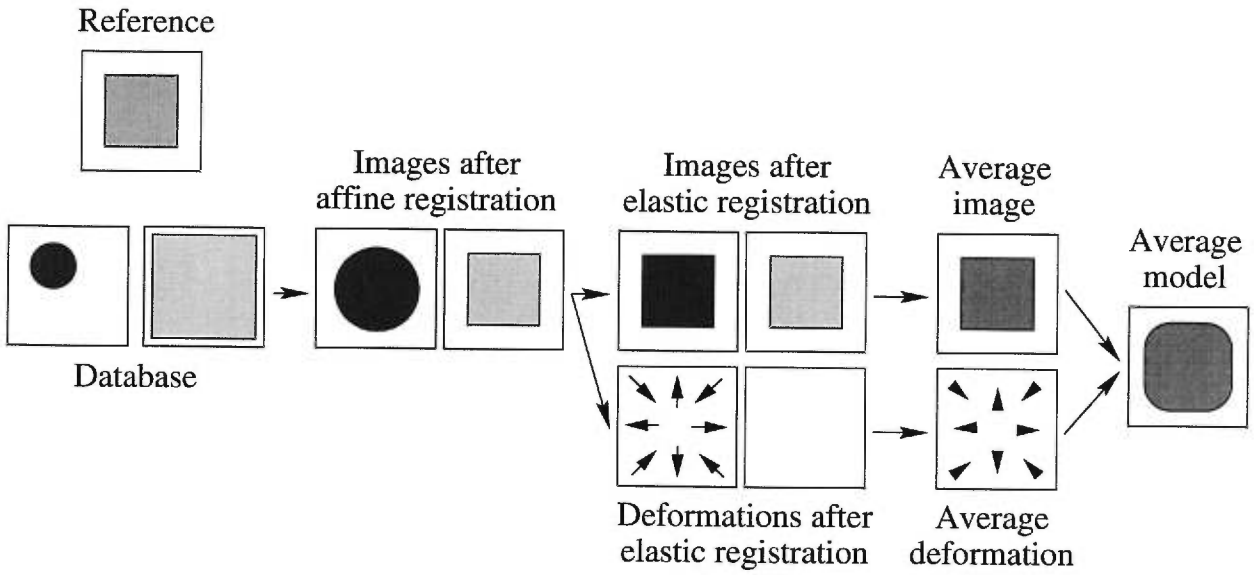

Figure 4.1: Average model construction method.

As depicted in Figure 4.1, our method can be summarized in the following manner. Affine registration between all the images of the set and a reference image corrects for positioning and global shape differences due to translation, rotation, scaling and shearing, as well as global linear intensity variations due to acquisition parameters or preprocessing. These are variations that are not of concern for our study. Elastic registration is then used to evaluate residual variations due to pure morphological differences and produces images having the same shape as the reference. Averaging the residual deformations, which are the inverses of the transformations that map each image of the set to the reference image, and the locally registered images yields an average deformation and an average intensity image, respectively. The average deformation is then applied to the average image to produce the model. It presents in a single image an average intensity and shape modulo an affine transformation corresponding to the affine characteristics of the reference image.

Although similar in terminology, the average shape and the average intensity characteristics have different purposes. The average shape represents an average of *morphological*

variations. This is generally a well understood concept. On the other hand, the average intensity is meant to average the *response of corresponding tissues to the acquisition parameters.* Also, assuming Gaussian noise in each MR scan, the average intensity increases the signal to noise ratio in the resulting model compared with individual scans.

The main contributions of this paper are the description of a fully automatic technique to obtain an *average intensity* and *shape* image, producing the *average model* M, and to show that this model, up to an affine transformation, is stable with respect to the choice of the initial reference image and repeated applications of the algorithm (iterations).

The most similar work regarding average intensity atlases is that of Bookstein [7] who created from nine MR scans a two-dimensional image representing the average intensity of the mid-sagittal plane. Thirteen manually identified landmarks in the mid-sagittal plane of each scan where matched with a reference image using the thin-plate spline interpolant [6]. The nine resampled images where then averaged to result into a morphometric average atlas. Our method differs mainly by two aspects. First, as suggested by Bookstein [7], we make full use of the three-dimensionality of the scans to compute a three-dimensional average image. Second, our registration method is automatic and computes a dense deformation field instead of an interpolated function based on thirteen landmarks. This deformation identifies for each voxel of the reference the corresponding positions in the other scans. Within this process, every voxel of the reference can be thought of as a landmark automatically determined in the other scans.

The work of the MNI group [26], where three hundred and five (305) three-dimensional MR scans were registered using translations, rotations and scalings, and averaged to build a statistical neuroanatomical model, also relates to our work. We enrich this idea by proceeding further in using a less constrained type of deformation after the affine match to accommodate for local shape variations.

In the same vein, Woods *et al.* [105] describe a method that finds from a set of images a common space that preserves the average orientation, size, and affine shape of the group by registering all possible pairs of images it contains. Averaging the images after affine mapping to this common space produces an average intensity brain atlas in the average affine space. Their method is computationally very intensive as it requires $n(n-1)/2$ registrations, n

being the number of subjects in the group. The basic difference between this approach and the one by the MNI group is that this one finds the average affine space, whereas the MNI method uses Talairach space.

The average shape concept is most similar to the beautiful work of the Brown/Washington groups [40, 70], who have put together a framework in which the construction of a template from a set of anatomies is proven to minimized the energy of the deformations required to map it onto all the elements of that set. Our work complements theirs in that we provide quantitative measurements confirming their formulation, though we do not compute small deformations as is required for their proof. It should be noted that our resulting model also includes average intensity information and that our respective groups use different registration methods.

Le Briquer and Gee [60] have also developed a method that provides, for a given group of subjects, the mean shape and the modes of principal variation along with their amplitude. Their approach is set in a statistical framework and aims at deriving a shape model. Our method differs in that we aim at the analysis of local information rather than global patterns.

The work presented here also relates to the methodologies of Subsol *et al.* [86], Bookstein [9] and Kendall [55] who compute average shapes modulo similarity or affine transformations. We have not tried to strictly follow the theory developed in their works. Our intention was to conform to the idea of making abstraction of differences between images due to first order transformations, and analyze residual variations. Our main contribution resides in the characteristics used to build the average shape, that is the image intensities instead of landmarks or crestlines. Again, this enables the computation of dense deformations fields representing variations everywhere is the MR scan, as opposed to interpolating transformations found using landmarks, lines or surfaces. We believe this technique may find less accurate matches in the close surroundings of the landmarks, but provides better overall registration.

As will be shown, compared to these previous efforts, our method provides clearer images with higher contrasts and sharper definitions of tissue boundaries. Most importantly, we provide numbers showing the convergence of the model towards the centroid of the image set.

The remaining sections of this paper are organized in the following manner. First, we detail the method used to construct the average model. We then present results showing the convergence of the method towards an average intensity and shape model, and show the effect of the choice of reference image. We conclude by a discussion on future research tracks.

4.2 Methodology

4.2.1 Registration

The work that follows assumes each point in one image has a corresponding equivalent in the others. It also assumes available a matching method able to find these correspondences and capable of providing a vector field representing those relationships. In practice, neither of these conditions is realized. That is, at a microscopic scale, there is not a one-to-one relationship between the brain cells of two individuals, and assuming there was, to this day, no algorithm is able to find it. However, deforming one brain so its shape matches the one of another is conceivable and many algorithms realizing this process have been developed [6, 3, 17, 22, 95, 36, 105]. The procedure used in the following work is the demons method [93] using a complete grid of demons. We briefly detail it here and refer the reader to the original article for more information.

Evaluating Shape Differences

When applied to MR images, the demons algorithm can be considered as an optical flow variant [52]. From this point of view, the 3D images to be registered are considered as a time sequence represented by $I(x,t)$ where $x = (x_1, x_2, x_3)$ is a voxel position in the image and t is time. It computes forces by constraining the brightness of brain structures to be constant in time so that

$$\frac{dI(x,t)}{dt} = 0. \tag{4.1}$$

This leads us to the basic optical flow formulation (See [52] for details about the derivation.),

$$v = -\nabla_x I(x,t) \frac{\partial I(x,t)/\partial t}{||\nabla_x I(x,t)||^2}, \tag{4.2}$$

which is the movement component in the direction of the brightness gradient $\nabla_x I(x,t) = \left(\frac{\partial I(x,t)}{\partial x_1}, \frac{\partial I(x,t)}{\partial x_2}, \frac{\partial I(x,t)}{\partial x_3}\right)$. For numerical stability reasons when $\nabla_x I(x,t)$ is close to zero, the denominator of the above formula is modified to result in the basic displacement formulation for the demons algorithm using a complete grid of demons,

$$v = -\nabla_x I(x,t) \frac{\partial I(x,t)/\partial t}{||\nabla_x I(x,t)||^2 + |\partial I(x,t)/\partial t|^2}. \tag{4.3}$$

When $||\nabla_x I(x,t)|| = 0$ no displacement is computed.

As with all optical flow formulations based on differential techniques, the problem here resides in finding the components of the movement in the directions orthogonal to the gradient. Many regularization methods have been proposed [5] each with their strengths and weaknesses. The one proposed by Thirion is to apply a Gaussian filter to each of the three components of v. This provides a smooth displacement field in a time efficient way. It is interesting to note that Bro-Nielsen and Gramkow [13] have shown that regularizing the deformation field using a Gaussian filter approximates linear elasticity.

The method is iterative and makes use of a multi-scale scheme which resolved the problem of finding large deformations, a common problem with optical flow techniques and a basic assumption in the formulation and implementation of the derivative filters.

Relaxing the Intensity Constraint

We mentioned that the registration algorithm assumes the same intensity for corresponding brain structures in the images to be registered. For all sorts of reasons, such as acquisition parameters or preprocessing, this may not be the case. To relax this constraint, a linear intensity correction is evaluated at each iteration of the registration procedure. It is obtained by finding the line that best fits the joint histogram of the two images (See Figure 4.2). This line is obtained using linear regression and outlier rejection. From experience, we know that such an intensity correction provides images in which boundary definitions are clearer and better matched.

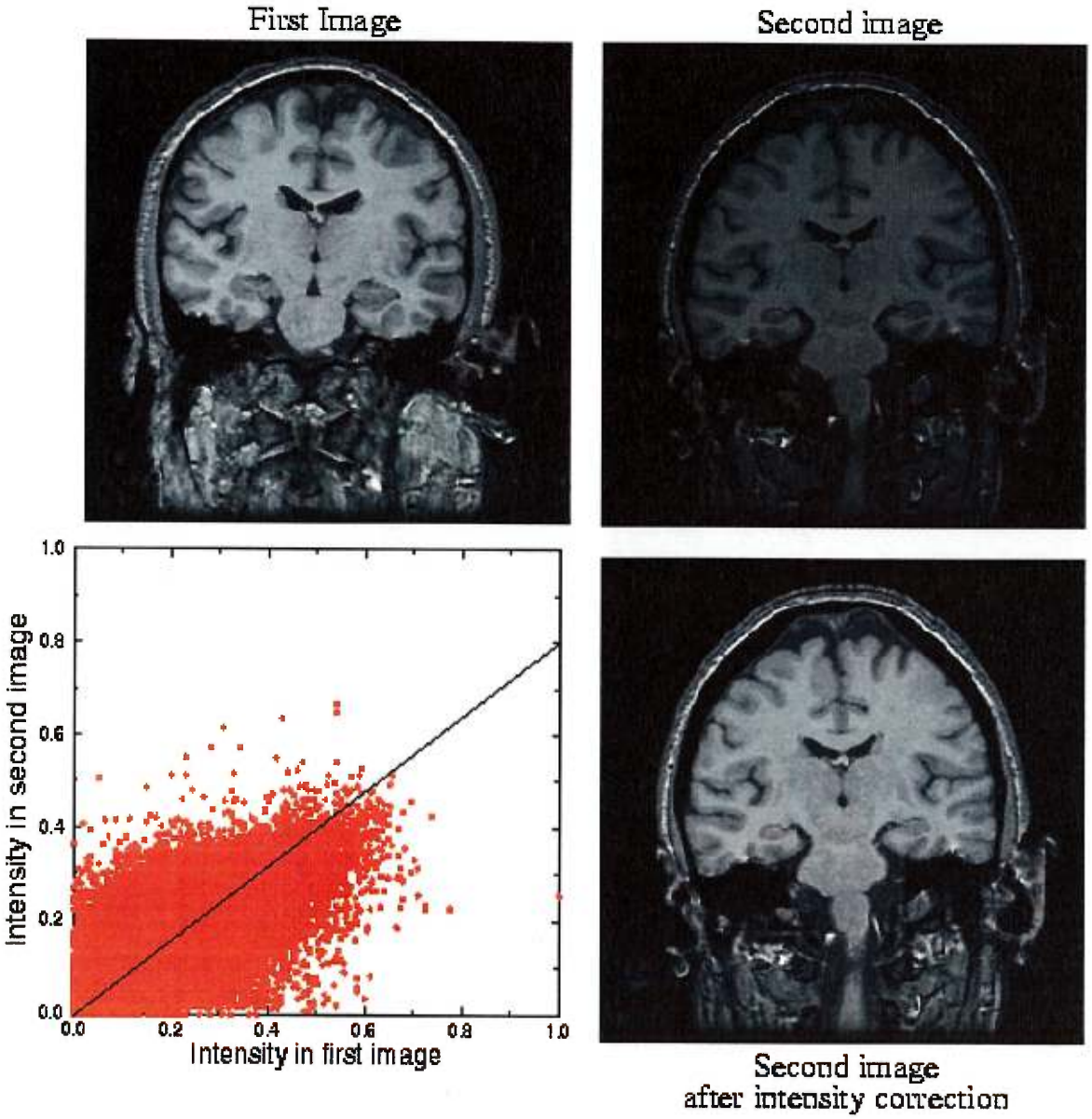

Figure 4.2: Intensity correction method.

Relevance of the Resulting Transformation

In the case of inter-subject non-rigid registration, quantifying the accuracy of a method is difficult. One could deform an image I using a known deformation D into I', register I with I' and compare the result of the registration with D, but this comparison is biased by the way D is generated. For example, since the demons algorithm produces a smooth deformation field, if the vectors of D were to be generated randomly, the method is expected to perform poorly. Another method is to place landmarks in the images to register and evaluate differences between landmarks after registration (See for example [105]). No such study has been performed using the demons algorithm.

An approach which is a generalization of the previous one is to compare manual and automatic segmentation using segmentation propagation, the manual result serving as ground truth (See for example [48]). We believe this approach may be better suited to evaluate the quality of high dimensional transformations such as the ones obtained using the previously described algorithm (typically $3 \times 200^3 = 24 \times 10^6$ degrees of freedom). Such a study has been perform previously by Dawant *et al.* [24] for the demons algorithm. To summarize their work, contours of different brain structures, large and small, have been segmented manually on nine MR images. One of these images was mapped to all eight other images. Then, manual and propagated segmentations were compared. Their similarity index is defined as two times the area encircled by both contours divided by the sum of the areas encircled by each contour. This index ranges from zero to one, with zero indicating zero overlap and one indicating a perfect agreement between two contours. It is sensitive to both displacement and differences in shape and it is thus preferable to a simple area comparison. The average similarity indices between the manual and automatic segmentations were 0.96, 0.97 and 0.845 for the whole head, the cerebellum and the head of the caudate respectively. Compared with intra-rater results of 0.97, 0.97 and 0.88, the difference in the mean similarity indices between two manual delineations and between the manual delineations and the automatic segmentation method are statistically significant for the whole head and the caudate but not for the cerebellum. The authors put forth though that similarity indices over 0.85 correspond to contours that are virtually indistinguishable and that a more relevant comparison should

be performed using inter-rater manual results which are known to have more discrepancies.

It should be pointed out that the demons algorithm does not explicitly track the transformation's Jacobian to make sure its determinant is positive, so that in theory it is possible to obtain a singular transformation. In our experience on MR data, this does not occur when using a sigma of 1 voxel to define the Gaussian filter for the smoothing operation. Also, the algorithm matches intensities and a *global* intensity correction is made over the whole image. Hence the transformed image is not an exact duplicate of the target. This is due to the smoothness constraint applied to the displacement field which establishes a compromise between intensity resemblance and uniform local deformations at each iteration and thus in the final result.

4.2.2 Average Model Construction

The average model construction needs as input a reference image I_R and a set S of N images $I_1, \ldots, I_N$ representing the group of subjects under consideration. The method can be divided in six steps as follows:

1. The first step is the evaluation of global shape and intensity differences between the reference and each image of the set. Elastic registration between I_R and I_i provides vector fields D_i giving for each voxel x_R of I_R the corresponding anatomical location x_i in I_i as well as an intensity transformation IT_i. An affine transformation A_i that best approximates, in a least squares sense, the corresponding D_i is computed. Since we have correspondences between anatomical points of the I_i and I_R that have the form $x_i = D_i(x_R)$, we compute the A_i by minimizing the distance $\sum_x ||x - A_i^{-1}(D_i(x))||^2$ (See for example [27] for a closed form), where the summation is performed on the voxel positions in I_R corresponding to cerebral tissues[1].

2. In the second step, residual variations due to pure morphological differences are calculated. Elastic registration is performed between I_R and each I_i using the corresponding

[1]These positions are obtained using an automatic method for brain segmentation similar to that of Brummer *et al.* [14]. From hereon, all summations over x are assumed to be on the voxel positions obtained using this algorithm.

A_i and IT_i as initial transformation estimates. This provides the resulting matched images I_i' as well as the residual vector fields R_i.

3. The third step averages the I_i', producing a mean intensity image $\overline{I}$ with the shape of I_R.

4. The fourth step aims to produce the deformation presenting the shape variations between I_R and the average shape of the set elements after correction of affine differences. Since the residual deformations R_i are all defined in the same anatomical space, that of I_R, calculating their vectorwise average $\overline{R}(x) = 1/N \sum_i^N R_i(x)$ will provide the desired deformation.

5. The fifth and final step consists of applying this average residual deformation to the average intensity image to obtain an average intensity and shape image representing the anatomical average model M. To avoid the cumbersome computation of the inverse of a vector field, we use forward resampling [43] with mathematical morphology [38] to guarantee continuity.

Considering numerical errors due to the fact that automatic registration methods usually perform better when images are closer to each other, all these steps may be repeated by replacing I_R with M, thus constructing a model with a reference image closer to the centroid of our set. Intuitively, this should reduce the mean registration error and provide a new model M' closer to the theoretical solution.

In the next section we will further study this convergence with respect to the choice of the reference image I_R and the number of iterations needed to achieve convergence.

4.3 Results

The method is tested by computing four models using two reference images I_{R_1} and I_{R_2} (see Figures 4.3(a) and 4.3(b)) and two image sets S_1 and S_2, each composed of five images (see Table 4.1).

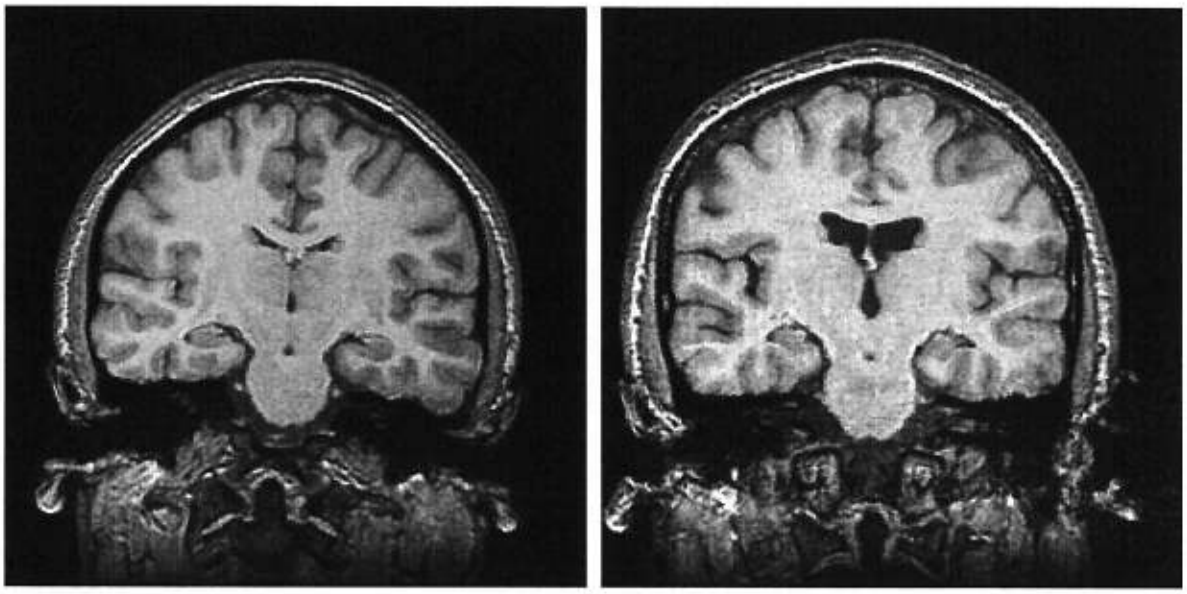

(a) A coronal slice of I_{R_1}.

(b) A coronal slice of I_{R_2}.

Figure 4.3: Coronal slices from the two reference images I_{R_1} and I_{R_2} respectively.

Model	**Reference**	**Image Set**
$\mathbf{M_{11}}$	I_{R_1}	S_1
$\mathbf{M_{21}}$	I_{R_2}	S_1
$\mathbf{M_{12}}$	I_{R_1}	S_2
$\mathbf{M_{22}}$	I_{R_2}	S_2

Table 4.1: References and image sets used to build the different models.

The 3D MR protocol provides coronal images obtained using a 1.5 Tesla SIGNA (General Electric, Milwaukee, U.S.A.) whole body MR imaging system. One hundred and twenty four (124) coronal T1-weighted images were obtained using a spoiled gradient echo (SPGR) pulse sequence (TE=9 milliseconds, TR=34 milliseconds, flip angle=45^o). Two NEX acquisitions took 27 minutes and 52 seconds. The Field of View (FOV) of the images was 20 cm and each image refers to a contiguous section of tissue of 1.6 mm thickness. The two acquisitions, as opposed to one, gave increased contrast to noise ratio between gray and white matter, and therefore better definition of structure boundaries. The images showed no evidence of movement or chemical shift artifacts, and partial voluming effects were minimal. The acquisition time was well tolerated by all subjects. The $256 \times 256 \times 124$ voxels of size $0.78 \times 0.78 \times 1.6$ mm^3 were trilinearly interpolated to $200 \times 200 \times 198$ to give cubic voxels of 1 mm side.

We analyze our results with regards to two factors. First, the iteration process is investigated to see if convergence is achieved, and if so, how fast the convergence rate is. Second, we study the effect of changing the reference image. If the model is a true average of the image set, changing the reference should produce an identical model up to an affine transformation defined by the affine difference between references.

In our evaluation procedure, three metrics are used. The first determines the average distance (AD) from an image I to the elements of a set S,

$$\mathrm{AD}(I,S) = \sqrt{\frac{1}{n}\sum_{x}\frac{1}{N}\sum_{i=1}^{N}||x - R_i(x)||^2}, \tag{4.4}$$

where R_i is the residual deformation from I to the ith element of S, n is the number of voxels characterizing cerebral tissues and N represents the number of elements in S.

The second is the root mean square norm (RMSN) which supplies information regarding the shape variation expressed by a deformation field D,

$$\mathrm{RMSN}(D) = \sqrt{\frac{1}{n}\sum_{x}||x - D(x)||^2}, \tag{4.5}$$

where n is the number of voxels characterizing cerebral tissues in the reference from which D was obtained.

The third provides a measure of brightness disparity between two images I_i and I_j. It is the normalized intensity difference (NID) of the images intensities at corresponding locations,

$$\mathrm{NID}(I_i, I_j) = \sqrt{\frac{\sum_x (I_i(x) - I_j(x))^2}{\sum_x (I_i(x))^2}}. \tag{4.6}$$

An easy way to interpret this formula is to notice that if $I_j = I_i$, $\mathrm{NID}(I_i, I_j) = 0$; if $I_j = 2I_i$, $\mathrm{NID}(I_i, I_j) = 1$; if $I_j = \frac{1}{2}I_i$, $\mathrm{NID}(I_i, I_j) = 0.5$; and so on.

4.3.1 Effect of Iterating

To evaluate the effect of iterating, we construct the four models repeating the process five times and using the result of the previous iteration as the reference image. We will designate the model M_{jk}, obtained with reference image I_j and set S_k, computed at the ith iteration by $M_{jk}^{(i)}$. For convenience, $M_{jk}^{(0)}$ will be identified to the average intensity image having the shape of I_j. This represents a sort of iteration after applying only the three first steps described in section 4.2.2.

Four measures were computed:

AD$(M_{jk}^{(i)}, S_k)$ The average distance from the reference of the current iteration to all the elements of the set.

RMSN$(\overline{R}_{jk}^{(i)})$ The shape variation expressed by the residual deformation field $\overline{R}_{jk}^{(i)}$ when $M_{jk}^{(i)}$ is used as the reference.

RMSN$(D_{jk}^{(i)})$ The shape difference between models computed at successive iterations. $D_{jk}^{(i)}$ is the deformation obtained by registering $M_{jk}^{(i)}$ with $M_{jk}^{(i+1)}$.

NID$(M_{jk}^{(i)}, M_{jk}^{(i+1)})$ The brightness disparity between models obtained at successive iterations.

If the models computed tend towards the centroid of the image set, the first measure should diminish. This process is depicted in Figure 4.4(a): as the model evolves towards the center (dotted line), the average distance to the image set elements decreases. The second and third measures, representing the shape evolution of the model (see Figure 4.4(b)), should

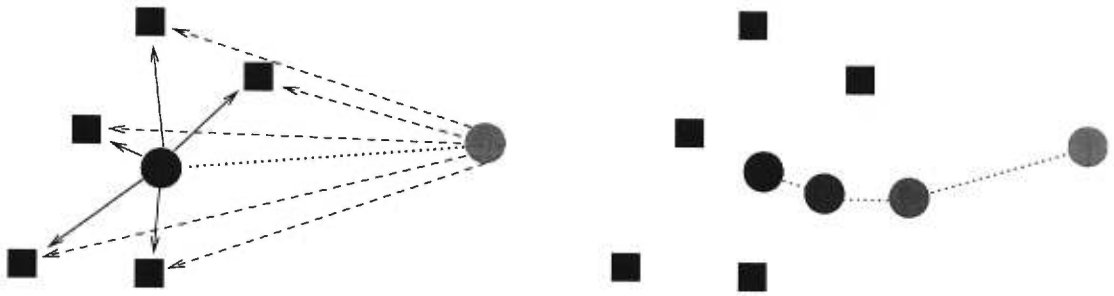

(a) The average distance of the model to the image set elements decreases.

(b) The distance between successive models diminishes.

Figure 4.4: Evolution of the model (circles) toward the center of the image set (squares).

tend towards zero. Finally, the fourth value should also decrease to zero since it represents the brightness differences between successive models.

The results of these calculations on the four models are presented in Figure 4.5. Note that the iterations range up to 4 and not 5 since we compare models computed at iterations i and $i+1$. We remind the reader that "models" $M_{jk}^{(0)}$, that is models before the first iteration, characterize only average intensities and not average shapes.

From Figure 4.5(a), we know the average distance from the references to the image set elements is between 4.62 mm and 5.51 mm and reduces to a range of 2.88 mm to 3.36 mm. Notice that the average distances for the models build using the same image set are very close (0.09 mm for both models) while the distance for the models built using different image sets is much higher (in the range of 0.30mm to 0.48 mm, depending of which models are compared). This is easily explainable by the fact that different small image sets will tend to have different average distance from their centroid. Compared to these values, the variation between successive models (see Figure 4.5(b) and 4.5(c)), which is in the range of 0.41 mm to 0.52 mm, seems minor. Figure 4.5(d) presents numbers showing the brightness difference between successive models diminishes rapidly to almost 0, increasing our belief that models do not evolve significantly after the first iteration.

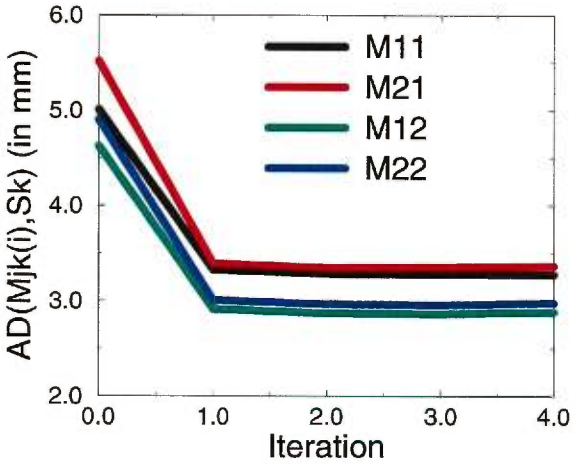

(a) Average distance to the reference of the current iteration.

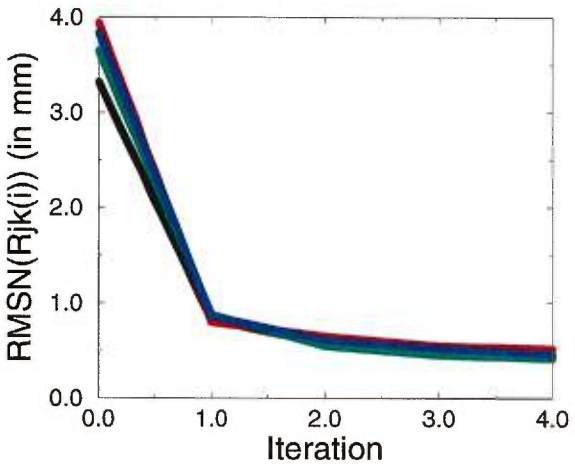

(b) Shape variation of the reference for the current iteration.

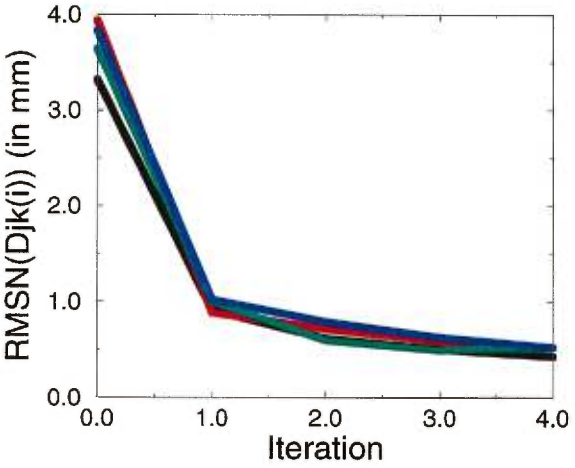

(c) Shape difference between models computed at successive iterations.

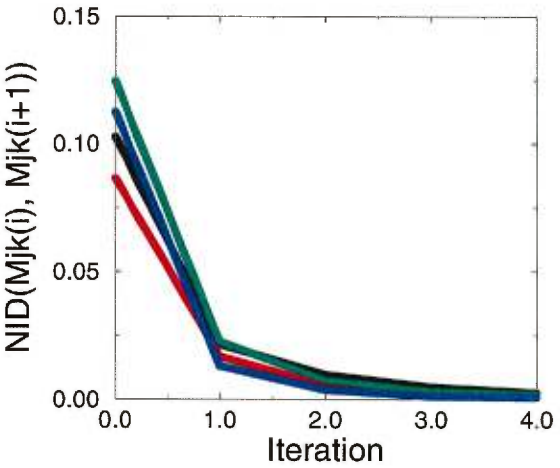

(d) Brightness disparity between models computed at successive iterations.

Figure 4.5: Impact of the iteration process when computing the models. Note that the iterations range up to 4 and not 5 since we compare models computed at iterations i and $i+1$. We remind the reader that "models" $M_{jk}^{(0)}$, that is models before the first iteration, characterize only average intensities and not average shapes.

4.3.2 Effect of the Reference

If the models computed are equal up to an affine transformation, changing the reference image should produce a model identical to the previous one after removing their affine differences. To verify this characteristic, we performed an *affine* registration between models built using the same image set. $M_{21}^{(i)}$ is registered with $M_{11}^{(i)}$ to provide the image $M'^{(i)}_{21}$ and $M_{22}^{(i)}$ with $M_{12}^{(i)}$ to result in $M'^{(i)}_{22}$.

Two measures were used:

RMSN($D_k^{(i)}$) The shape variation from $M_{1k}^{(i)}$ to $M'^{(i)}_{2k}$. $D_k^{(i)}$ is the deformation obtained by registering the two images.

NID($M_{1k}^{(i)}$, $M'^{(i)}_{2k}$) The brightness disparity between the two models.

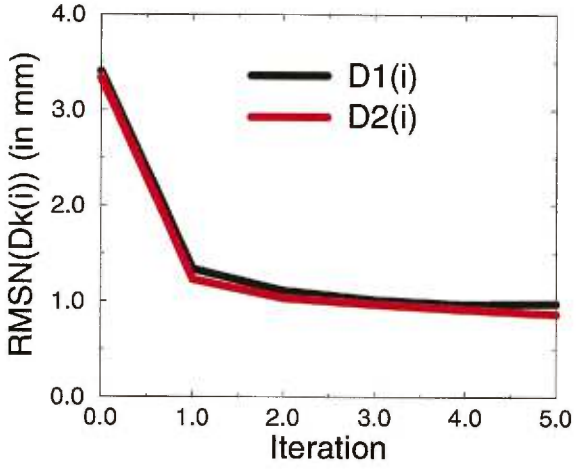

(a) Shape variation between $M_{1k}^{(i)}$ and $M'^{(i)}_{2k}$.

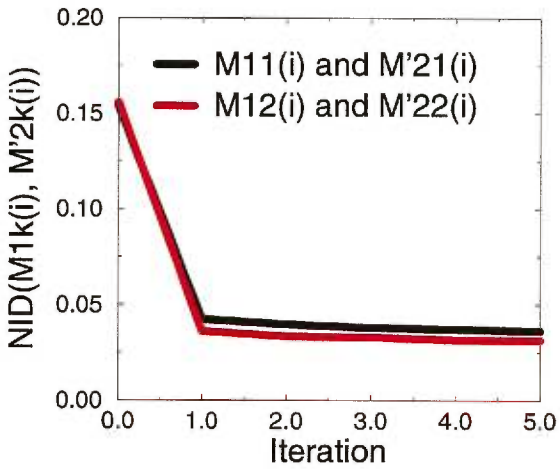

(b) Brightness disparity between $M_{1k}^{(i)}$ and $M'^{(i)}_{2k}$.

Figure 4.6: Influence of the reference on the model computed.

Results are shown in Figures 4.6(a) and 4.6(b) respectively. We notice that shape variation between the models reduces from about 3.4 mm to 0.9 mm. This last value is close to the difference between successive models which we know from Figures 4.5(b) and 4.5(c) to be approximately 0.4 mm. The brightness disparity also diminishes rapidly and does not change drastically after the first iteration. From these results, one can see that the models

built using different reference images are very close but not identical. We believe the differences are due to errors in our registration method and to the resampling procedure applied to the models to put them in the same affine space, which tends to smooth the image. This last artifact is not present when comparing models obtained from successive iterations as we did for the results of Figure 4.5(d). Still, the average distance between models is less than the resolution of the image, and both the average distance and the normalized intensity difference evolve only slightly after the first iteration.

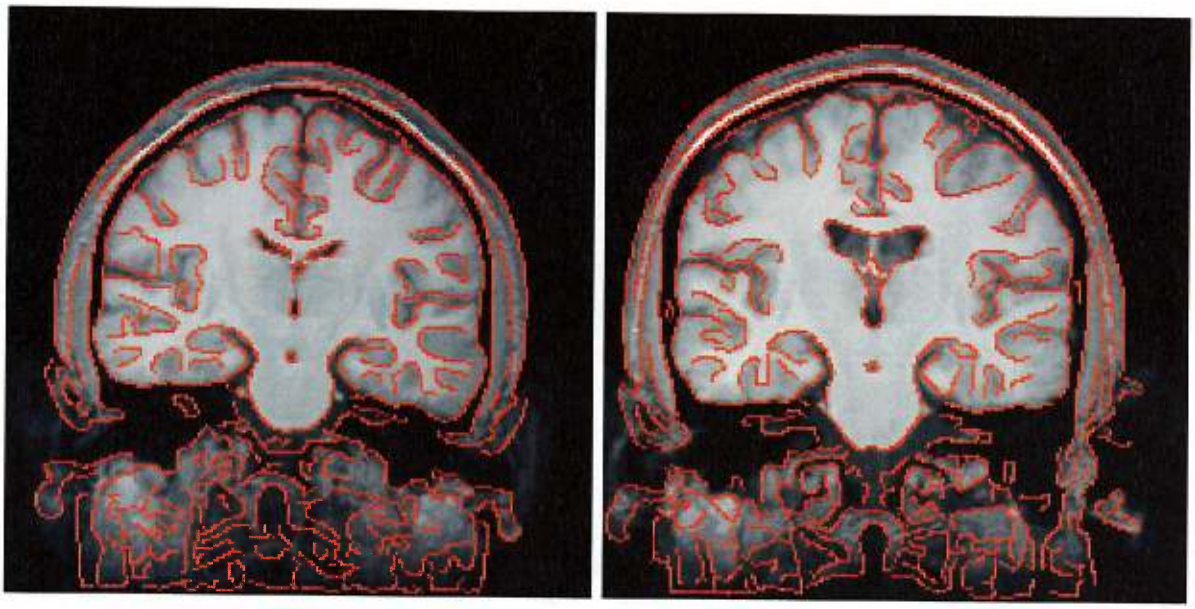

(a) Average intensity image $\overline{I}$ build using I_{R_1} and S_1 during first iteration.

(b) Average intensity image $\overline{I}$ build using I_{R_2} and S_1 during first iteration.

Figure 4.7: Average intensity images build using reference images I_{R_1} (Figure 4.3(a)) and I_{R_2} (Figure 4.3(b)) and the same image set S_1. They were obtained during the first iteration of the model construction method. Notice how the signal to noise ratio is increased while contrast is preserved. The overlaid contours on Figure 4.7(a) and Figure 4.7(b) were obtained using a Canny-Deriche edge detector on I_{R_1} (Figure 4.3(a)) and I_{R_2} (Figure 4.3(b)) respectively to help evaluate shape discrepancies.

Figures 4.7 to 4.10 present some results obtained during this process. In Figure 4.7 the average intensity images corresponding to the reference images of Figure 4.3 are presented. They basically have the same shape as their respective reference image and their intensities

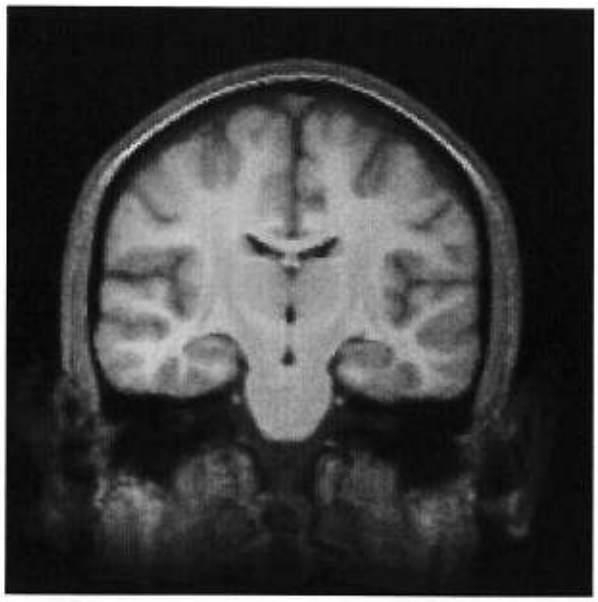

(a) A coronal slice of $M_{11}^{(1)}$.

(b) A coronal slice of $M_{21}^{(1)}$.

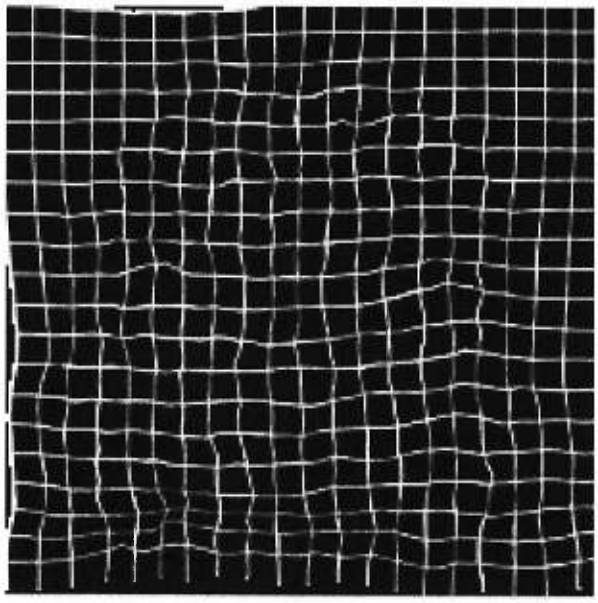

(c) A regular grid deformed by the average residual deformation $\overline{R}_{11}^{(0)}$.

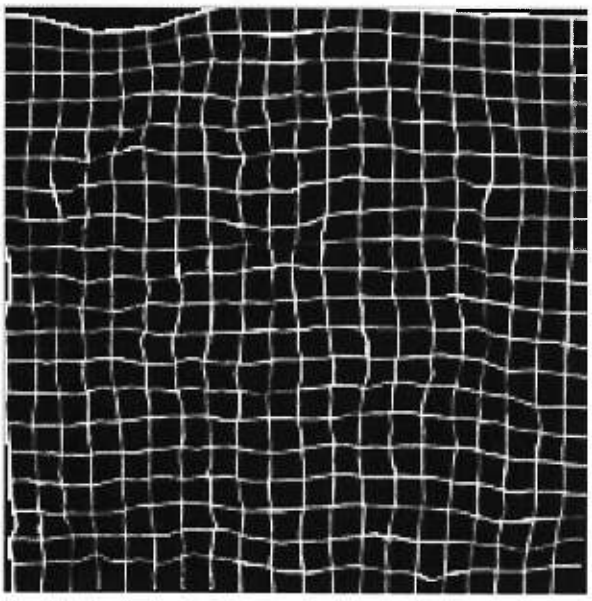

(d) A regular grid deformed by the average residual deformation $\overline{R}_{21}^{(0)}$.

Figure 4.8: Average models $M_{11}^{(1)}$ (Figure 4.8(a)) and $M_{21}^{(1)}$ (Figure 4.8(b)) computed using reference images I_{R_1} (Figure 4.3(a)) and I_{R_2} (Figure 4.3(b)) and the same image set S_1. They were built from the average intensity images of Figure 4.7(a) and Figure 4.7(b) respectively. Figures 4.8(c) and 4.8(d) are the corresponding deformed grids.

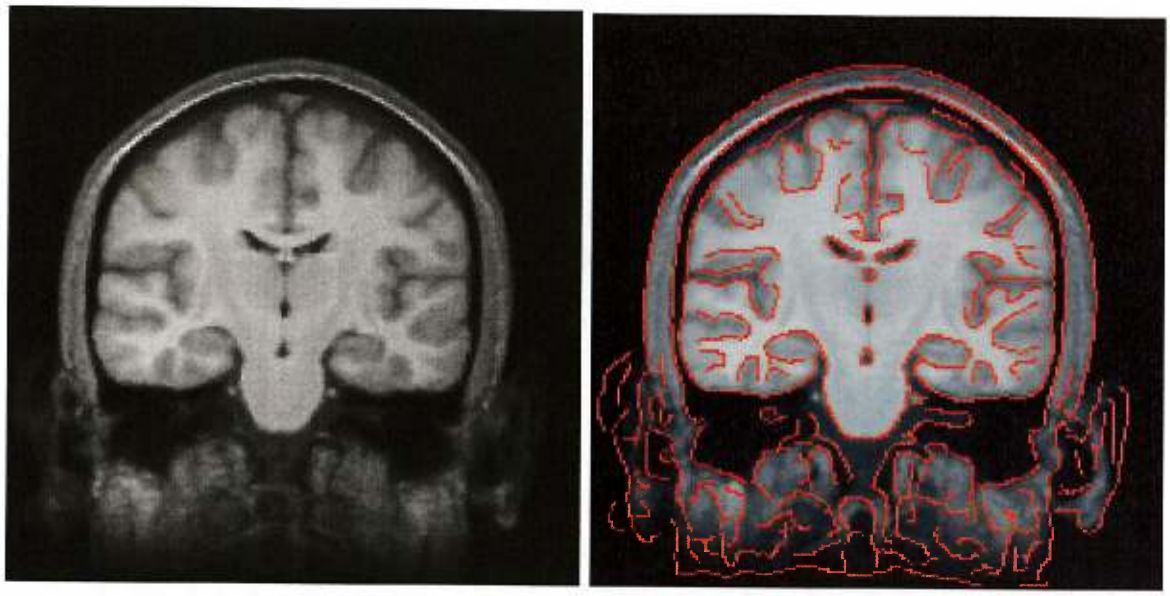

(a) A coronal slice of $M_{11}^{(1)}$.

(b) A coronal slice of $M'^{(1)}_{21}$.

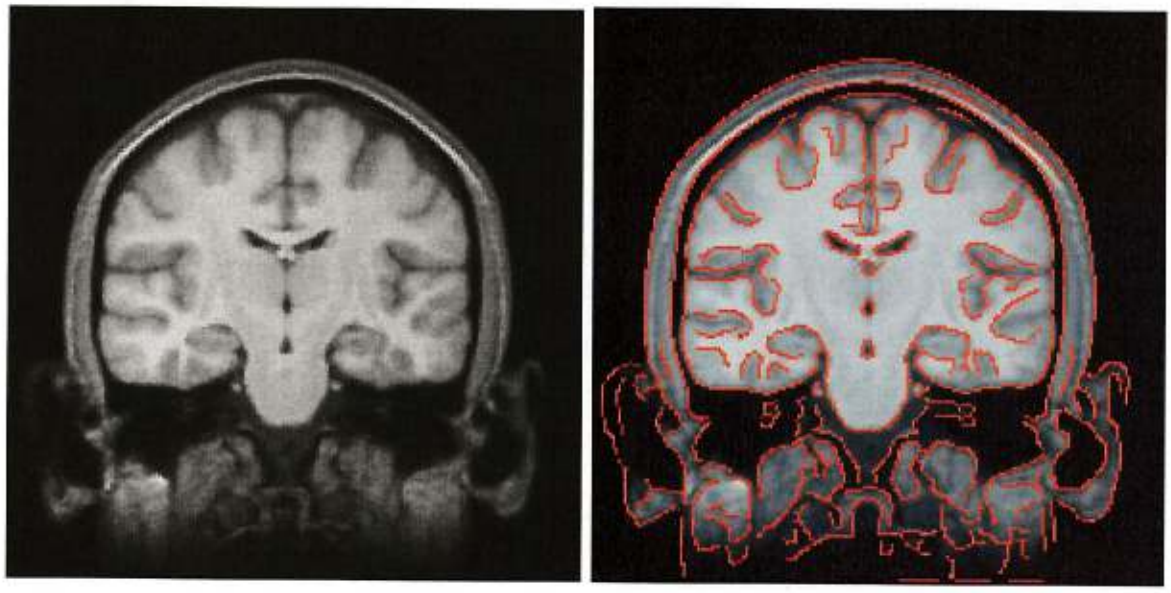

(c) A coronal slice of $M_{11}^{(5)}$.

(d) A coronal slice of $M'^{(5)}_{21}$.

Figure 4.9: Average models computed using reference images I_{R_1} (Figure 4.3(a)) and I_{R_2} (Figure 4.3(b)) and the same image set S_1. Figures 4.9(b) and 4.9(d) have been transformed into the same affine space as Figures 4.9(a) and 4.9(c) respectively, and can therefore be compared directly. The overlaid contours on Figure 4.9(b) and Figure 4.9(d) were obtained using a Canny-Deriche edge detector on Figure 4.9(a) and Figure 4.9(c) respectively to help evaluate shape discrepancies.

(a) A coronal slice of $M_{11}^{(5)}$.

(b) A coronal slice of $M'^{(5)}_{21}$.

Figure 4.10: Average models computed using reference images I_{R_1} (Figure 4.3(a)) and I_{R_2} (Figure 4.3(b)) and the same image set S_1. Figure 4.10(b) has been transformed into the same affine space as Figure 4.10(a) and can therefore be compared directly. Compared with Figure 4.9, these slices are taken where there is more variability in the cortex area and thus where our registration method finds correspondences in which we have less confidence. As can be seen, in these regions the model image is less clear and the contrast between gray and white matter is less pronounced. The overlaid contours on Figure 4.10(b) were obtained using a Canny-Deriche edge detector on Figure 4.10(a) to help evaluate shape discrepancies.

correspond to the average of the image set S_1. Notice how the signal to noise ratio is increased while contrast is preserved. These average intensity images are deformed using the corresponding average residual deformations to provide the average models of Figure 4.8. The average model $M_{21}^{(1)}$ is then registered with $M_{11}^{(1)}$ using an affine transformation to set it in the same affine space. This result is presented in Figures 4.9(a) and 4.9(b). The same procedure has been performed for all five iterations for both image sets S_1 and S_2. The resulting models for the fifth iteration using image set S_1 is also shown in Figures 4.9(c) and 4.9(d). In Figure 4.10, slices are taken where there is more variability in the cortex area and thus where our registration method finds correspondences in which we have less confidence. As can be seen in these regions, the model image is less clear and the contrast between gray and white matter is less pronounced.

4.4 Discussion

Figure 4.5 presents numbers showing that our method constructs average models well representing the average intensity and shape of our image sets. In particular, Figure 4.5(a) shows that the average distance from one image to the set elements varies between 4.62 mm and 5.51 mm. This distance reduces and stays between 2.88 mm to 3.36 mm after the first iteration. Figure 4.5(b) and 4.5(c) illustrate a minor shape evolution of the models at each iteration. Furthermore, Figure 4.5(d) allows us to claim the visual aspect of the models changes only minimally. This leads us to the conclusion that models constructed are different, but equivalent from a practical point of view. That is, we believe the model slowly wanders around the optimum solution. Their intensity difference is practically null, and their shapes, although different, all have the same average distance to the other elements of the set. Hence, we believe one or two iterations are sufficient to build representative average models.

The reader should appreciate the low noise, high contrast and high quality of the models produced in Figures 4.8, 4.9 and 4.10. They present models built using different reference images and the same image set. The ventricular shape bias introduced using I_{R_2} is minimal if not null. Also, Figure 4.6 shows that the models built using different references seem

to converge towards the same solution. Their shape difference presented in Figure 4.6(a) of about 0.9 mm is low compared to the average distance between the models and the set elements, which is in the range of 2.88 mm to 3.36 mm, and just over the distance between successive average models which varies from 0.30 mm to 0.48 mm. Figure 4.6(b) also presents a low disparity between the different models intensities.

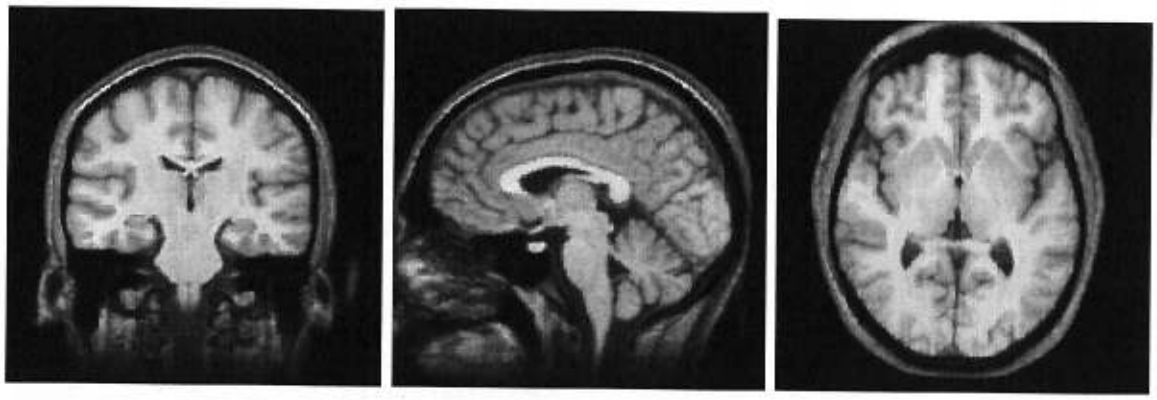

(a) Coronal slice, elastic registration.

(b) Sagittal slice, elastic registration.

(c) Axial slice, elastic registration.

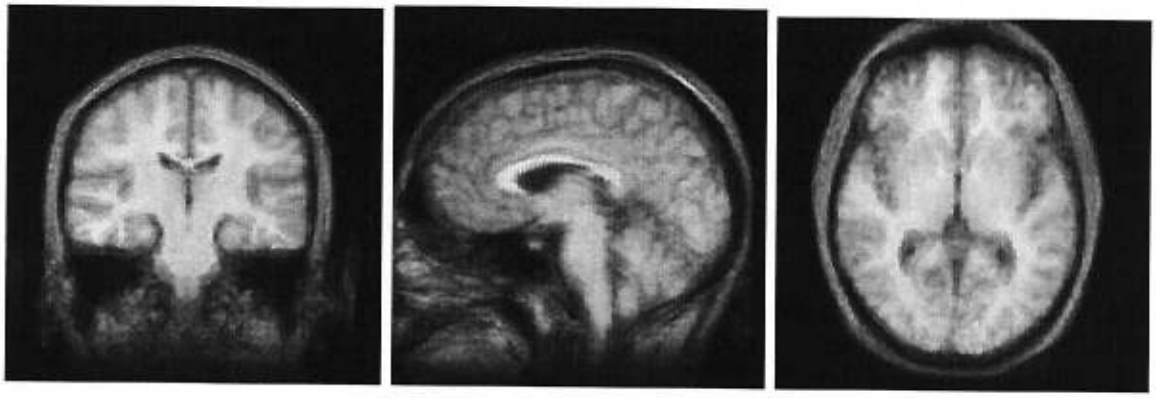

(d) Coronal slice, affine registration.

(e) Sagittal slice, affine registration.

(f) Axial slice, affine registration.

Figure 4.11: Corresponding slices of M_{11} using affine registration (Figures 4.11(d), 4.11(e) and 4.11(f)) instead of elastic registration (Figures 4.11(a), 4.11(b) and 4.11(c)).

If familiar with the work of Bookstein [7] or the MNI group [26], the reader will appreciate the high contrast and visual quality of the images produced, although due in part to the smaller number of images used. To better visually appreciate the gain in using high-dimensional volumetric maps ($200^2 \times 198 \times 3 = 2.376 \times 10^7$ degrees of freedom) instead of

affine transformations (12 degrees of freedom) during registration, Figure 4.11 presents corresponding slices of the model M_{11} built using the method presented in this paper and the one built restraining registration to affine transformations. Note that Figures 4.11(a), 4.11(b) and 4.11(c), obtained using the method described above, provide higher contrasts and sharper definitions of tissue boundaries than Figures 4.11(d), 4.11(e) and 4.11(f) which where obtained using affine registration only.

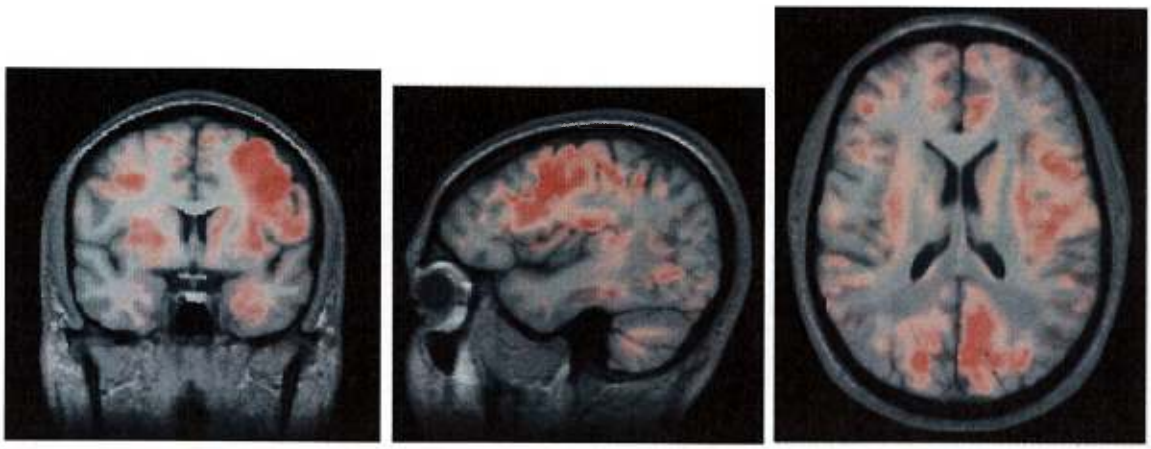

(a) Coronal section. (b) Sagittal section in left hemisphere. (c) Axial section.

Figure 4.12: Coronal, sagittal and axial sections of the probabilistic atlas. Shape variability is superimposed in red (see text for more details). Images are shown using the radiological convention, i.e. patient's left side is on the right side and vice-versa.

In the event that bad matches occur during registration, the model would reflect this by having larger variances in deformation and/or intensity. The image obtained and the corresponding statistics regarding deformations and intensities would not reflect normal variations, but to a certain extent reflect normal variations *within our registration framework.* It is our belief that the models obtained in this paper are intricately linked to our modeling of the registration problem. Though cross-validation of registration techniques results reports mutually coherent matches [94], average variations of 3 mm to 4 mm have been observed in this study. These figures are too large to give significance to our models' statistics using other registration methods.

Although beyond the scope of this article, we present in Figure 4.12 preliminary results

of a probabilistic atlas built using the information gathered during the construction of M_{11}. This figure presents slices of the average model on which information about shape variability is superimposed in red. This variability is computed as follows: we calculate the voxelwise covariance matrix of the residual deformation fields R_i obtained from the registration of each element of S_1 with M_{11}. The determinant, or the product of the eigenvalues, of each of these matrices is computed. The resulting values can be interpreted as probabilistic volumes (See [32] for more detailed geometric interpretations of this measure). Hence, for a given voxel, a large volume corresponds to a large variability of the positions of corresponding voxels found in S_1. This volume has been normalized and converted to a red intensity value added to the MR image.

We remind the reader that this probabilistic atlas was built using only five normal subjects, and hence does not reflect the extent of normal variability that is to be found in a larger population. Nonetheless, we wish to point out that high variability was found in the cortical region, which is known to present large shape variations. There also seems to be more variability in the left hemisphere than in the right one.

We are presently working on the evaluation of the number of subjects needed to fully represent the extent of variations in a normal population. Further interpretations of the corresponding probabilistic atlas will follow this work.

4.5 Conclusion

We have presented a completely automatic method to build average anatomical models of the human brain using a set of MR images. To this end, brain shape variations between subjects were identified. Differences due to linear transformations were excluded, resulting in the quantification of pure morphological differences. The result is an average intensity and shape image representative of the characteristics of the image set elements used for the construction. Furthermore, we have shown that this model corresponds to the centroid of the image set and does not depend on the reference image used for its construction. This stability is very important to ensure the efficiency and usefulness of our method. The coupling of such a high quality model with statistical information regarding normal deformations, such

as the one presented in Figure 4.12 or in the work of Thompson & Toga [97] or of the Brown/Washington groups [40, 70], could enrich the significance of statistical tests by adding intensity information, useful for example in detecting gliosis in T2 MR images, and would supply an important tool in the analysis of normal anatomy.

4.6 Acknowledgments

Dr. Neil Roberts from the Magnetic Resonance & Image Analysis Research Center (MARIARC) of Liverpool University provided the MR images used in this study. Part of this work was funded by the Natural Sciences and Engineering and Research Council of Canada (NSERC) and the Ministère de l'Éducation du Québec (MEQ).

Chapitre 5

Conclusion et perspectives

Sommaire

Dans les chapitres précédents, nous avons apporté des contributions importantes à trois grands domaines d'actualité en informatique médicale: le recalage, l'exploration de bases de données et la génération de modèles moyens. Ce chapitre rappelle les apports les plus importants que nous avons faits à chacun de ces domaines et situe chacun d'entre eux dans le but ultime de cette thèse: l'utilisation d'atlas probabilistes du cerveau en milieu clinique.

5.1 Recalage

Dans le chapitre 2, nous avons défini une méthode de recalage permettant de mettre en correspondance des images de patients différents acquises selon différentes modalités. Notre contribution à ce niveau ne réside pas tant dans l'obtention des déformations géométriques. Comme nous l'avons vu, notre méthode de transformation géométrique n'est qu'une petite modification de l'algorithme des démons suite à une analogie entre cette technique et la descente de gradient du SSD (Voir la section 2.2.1.). Notre apport réside dans la modélisation des différences d'intensité des structures du cerveau par rapport à leur méthodes d'acquisition

respectives et l'intégration de cette modélisation au sein de la méthode de recalage.

L'impact direct de nos travaux sur le recalage sur les travaux subséquents présentés dans cette thèse est la méthode de transformation d'intensité modélisée lors du recalage mono-modal. Comme mentionné précédemment, nous avons ici fait l'hypothèse d'une dépendance linéaire entre les intensités des images à recaler. Cette présomption linéaire s'explique en considérant les différents aspects affectant possiblement les différences d'intensité entre les structures de sujets différents :

1. L'intensité d'une structure dans l'image acquise dépend de la composition des différentes structures du cerveau et peut varier au sein de la population, mais cette variation est faible. Les variations importantes correspondent à des pathologies.
2. L'intensité dépend également des circonstances de l'acquisition. Les champs présents lors de l'acquisition dépendent du sujet scanné et évoluent au cours d'une journée. Encore ici, les variations au sein d'une population normale sont faibles.
3. Pour des fins de visualisation, les intensités des images sont souvent normalisées en milieu clinique à leur sortie du scanner par rapport à la plus forte intensité dans l'image. Dû au bruit ainsi qu'aux différents artéfacts possiblement présents dans l'image, le facteur multiplicatif n'est pas identique pour toutes les images.

Prenant en compte ces considérations, les différences d'intensité entre images provenant de différents sujets sont principalement dues à des pathologies et/ou à des normalisation d'intensité. Puisque nous avons ici seulement étudié des sujets normaux, la première cause peut être négligée. Pour la deuxième, il est généralement plus simple d'utiliser notre modèle de transformation d'intensité que d'élaborer un nouveau protocole d'acquisition et de prétraitement ne modifiant pas les intensités des images. Les normalisations mentionnées au point 3 étant des transformations linéaires, faire l'hypothèse d'une dépendance fonctionnelle de degré 1 est justifiée. Dans le cas d'étude de sujet anormaux, il serait préférable de faire appel à des transformations de degré plus élevé telles que présentées au chapitre 2.

L'aspect indirect de cette recherche se reflète principalement dans l'augmentation des possibilités d'utilisation des atlas générés dans le chapitre 4. Par exemple, la technique actuellement utilisée lorsque l'on veut placer un atlas de modalité A sur une image acquise

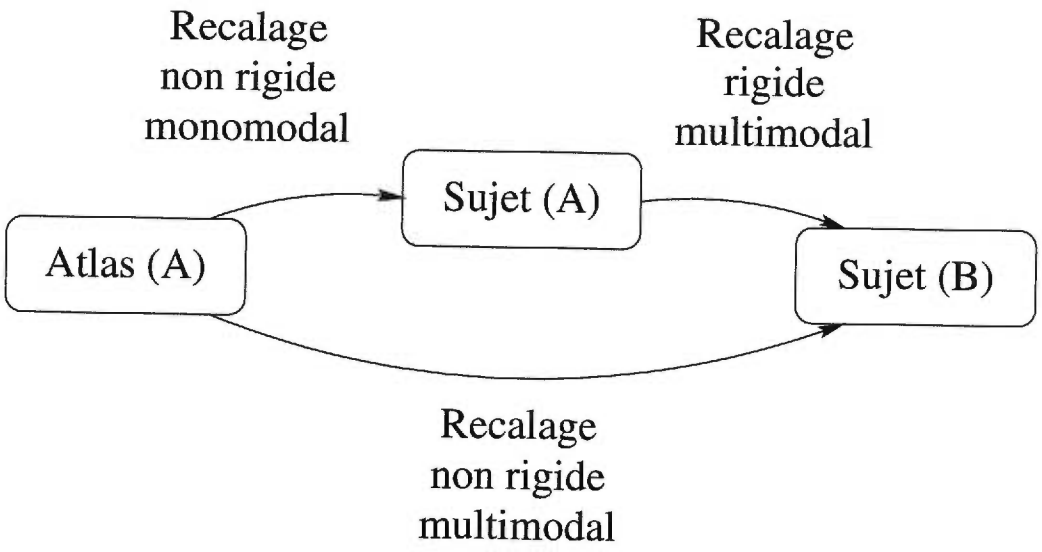

FIG. 5.1 – *La méthode actuellement utilisée (haut) pour recaler un atlas sur un sujet donné et la méthode que nous proposons (bas).*

selon une autre modalité B est de faire une acquisition du patient dans chaque modalité A et B (Voir la figure 5.1.). On effectue ensuite un recalage non rigide monomodal entre l'atlas et l'image de modalité A du sujet, puis un recalage rigide multimodal entre les deux images du sujet. Les déformations résultant de ce recalage sont ensuite appliquées à l'atlas pour le superposer sur l'image B du sujet. L'utilisation de notre méthode, permettant un recalage direct de l'image du sujet avec l'atlas, simplifie grandement ce procédé en plus d'avoir des considérations économiques importantes puisqu'il ne nécessite pas d'acquisition supplémentaire. Même si dans cette thèse nous n'avons pas apporté pas de preuve montrant la stricte équivalence des champs de déplacements indépendemment de la modalité d'acquisition, les statistiques présentées à la Table 2.2 nous permettent de croire que les déplacements sont très similaires. Cette méthode permet en plus le recalage d'images de sujets anormaux, présentant des variations anormales d'intensité lors des acquisitions, avec les atlas générés, ainsi que la construction d'atlas "pathologiques" à partir d'images de tels patients. Bien d'autres applications sont facilement envisageables.

5.2 Exploration de bases de données

Nos travaux sur l'exploration de bases de données visent l'application des techniques développées ici en milieu clinique. En effet, malgré les progrès toujours croissants de l'informatique, le recalage de deux images nécessite toujours trop de temps, parfois plusieurs jours pour certaines techniques, pour être applicable en milieu clinique. Nous avons ici montré qu'un clinicien s'intéressant à une structure particulière, par exemple l'hippocampe définie dans un atlas, pourrait s'attendre à obtenir la même structure ainsi que les zones de variations normales et anormales en moins d'une minute, un laps de temps plus qu'acceptable.

Plusieurs autres applications sont envisageables et nous en avons présenté quelques exemples. Dans le chapitre 3.4.1 nous montrons qu'il devient possible pour un clinicien de construire des atlas de certaines structures cérébrales "en ligne" afin d'obtenir rapidement des informations statistiques sur les variations anatomiques de la structure d'intérêt. Notons aussi que les exemples exposés dans le chapitre 3.4.2 doivent être placés dans un contexte de recherche de patients similaires dans de larges banques de données d'images tridimensionnelles. Nous croyons que de meilleurs résultats pourraient être obtenus en divisant les sujets étudiés en sous-classes selon leur morphologie. Ceci faciliterait l'analyse isolée de leurs différences morphométriques et permettrait une meilleure compréhension des dissimilarités entre un patient donné et le groupe de sujets normaux ayant la même morphologie. L'étude de ces catégories nous permettrait de rassembler des informations pertinentes sur chacune d'entre elles et d'en faire ressortir les caractéristiques principales.

5.3 Modèles moyens

Dans le chapitre 4, nous avons présenté une méthode de construction de modèle moyen anatomique du cerveau. Surtout, nous avons montré que ces modèles moyens sont stables par rapport à l'image cible et au nombre d'itérations effectuées pour construire le modèle. Ceci permet de modéliser les variations géométriques ainsi que les variations d'intensité. Comme mentionné précédemment, ces variations d'intensité sont peu importantes pour l'analyse de sujets normaux mais peuvent le devenir pour discriminer des pathologies où la forme des

structures reste inchangée.

Quoique les atlas générés dans cette thèse tiennent comptent de peu de sujets, des travaux sont présentement en cours afin d'étudier leurs propriétés sur de plus grands ensembles de données. Les résultats préliminaires sont prometteurs et corroborent ceux présentés ici. La construction d'un atlas construit à l'aide de plusieurs centaines d'images, et donc plus représentatif d'une population normale, sera l'oeuvre finale de ce projet.

Mis ensembles, les outils présentés ici permettent la construction d'atlas du cerveau selon plusieurs modalités ainsi que l'identification rapide de la présence de pathologies reflétées par des transformations géométriques et/ou d'intensité dans les images scannées. Ceci permet leur utilisation quotidienne dans un environnement clinique. Nous espérons que cette recherche fournira des informations pertinentes aux cliniciens, leur permettant ainsi de fournir des diagnostiques plus justes et plus complets.

Bibliographie

[1] Elseviers's Interactive ANATOMY. « Temporal Bone and Posterior Cranial Fossa ». CD-ROM, 1994. Full-Motion CD-I.

[2] N. C. ANDREASEN, S. ARNDT, V. SWAYZE II, T. CIZADLO, M. FLAUM, D. O'LEARY, J. C. EHRHARDT, et W. T. C. YUH. « Thalamic Abnormalies in Schizophrenia Visualized Through Magnetic Resonance Image Averaging ». *Science*, 266:294–298, 1994.

[3] R. BAJCSY et S. KOVAČIČ. « Multiresolution Elastic Matching ». *Computer Vision, Graphics and Image Processing*, 46(1):1–21, avril 1989.

[4] D. C. BARBER. « Registration of Low Resolution Medical Images ». *Physics in Medecine and Biology*, 37(7):1485–1498, 1992.

[5] J. L. BARRON, D. J. FLEET, et S. S. BEAUCHEMIN. « Performance of Optical Flow Techniques ». *International Journal of Computer Vision*, 12(1):43–77, janvier 1994.

[6] F. L. BOOKSTEIN. « Principal Warps: Thin-Plate Splines and the Decomposition of Deformations ». *IEEE Transactions on Pattern Analysis and Machine Intelligence*, 11(6):567–585, juin 1989.

[7] F. L. BOOKSTEIN. « Thin-Plate Splines and the Atlas Problem for Biomedical Images ». Dans A. C. F. COLCHESTER et C. J. HAWKES, éditeurs, *Proceedings of the Information Processing in Medical Imaging Conference*, volume 511 de *Lecture Notes in Computer Science*, pages 326–342, Wye, United Kingdom, juillet 1991.

[8] F. L. BOOKSTEIN. « *Functional Neuroimaging* », Chapitre 10 - Landmarks, Edges, Morphometrics, and the Brain Atlas Problem. Academic Press, 1994.

[9] F. L. BOOKSTEIN. « Shape and the Information in Medical Images: A Decade of the Morphometric Synthesis ». *Computer Vision and Image Understanding*, 66(2):97–118, may 1997.

[10] H. BRAAK. *Architectonics of the Human Telencephalic Cortex*. Springer-Verlag, Berlin, 1980.

[11] « Simulated Brain Database ». http://www.bic.mni.mcgill.ca/brainweb/.

[12] J. W. BRANDT. « Improved Accuracy in Gradient-Based Optical Flow Estimation ». *International Journal of Computer Vision*, 25(1):5–22, 1997.

[13] M. BRO-NIELSEN et C. GRAMKOW. « Fast Fluid Registration of Medical Images ». Dans K. H. HÖHNE et R. KIKINIS, éditeurs, *Proceedings of the 4th International Conference Visualisation in Biomedical Computing (VBC'96, held in Hamburg, Germany, September 22-25, 1996)*, volume 1131 de *Lecture Notes in Computer Science*, pages 267–276. Springer-Verlag, 1996.

[14] M. E. BRUMMER, R. M. MERSEREAU, R. L. EISNER, et R. R. J. LEWINE. « Automatic Detection of Brain Contours in MRI Data Sets ». *IEEE Transactions in Medical Imaging*, 12(2):153–166, juin 1993.

[15] P. CACHIER, X. PENNEC, et N. AYACHE. « Fast Non Rigid Matching by Gradient Descent: Study and Improvements of the "Demons" Algorithm ». Rapport Technique 3706, Institut National de Recherche en Informatique et en Automatique, juin 1999. http://www.inria.fr/RRRT/RR-3706.html.

[16] G. CHRISTENSEN, M. I. MILLER, et M. W. VANNIER. « A 3D Deformable Magnetic Resonance Textbook Based on Elasticity ». Dans *Spring Symposium: Applications of Computer Vision in Medical Image Processing*, Stanford (CA), USA, mars 1994. American Association for Artificial Intelligence.

[17] G. CHRISTENSEN, R. D. RABBITT, et M. I. MILLER. « 3D Brain Mapping Using a Deformable Neuroanatomy ». *Physics in Medecine and Biology*, 39:608–618, mars 1994.

[18] G. E. CHRISTENSEN. « *Deformable Shape Models for Anatomy* ». D. Sc. dissertation, Department of Electrical Engineering, Sever Institute of Technology, Washington

University, St. Louis, 1994.

[19] G. E. CHRISTENSEN, R. D. RABBITT, et M. I. MILLER. « Deformable Templates Using Large Deformation Kinematics ». *IEEE Transactions in Medical Imaging*, 5(10):1435–1447, octobre 1996.

[20] C. A. COCOSCO, V. KOLLOKIAN, R. K.-S. KWAN, et A. C. EVANS. « BrainWeb: Online Interface to a 3D MRI Simulated Brain Database ». *NeuroImage, Proceedings of the Third International Conference on Functional Mapping of the Human Brain (HBM'97, Conference held in Copenhagen, Danmark, May 19–23 1997)*, 5(4):S425, mai 1997.

[21] D. L. COLLINS, P. NEELIN, T. M. PETERS, et A. C. EVANS. « Automatic 3D Intersubject Registration of MR Volumetric Data in Standardized Talairach Space ». *Journal of Computer Assisted Tomography*, 18(2):1992–205, mars/avril 1994.

[22] D. L. COLLINS, T. M. PETERS, et A. C. EVANS. « An Automated 3D Non-Linear Image Deformation Procedure for Determination of Gross Morphometric Variability in Human Brain. ». Dans R. A. ROBB, éditeur, *Visualisation in Biomedical Computing*, volume 2359 de *SPIE Proceedings*, pages 180–190, Rochester, octobre 1994.

[23] D. L. COLLINS, A. P. ZIJDENBOS, V. KOLLOKIAN, J. G. SLED, N. J. KABANI, C. J. HOLMES, et A. C. EVANS. « Design and Construction of a Realistic Digital Brain Phantom ». *IEEE Transactions in Medical Imaging*, 17(3):463–468, juin 1998.

[24] B. M. DAWANT, J.-P. THIRION, F. MAES, D. VANDERMEULEN, et P. DEMAEREL. « Automatic 3D Segmentation of Internal Structures of the Head in MR Images Using a Combination of Similarity and Free Form Transformations ». Dans K. M. HANSON, éditeur, *Medical Imaging 1998: Image Processing (MI'98, Conference held in San Diego (CA), USA, Febuary 23–26 1998)*, volume 3338 de *SPIE Proceedings*, pages 545–554, San Diego (CA), USA, février 1998. Internation Society for Optical Engineering.

[25] J. DECLERCK, G. SUBSOL, J.-P. THIRION, et N. AYACHE. « Automatic Retrieval of Anatomical Structures in 3D Medical Images ». Dans N. AYACHE, éditeur, *Conference on Computer Vision, Virtual Reality and Robotics in Medecine*, volume 905 de *Lecture Notes in Computer Science*, pages 153–162, Nice (France), avril 1995. Springer-Verlag. http://www.inria.fr/RRRT/RR-2485.html.

[26] A. C. EVANS, M. KAMBER, D. L. COLLINS, et D. MACDONALD. An MRI-based probabilistic atlas of neuroanatomy. Dans S. SHORVON, D. FISH, F. ANDERMANN, G. M. BYDDER, et H. STEFAN, éditeurs, *Magnetic Resonance Scanning and Epilepsy*, volume 264 de *NATO ASI Series A, Life Sciences*, pages 263–274. Plenum Press, 1994.

[27] O. FAUGERAS. *Three-Dimensional Computer Vision: A Geometric Viewpoint.* MIT Press, Cambridge, Massachusetts, 1993.

[28] J. FELDMAR et N. AYACHE. « Rigid, Affine and Locally Affine Registration of Free-Form Surfaces ». *International Journal of Computer Vision*, 18(2):99–119, mai 1996.

[29] J. FELDMAR, J. DECLERCK, G. MALANDAIN, et N. AYACHE. « Extension of the ICP Algorithm to Non-Rigid Intensity-Based Registration of 3D Volumes ». *Computer Vision and Image Understanding*, 66(2):193–206, mai 1997.

[30] K. J. FRISTON, J. ASHBURNER, J. B. POLINE, C. D. FRITH, J. D. HEATHER, et R. S. J. FRACKOWIAK. « Spatial registration and normalisation of images ». *Proceedings of the Second International Conference on Functional Mapping of the Human Brain (HBM'95, Conference held in Paris, France, JUNE 27–30 1995)*, pages 165–189, 1995.

[31] K. FUKUNAGA. *Introduction to Statistical Pattern Recognition.* Computer science and scientific computing. Academic Press, 2 édition, 1990.

[32] K. FUKUNAGA. « *Introduction to Statistical Pattern Recognition* », Chapitre 2 – Random Vectors and Their Properties, pages 11–50. Computer science and scientific computing. Academic Press, London, England, 2nd édition, 1990.

[33] T. GAENS, F. MAES, D. VANDERMEULEN, et P. SUETENS. « Non-rigid Multimodal Image Registration Using Mutual Information ». Dans W. M. WELLS, A. COLCHESTER, et S. DELP, éditeurs, *Proceedings of the First International Conference on Medical Image Computing and Computer-Assisted Intervention (MICCAI'98, Conference held in Cambridge (MA), USA, October 11–13, 1998)*, volume 1496 de *Lecture Notes in Computer Science*, pages 1099–1106. Springer-Verlag, 1998.

[34] R. G. GALLAGER. *Information Theory and Reliable Communication.* Systems Science. John Wiley and sons, New-York, 1968.

[35] J. C. GEE, L. Le BRIQUER, C. BARILLOT, et D. R. HAYNOR. « Probabilistic Matching of Brain Images ». Dans Y. BIZAIS, C. BARILLOT, et R. Di PAOLA, éditeurs, *Proceedings of the Information Processing in Medical Imaging Conference*, pages 113–125, Dordrecht, 1995. Kluwer Academic Publishers.

[36] J. C. GEE, D. R. HAYNOR, L. Le BRIQUER, et R. K. BAJCSY. « Advances in Elastic Matching Theory and Its Implementation ». Dans P. CINQUIN, R. KIKINIS, et S. LAVALLEE, éditeurs, *Conference on Computer Vision, Virtual Reality and Robotics in Medecine & Medical Robotics and Computer Aided Surgery (CVRMed-MRCAS'97)*, Heidelberg, 1997. Springer-Verlag.

[37] J. C. GEE, M. REIVICH, et R. BAJCSY. « Elastically Deforming 3D Atlas to Match Anatomical Brain Images ». *Journal of Computer Assisted Tomography*, 17(2):225–236, 1993.

[38] R. C. GONZALEZ et R. E. WOODS. *Digital Image Processing.* Addison-Wesley, 1992.

[39] T. GREITZ, C. BOHM, S. HOLTE, et L. ERIKSSON. « A Computerized Brain Atlas: Construction, Anatomical Content, and Some Applications ». *Journal of Computer Assisted Tomography*, 15(1):26–38, janvier 1991.

[40] U. GRENANDER et M. I. MILLER. « Computational Anatomy: An Emerging Discipline ». *Quarterly of Applied Mathematics*, 56(4):617–694, décembre 1998.

[41] A. GUIMOND, J. MEUNIER, et J.-P. SOUCY. « Automated Detection of the Intercommissural Line in SPECT ». Dans *Engineering in Medicine and Biology Society*, Montréal, Canada, septembre 1995.

[42] A. GUIMOND, J. MEUNIER, et J.-P. THIRION. « Average Brain Models: A Convergence Study ». *Computer Vision and Image Understanding*, 1999. À paraître.

[43] A. GUIMOND, J. MEUNIER, et J.-P. THIRION. « Average Brain Models: A Convergence Study ». Rapport Technique 3731, Institut National de Recherche en Informatique et en Automatique, Sophia-Antipolis, France, juillet 1999. http://www.inria.fr/RRRT/RR-3731.html.

[44] A. GUIMOND, A. ROCHE, N. AYACHE, et J. MEUNIER. « Three-Dimensional Multimodal Brain Warping Using the Demons Algorithm and Adaptive Intensity Corrections ».

IEEE Transactions in Medical Imaging, 1999. Soumis.

[45] A. GUIMOND, G. SUBSOL, et J.-P. THIRION. « Automatic MRI Database Exploration and Applications ». *International Journal of Pattern Recognition and Artificial Intelligence*, 11(8):1345–1365, décembre 1997.

[46] C. R. G. GUTTMANN, R. KIKINIS, M. C. ANDERSON, M. JAKAB, S. K. WARFIELD, R. J. KILLIANY, H. L. WEINER, et F. A. JOLESZ. « Quantitative Follow-up of patients With Multiple Sclerosis Using MRI: Reproducibility ». *Magnetic Resonance Imaging*, 9:509–518, 1999.

[47] A. GUÉZIEC et N. AYACHE. « Smoothing and Matching of 3D Space Curves ». Dans *Europeen Conference on Computer Vision*, Santa Margherita (Italy), mai 1992. Springer-Verlag.

[48] J. W. HALLER, A. BANERJEE, G. E. CHRISTENSEN, M. GADO, S. C. JOSHI, , M. I. MILLER, Y. SHERLINE, M. W. VANNIER, et J. G. CSERNANSKY. « Three-dimensional Hippocampal MR Morphometry with High-dimensional Transformation of a Neuroanatomic Atlas ». *Radiology*, 202:504–510, 1997.

[49] P. HELLIER, C. BARILLOT, E. MÉMIN, et P. PÉREZ. « Medical Image Registration with Robust Multigrid Techniques ». Dans *Proceedings of the Second International Conference on Medical Image Computing and Computer-Assisted Intervention (MICCAI'99, Conference held in Cambridge, England, September 19–22, 1999)*, volume 1679 de *Lecture Notes in Computer Science*, pages 680–687, Cambridge, England, octobre 1999.

[50] K. H. HÖHNE, M. BOMANS, M. RIEMER, R. SCHUBERT, U. TIEDE, et W. LIERSE. « A 3D anatomical atlas based on a volume model ». *IEEE Computer Graphics and Applications*, 12(4):72–78, juillet 1992.

[51] H. HOKAMA, M. E. SHENTON, P. G. NESTOR, R. KIKINIS, J. J. LEVITT, D. METCALF, C. G. WIBLE, B. F. O'DONNELL, F. A. JOLESZ, et R. W. MCCARLEY. « Caudate, Putamen, and Globus Pallidus Volume in Schizophrenia: A Quantitative MRI Study ». *Psychiatry Research: Neuroimaging*, 61:209–229, 1995.

[52] B. K. P. HORN et B. G. SCHUNCK. « Determining Optical Flow ». *Artificial Intelligence*, 17:185–203, août 1981.

[53] C. R. JACK. « Hippocampal T2 relaxometry in epilepsy : past, present and future ». *ajn*, 17:1811–1814, 1996.

[54] S. JOSHI. « *Large deformation diffeomorphisms and Gaussian random fields for statistical characterization of brain subminifolds* ». PhD thesis, Department of Electrical Engineering, Sever Institute of Technology, Washington University, St. Louis, 1997.

[55] D. G. KENDALL. « A Survey of the Statistical Theory of Shape ». *Statistical Science*, 4(2):87–120, 1989.

[56] R. KIKINIS, M. E. SHENTON, D. V. IOSIFESCU, R. W. MCCARLEY, P. SAIVIROONPORN, H. H. HOKAMA, A. ROBATINO, D. METCAL, C. G. WIBLE, C. M. PORTAS, R. M. DONNINO, et F. A. JOLESZ. « A Digital Brain Atlas for Surgical Planning, Model-Driven Segmentation, and Teaching ». *IEEE Transactions on Visualization and Computer Graphics*, 2(3):232–241, septembre 1996.

[57] S. KOVAČIČ et R. BAJCSY. « *Brain Warping* », Chapitre 3. Multiscale/Multiresolution Representations, pages 45–65. Academic Press, 1999.

[58] R. K.-S. KWAN, A. C. EVANS, et G. B. PIKE. « An Extensible MRI Simulator for Post-Processing Evaluation ». Dans K. H. HÖHNE et R. KIKINIS, éditeurs, *Proceedings of the 4th International Conference Visualisation in Biomedical Computing (VBC'96, held in Hamburg, Germany, September 22-25, 1996)*, volume 1131 de *Lecture Notes in Computer Science*, pages 135–140. Springer-Verlag, 1996.

[59] Y. H. LAU, M. BRAUN, et B. F. HUTTON. « Non-rigid 3d image registration using regionally constrainted matching and the correlation ratio ». Dans *International Workshop on Biomedical Image Registration (WBIR'99, Workshop help in Bled, Slovenia, August 30–31, 1999)*, 1999. À paraître.

[60] L. LE BRIQUER et J. C. GEE. « Design of a Statistical Model of Brain Shape ». Dans J. S. DUNCAN et G. R. GINDI, éditeurs, *Proceedings of the Information Processing in Medical Imaging Conference (IPMI'97)*, Vermont, USA, 1997. Springer-Verlag.

[61] D. LEMOINE, C. BARILLOT, B. GIBAUD, et E. PASQUALINI. « An Anatomical-Based 3D Registration System of Multimodality and Atlas Data in Neurosurgery ». *Lecture Notes in Computer Science*, 511:154–164, 1991.

[62] F. MAES, A. COLLIGNON, D. VANDERMEULEN, G. MARCHAL, et P. SUETENS. « Multimodality Image Registration by Maximization of Mutual Information ». *IEEE Transactions in Medical Imaging*, 16(2):187–198, 1997.

[63] J. B. MAINTZ. « *Retrospective Registration of Tomographic Brain Images* ». PhD thesis, Utrecht University, Netherlands, 1996.

[64] J. B. A. MAINTZ, E. H. W. MEIJERING, et M. A. VIERGEVER. « General Multimodal Elastic Registration Based on Mutual Information ». Dans K. M. HANSON, éditeur, *Medical Imaging 1998: Image Processing (MI'98, Conference held in San Diego (CA), USA, Febuary 23–26 1998)*, volume 3338 de *SPIE Proceedings*, pages 144–154, Bellingham (WA), USA, avril 1998. Internation Society for Optical Engineering.

[65] J. B. A. MAINTZ et M. A. VIERGEVER. « A survey of medical image registration ». *Medical Image Analysis*, 2(1):1–36, avril 1998.

[66] J. MARTIN, A. PENTLAND, S. SCLAROFF, et R. KIKINIS. « Characterization of Neuropathological Shape Deformations ». Rapport Technique 331, M.I.T. Media Laboratory Perceptual Computing, mai 1995.

[67] T. MATSUI et A. HIRANO. *An Atlas of the Human Brain for Computerized Tomography.* Igaku-Shoin, 1978.

[68] J. C. MAZZIOTTA, A. W. TOGA, A. EVANS, P. FOX, et J. LANCASTER. « A Probabilistic Atlas of the Human Brain: Theory and Rationale for Its Development ». *Neuroimage*, 2:89–101, 1995.

[69] D. P. MCGARRY, T. R. JACKSON, M. B. PLANTEC, N. F. KASSELL, et J. H. DOWNS. « Registration of Functional Magnetic Resonance Imagery using Mutual Information and Surface Matching ». Dans *Medical Imaging: Image Processing*, Newport Beach, United-States, février 1997.

[70] M. I. MILLER, A. BANERJEE, G. E. CHRISTENSEN, S. C. JOSHI, N KHANEJA, U. GRENANDER, et L. MATEJIC. « Statistical Methods in Computational Anatomy ». *Statis-*

tical Methods in Medical Research, 6:267–299, 1997.

[71] S. MINOSHIMA, K. L. BERGER, K. S. LEE, et M. A. MINTUN. « An Automated Method for Rotational Correction and Centering of Three-Dimensional Functional Brain Images ». *Journal of Nuclear Medicine*, 33(8):1579–1585, 1992.

[72] A. PAPOULIS. *Probability, Random Variables, and Stochastic Processes.* McGraw-Hill, Inc, 3 édition, 1991.

[73] T. PAVLIDIS. *Structural Pattern Recognition*, volume 1 de *Springer series in electrophysics.* Springer-Verlag, New-York, 1977.

[74] X. PENNEC, P. CACHIER, et N. AYACHE. « Understanding the "Demon's Algorithm": 3D Non-Rigid registration by Gradient Descent ». Dans?, éditeur, *Proceedings of the Second International Conference on Medical Image Computing and Computer-Assisted Intervention (MICCAI'99, Conference held in Cambridge, England, September 19–22, 1999)*, volume? de *Lecture Notes in Computer Science*, page? Springer-Verlag, 1999.

[75] E. PERNKOPF. *Atlas d'anatomie humaine.* Piccin, 1983.

[76] A. ROCHE, G. MALANDAIN, et N. AYACHE. « Unifying Maximum Likelihood Approaches in Medical Image Registration ». *International Journal of Imaging Systems and Technology*, 1999. Soumis. http://www.inria.fr/RRRT/RR-3741.html.

[77] A. ROCHE, G. MALANDAIN, N. AYACHE, et S. PRIMA. « Towards a Better Comprehension of Similarity Measures used in Medical Image Registration ». Dans *Proceedings of the Second International Conference on Medical Image Computing and Computer-Assisted Intervention (MICCAI'99, Conference held in Cambridge, England, September 19–22, 1999)*, volume 1679, pages 555–566. Springer-Verlag, octobre 1999.

[78] A. ROCHE, G. MALANDAIN, X. PENNEC, et N. AYACHE. « The Correlation Ratio as a New Similarity Measure for Multimodal Image Registration ». Dans W. M. WELLS, A. COLCHESTER, et S. DELP, éditeurs, *Proceedings of the First International Conference on Medical Image Computing and Computer-Assisted Intervention (MICCAI'98, Conference held in Cambridge (MA), USA, October 11–13, 1998)*, volume 1496 de *Lecture Notes in Computer Science*, pages 1115–1124. Springer-Verlag, 1998. http://www.inria.fr/RRRT/RR-3378.html.

[79] P. J. ROUSSEEUW et K. Van DRIESSEN. « Computing LTS Regression for Large Data Sets ». Rapport Technique, Statistics Group, University of Antwerp, 1999. http://win-www.uia.ac.be/u/statis/publicat/fastlts_readme.html.

[80] P. J. ROUSSEEUW et A. M. LEROY. *Robust Regression and Outlier Detection.* Wiley series in probability and mathematical statistics. John Wiley & Sons, 1987.

[81] G. SCHALTENBRAND et W. WAHREN. *Atlas of Stereotaxy of the Human Brain.* Georg Thieme Verlag, Stuttgart, 1977.

[82] E. P. SIMONCELLI. « Design of Multi-Dimensional Derivative Filters ». Dans *International Conference on Image Processing*, Austin, USA, novembre 1994. IEEE.

[83] G. SUBSOL. « *Construction automatique d'atlas anatomiques morphométriques à partir d'images médicales tridimensionnelles* ». PhD thesis, École Centrale de Paris, 1995. http://www.inria.fr/RRRT/TU-0379.html.

[84] G. SUBSOL, J.-P. THIRION, et N. AYACHE. « A General Scheme for Automatically Building 3D Morphometric Anatomical Atlases: applications to a Skull Atlas ». Dans *Medical Robotics and Computer Aided Surgery*, pages 373–382, Baltimore, novembre 1995. http://www.inria.fr/RRRT/RR-2586.html.

[85] G. SUBSOL, J.-P. THIRION, et N. AYACHE. « Application of an Automatically Built 3D Morphometric Brain Atlas: Study of Cerebral Ventricle Shape ». *Lecture Notes in Computer Science*, 1131:373–382, 1996.

[86] G. SUBSOL, J.-P. THIRION, et N. AYACHE. « A Scheme for Automatically Building Three-Dimensional Morphometric Anatomical Atlases: Application to a Skull Atlas ». *Medical Image Analysis*, 2(1):37–60, 1998.

[87] R. SZELISKI et S. LAVALLÉE. « Matching 3-D Anatomical Surfaces with Non-Rigid Deformations using Octree-Splines ». *International Journal of Computer Vision*, 18(2):171–186, mai 1996.

[88] J. TALAIRACH et P. TOURNOUX. *Co-Planar Stereotaxic Atlas of the Human Brain.* Thieme Medical Publishers, New York, 1988.

[89] J.-P. THIRION. « Fast Non-Rigid Matching of 3D Medical Images ». Dans *Medical Robotics and Computer Aided Surgery*, pages 47–54, Baltimore, novembre 1995.

http://www.inria.fr/RRRT/RR-2547.html.

[90] J.-P. THIRION. « Fast Non-Rigid Matching of 3D Medical Images ». Rapport Technique 2547, Institut National de Recherche en Informatique et en Automatique, Sophia-Antipolis, 1995. http://www.inria.fr/RRRT/RR-2547.html.

[91] J.-P. THIRION. « Non-Rigid Matching Using Demons ». Dans *Proceedings of the Computer Vision and Pattern Recognition Conference*, pages 245–251, San Francisco, USA, juin 1996. http://www.inria.fr/RRRT/RR-2547.html.

[92] J.-P. THIRION. « *Mise en Correspondance Automatique d'Images Médicales Tri-Dimensionnelles* ». Thèse d'habilitation à diriger des recherches, Université de Nice, Sophia-Antipolis, France, juin 1997.

[93] J.-P. THIRION. « Image matching as a diffusion process: an analogy with Maxwell's demons ». *Medical Image Analysis*, 2(3):243–260, 1998.

[94] J.-P. THIRION, G. SUBSOL, et D. DEAN. « Cross Validation of Three Inter-Parients Matching Methods ». Dans K. H. HÖHNE et R. KIKINIS, éditeurs, *Visualisation in Biomedical Computing (VBC'96)*, volume 1131 de *Lecture Notes in Computer Science*, pages 327–336, Hamburg, Germany, septembre 1996. Springer-Verlag.

[95] P. THOMPSON et A. W. TOGA. « A Surface-Based Technique for Warping 3-Dimensional Images of the Brain ». *IEEE Transactions in Medical Imaging*, 15:1–16, 1996.

[96] P. M. THOMPSON, D MACDONALD, M. S. MEGA, C. J. HOLMES, A. C. EVANS, et A. W. TOGA. « Detection and Mapping of Abnormal Brain Structure with a Probabilistic Atlas of Cortical Surfaces ». *Journal of Computer Assisted Tomography*, 21(4):567–581, 1998.

[97] P. M. THOMPSON et A. W. TOGA. « Detection, Visualization and Animation of Abnormal Anatomic Structure with a Deformable Probabilistic Brain Atlas Based on Random Vector Field Transformations ». *Medical Image Analysis*, 1(4):271–294, septembre 1997.

[98] A. W. TOGA. *Brain Warping.* Academic Press, 1999.

[99] A. W. TOGA, P. M. THOMPSON, et B. A. PAYNE. « *Developmental Neuroimaging: Mapping the Development of Brain and Behavior* », Chapitre Modeling Morphometric Changes of the Brain during Development, pages 15–27. Academic Press, San Diego (CA), USA, 1996.

[100] A. VENOT, J. F. LEBRUCHEC, J. L. GOLMARD, et J. C. ROUCAVROL. « An Automated Method for the Normalization of Scintigraphic Images ». *Journal of Nuclear Medicine*, 24:529–531, 1983.

[101] A. VENOT et V. LECLERC. « Automated Correction of Patient Motien and Gray Values Prior to Subtraction in Digitized Angiography ». *IEEE Transactions in Medical Imaging*, MI-3(4):179–184, décembre 1984.

[102] P. VIOLA et W. M. WELLS. « Alignment by Maximization of Mutual Information ». *International Journal of Computer Vision*, 24(2):137–154, 1997.

[103] J. WEBB, A. GUIMOND, N. ROBERTS, P. ELDRIDGE, D. CHADWICK, J. MEUNIER, et J.-P. THIRION. « Automatic detection of hippocampal atrophy on magnetic resonance images ». *Magnetic Resonance Imaging*, 17(8):1149–1161, avril 1999.

[104] J. WEST, J. M. FITZPATRICK, M. Y. WANG, B. M. DAWANT, C. R. MAURER, JR., R. M. KESSLER, R. J. MACIUNAS, C. BARILLOT, D. LEMOINE, A. COLLIGNON, F. MAES, P. SUETENS, D. VANDERMEULEN, P. A. van den ELSEN, P. F. HEMLER, S. NAPEL, T. S. SUMANAWEERA, B. HARKNESS, D. L. G. HILL, C. STUDHOLME, G. MALANDAIN, X. PENNEC, M. E. NOZ, G. Q. MAGUIRE, Jr, M. POLLACK, C. A. PELIZZARI, R. A. ROBB, D. HANSON, et R. P. WOODS. « Comparison and Evaluation of Retrospective Intermodality Image Registration Techniques ». *Journal of Computer Assisted Tomography*, 21:554–566, 1997.

[105] R. P. WOODS, S. T. GRAFTON, J. D. G. WATSON, N. L. SICOTTE, et J. C. MAZZIOTTA. « Automated Image Registration: II. Intersubject Validation of Linear and Nonlinear Models ». *Journal of Computer Assisted Tomography*, 22(1):153–165, 1998.

[106] R. P. WOODS, J. C. MAZZIOTTA, et S. R. CHERRY. « MRI-PET Registration with Automated Algorithm ». *Journal of Computer Assisted Tomography*, 17(4):536–546, 1993.